Developments in Double-Modulated Terahertz Differential Time-Domain Spectroscopy

by

Jegathisvaran Balakrishnan

B.Eng. (Electrical & Electronic, Honours),
The University of Adelaide, 2005

Thesis submitted for the degree of

Doctor of Philosophy

in

School of Electrical & Electronic Engineering,
The Faculty of Engineering, Computer, and Mathematical Sciences
The University of Adelaide, Australia

February, 2010

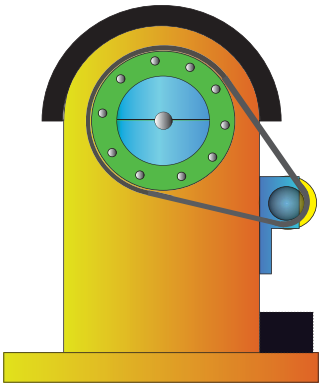

Introduction and Motivation

THIS chapter introduces the field of THz radiation (T-rays) and discusses the motivation for the work in this Thesis. It provides a roadmap for the Thesis and a concise summary of the novel contributions represented by this work. The structure of the Thesis and the contents of the chapters are outlined, and the the original contributions are highlighted.

1.1 Introduction

The T-ray (THz) region of the electromagnetic spectrum has proven to be one of the most elusive. T-ray radiation is loosely defined by the 0.1 to 10 THz frequency range (Abbott and Zhang 2007). According to the definition, T-rays are situated between the microwave and infrared regions of the electromagnetic spectrum (Fig. 1.1). The T-ray region remains as one of the least explored parts of the electromagnetic spectrum. Until the early 1980s T-rays were limited due to inefficient generation and detection techniques and also due to high atmospheric absorption. The introduction of the first ultrafast laser by Theodore Maiman in 1960s (Maiman 2000) underpinned the extensive pioneering work on generation and detection of T-ray in the early 1980s. The THz

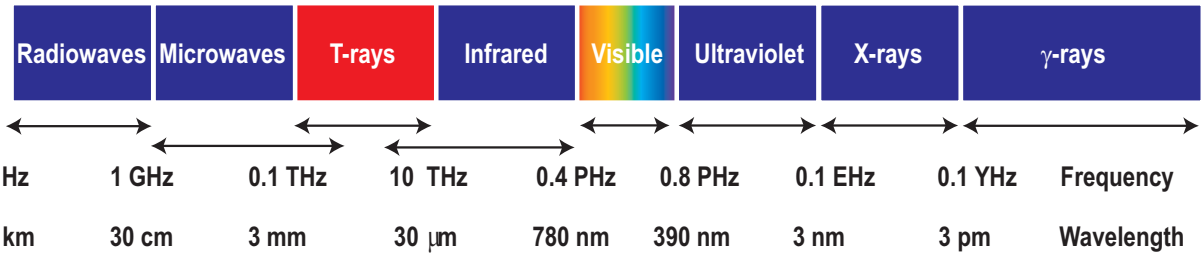

Figure 1.1. The electromagnetic spectrum. This figure illustrates a representation of the electromagnetic spectrum with the T-ray band partly overlapping the microwave and infrared regions. For simplicity, the millimetre wave band is taken to be a subset of the microwave band for this illustration.

time-domain spectroscopy was introduced for the first time in late 1980s by van Exter *et al.* (1989). Since then, the interest in THz technology has grown tremendously. In general, there are two methods of T-ray generation and detection based on ultrafast laser pulses: first, transient photoconductivity in semiconductor material (i.e., GaAs, SOS), second, nonlinear effects through optical rectification in electro-optic crystals.

T-rays are of great importance to biological sciences, because complementary information to traditional spectroscopic measurements on low-frequency bond vibrations, hydrogen bond stretching, and torsions in liquids and gases may be obtained (Yin 2008). T-rays are also well known as a *fingerprint region* that enables detection of chemicals or biomolecules through their unique THz vibrational spectral features (Fischer 2005). T-rays are considered to be non-invasive due to low photon energies (0.41 meV at 0.1 THz). This is particularly attractive for biomedical applications. The full potential of THz was not realised till the introduction of T-ray imaging by Hu and Nuss

(1995), which opened up wide opportunity for applications ranging from defence, security and biosensing.

It has been demonstrated that dry, non-polar, and nonmetallic substance such as paper, cardboard, and plastics are transparent to T-rays (Kemp *et al.* 2003). This useful feature led to a term called T-ray *retection*, which simply means "detection of an object through a concealed layer" (Abbott and Zhang 2007). Several studies have been conducted on packaging materials leading to potential application in quality control and security. Shining T-rays on packaging materials may reveal a molecular fingerprint to identify the contents (Abbott and Zhang 2007).

The double-modulated terahertz differential time-domain spectroscopy (double modulated THz-DTDS) scheme has drawn considerable attention among the researchers in the recent years (Mickan *et al.* 2002b, Mickan *et al.* 2004). This scheme is based on linear dithering of the sample under test and was first used to characterise thin samples in the GHz-THz range. Linear dithering, however, imposes a fundamental limitation as it introduces mechanical noise into the system. In this Thesis, the double-modulated THz-DTDS scheme is employed on a novel approach based on mounting the sample on a spinning wheel in order to overcome the fundamental limitation imposed by the linear dithering.

This Thesis presents a systematic approach of original research in (i) sensing hygroscopicity, (ii) developing a parameter extraction technique using a novel spinning wheel device, (iii) performing fixed dual-thickness liquid sensing, and (iv) a literature review as a foundation for the experimental chapters.

1.2 Thesis overview

In Ch. 2, the seemingly diverse collection of electromagnetic waves that can be classified in terms of a continuous range of wavelength, frequency, or energy are described. The electromagnetic spectrum can be categorised into various regimes, namely radiowaves, microwaves, T-rays, infrared, visible light, ultraviolet, X-rays, and γ-rays. A brief historical development of each electromagnetic region is presented.

Chapter 3 gives an overview of a basic experimental techniques in THz time-domain

spectroscopy. A method of generation and detection of terahertz radiation based on photoconductive antennas is discussed. A data analysis technique used for spectroscopic applications is elaborated.

Polymers are used as sample holder windows for THz experiments. Chapter 4 reviews the properties of thermoplastic polymers and its molecular interaction with THz radiation. The motivation of this chapter is to characterise a range of thermoplastic polymers with a view to identifying improved THz window materials. In Chapter 5, hygroscopicity of polymer and copolymer materials using a linear absorption model have been investigated.

Chapter 6 reviews various window cell geometries for liquid spectroscopy. Novel custom-built sample holders have been presented in this chapter. Data analysis techniques for each geometry are discussed.

Novel contribution to THz material parameter extraction using a spinning wheel mechanism is presented in Ch. 7. The spinning wheel mechanism is implemented using a double-modulated THz-DTDS sensing method. Chapter 8 shows how the spinning wheel technique can be applied to liquid by introducing a novel fixed dual-thickness window cell.

The Thesis conclusion is described in Ch. 9. Here, a review on each chapter is performed and the future work is elaborated.

Appendix A describes a modelling technique of terahertz signal extraction using lock-in amplifier. The first part of the chapter gives a detailed explanation on modelling terahertz signal extraction from a conventional THz-TDS spectrometer and the second part of the chapter discusses the modelling terahertz signal extraction from a double-modulated THz-DTDS spectrometer.

Appendix B focuses on substance retection within a faux suitcase. A commercially available Picometrix^{TM} T-Ray 2000 system is used to obtain spectral data.

Appendix C lists most of the experimental equipment used in this Thesis. Moreover,

data aquisition technique for both conventional THz-TDS and double-modulated THz-DTDS are described. Appendix D elaborates the software program developed as part of this research.

The structural interconnnections of the main chapters are shown in Fig. 1.2. This flow chart shows which chapter contains original experimental work, and how they are linked. The Thesis progresses along this chart from top to bottom and left to right.

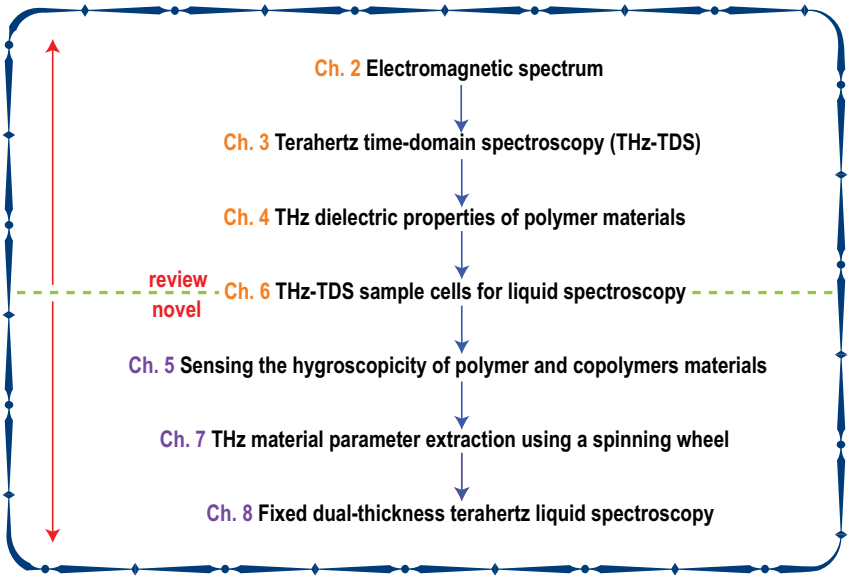

Figure 1.2. Thesis structural flow chart. This flow chart shows how the chapters in this Thesis fit together. There are two parts to this Thesis: first part is the review section. Here, the chapters are dedicated purely to a literature review. The second part focuses on the original contributions of this Thesis work. Chapter 6 contains a review of sample cells, along with original work on our custom built liquid cells.

1.3 Original contribution

The original contributions in this Thesis made to T-ray science lie both in system design and T-ray applications. The originality and breadth of these contributions is evidenced by the list of publications on page xvii.

The work in this Thesis was the first to demonstrate the measurement of polar and non-polar polymer materials (i.e., PMMA, PC, COC 6013S04, COC 5013L10, HDPE, and PTFE) using a linear absorption model in the low terahertz frequency band (Ch. 5).

Following the initial demonstration of double-modulated THz-DTDS by Mickan (2003), this Thesis shows an improved double-modulated THz-DTDS for material characterisation. In this Thesis, the double-modulated THz-DTDS is demonstrated using a novel spinning wheel device. The measurement technique is verified experimentally and shown to improve the signal-to-noise ratio (Ch. 7).

With the success of the spinning wheel device through the double-modulated THz-DTDS technique, the device is then used for liquid spectroscopy applications for the first time (Ch. 8). Here, we introduce a fixed dual-thickness measurement technique for the first time and demonstrate a reduction in the window cell thickness error to less than 5 μm. For verification purposes, several liquids from the literature (i.e., water, methanol, and ethanol) have been tested and compared to measurements in the literature.

The original contributions of this Thesis offers benefits to THz liquid spectroscopy, and the technology of T-ray spectrometers. The technique is not limited to liquids and by simple extension may find use for characterising solids and thin films.

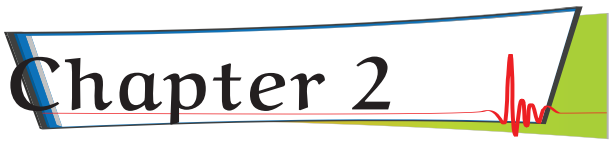

Electromagnetic spectrum

THE electromagnetic spectrum refers to all electromagnetic waves that are described in terms of wavelength, frequency, or energy. The spectrum includes radiowaves, microwaves, T-rays, infrared, visible light, ultraviolet, X-rays, and γ-rays in increasing order of frequency. In this chapter, a brief fundamental historical development of the electromagnetic spectrum is described.

2.1 Introduction

The electromagnetic spectrum refers to the seemingly diverse collection of electromagnetic waves that can be classified in terms of a continuous range of wavelength, frequency, or energy. According to Maxwell's classical theories, an electromagnetic wave oscillates sinusoidally and constitutes electric and magnetic fields that are mutually perpendicular to each other and to the direction of propagation (Brittain *et al.* 1970). The electromagnetic wave is shown schematically in Fig. 2.1.

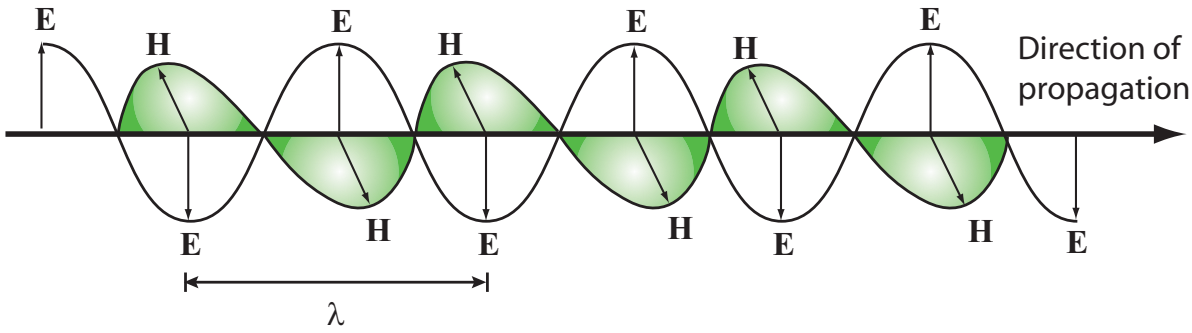

Figure 2.1. The electromagnetic wave. This figure illustrates an electromagnetic wave that consists of an electric field coupled with a magnetic field. The magnetic and electric fields of an electromagnetic wave are perpendicular to each other and to the direction of propagation of the wave.

As illustrated in Fig. 2.1, the electric and magnetic fields can be represented by vectors **E** and **H** respectively. Wavelength λ, is the distance between two successive peaks in a wave. The unit of wavelength is in metres, m. Frequency f, is defined as the number of wavelengths passing through a fixed point in time. Here, the unit for frequency is Hertz (Hz). Thus, both wavelength and frequency are related to the speed of light by the following equation:

$$\lambda = \frac{c}{f}, \tag{2.1}$$

where c is 3×10^{8} ms^{-1}. Also, the photon energy, E, given by the Planck equation, is related to wavelength and frequency by the following:

$$E = hf = \frac{hc}{\lambda}. \tag{2.2}$$

Here, h is known as Planck's constant, 6.6×10^{-34} Js^{-1}.

The electromagnetic spectrum can be categorised into various regimes, namely radiowaves, microwaves, T-rays, infrared, visible light, ultraviolet, X-rays and γ-rays (Fig. 1.1).

2.1.1 Objectives and framework

A brief historical development of the electromagnetic spectrum is discussed in this chapter. In Sec. 2.2, we present the seemingly diverse collection of electromagnetic waves ranging from radiowaves through to γ-rays. A brief introduction on the discoverer of each electromagnetic region is described in this section.

2.2 In the Beginning

2.2.1 Radiowaves

Heinrich Rudolf Hertz, a German physicist, born in Hamburg (Fig. 2.2), discovered radiowaves in 1887 using an oscillatory discharge across a spark gap, confirming the electromagnetic theory of light presented by James Clerk Maxwell in 1864. Hertz demonstrated the existance of electromagnetic waves by implementing the experimental setup illustrated in Fig. 2.3. According to Hertz's theory, electricity is a form of electromagnetism. As result of his theory, wireless telegraph and radio have been developed. According to Band (2006), radiowaves are defined as the region of the electromagnetic spectrum from a few Hz up to 1 GHz or photon energies of up to 4.11 μeV, which corresponds to a wavelength of up to 0.3 m. This part of the spectrum is commonly used in the communications field, ranging from radio to radar. Futhermore, radiowaves are widely used in spectroscopic applications such as nuclear magnetic resonance (NMR) and electron spin resonance (ESR).

2.2.2 Microwaves

Radiation arising from electrical disturbances at high frequencies is known as the microwave (Fuller 1979). Microwaves embrace a frequency range from 1 GHz to about 1 THz (or photon energy ranging from 4.11 μeV to 4.1 meV) with corresponding wavelengths ranging from 30 cm to 300 μm (Band 2006). Cellular communications falls in

Figure 2.2. Heinrich Rudolf Hertz (1857 - 1894). The discoverer of radiowaves. Adapted from Baird *et al.* (1998).

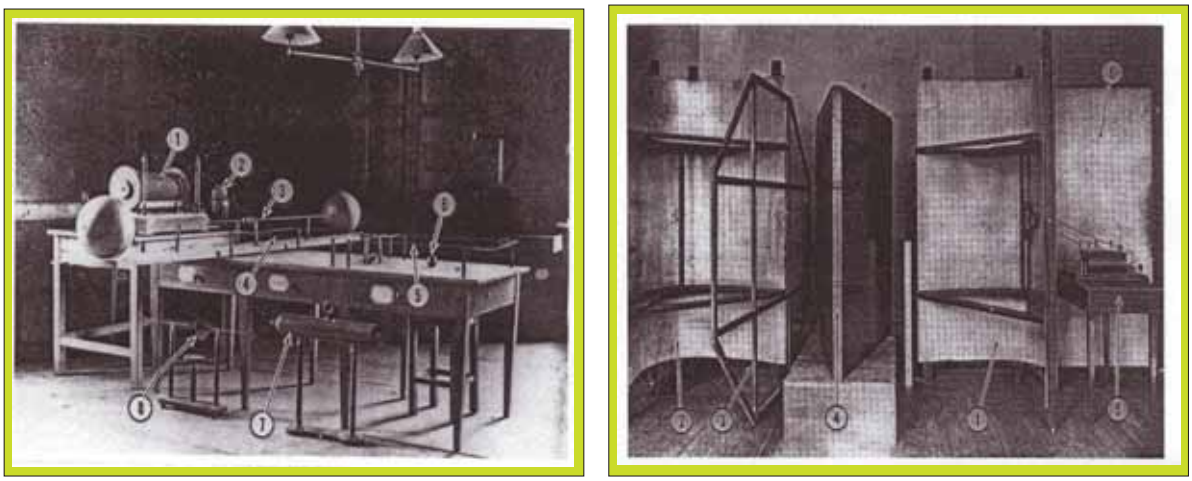

(a) (b)

Figure 2.3. Hertz's laboratory appratus. Fig. 2.3a illustrates a transmitter and a receiver setup to generate an electromagnetic wave with a 6 m wavelength. Fig. 2.3b shows a 60 cm wavelength apparatus. This setup was built to demonstrate optics-like properties of radio waves. Further details on Hertz's apparatus can be obtained from Byrant (1998).

this regime. Microwave radiation is generated using a high-power electron gun (i.e., klystron or magnetron) and resonant cavities as shown in Fig. 2.4. Figure 2.4a shows a typical single cavity klystron or reflex klystron that is capable of producing high power radiation (i.e., in the MW range). As shown in Fig. 2.4a, an electron gun directs electrons through the grids of the resonator cavity towards the reflector. Feedback is required to maintain the oscillation of the electrons within the cavity. This can be

achieved by reversing the electrons back to the cavity using a reflector. Thus, as the beam reflects through the grids the second time, the beam emerging from the grid is collected from the body of the resonator (Dunlop and Smith 1994). The reflex klystron is widely used for spectroscopy. Another high powered source of microwave radiation

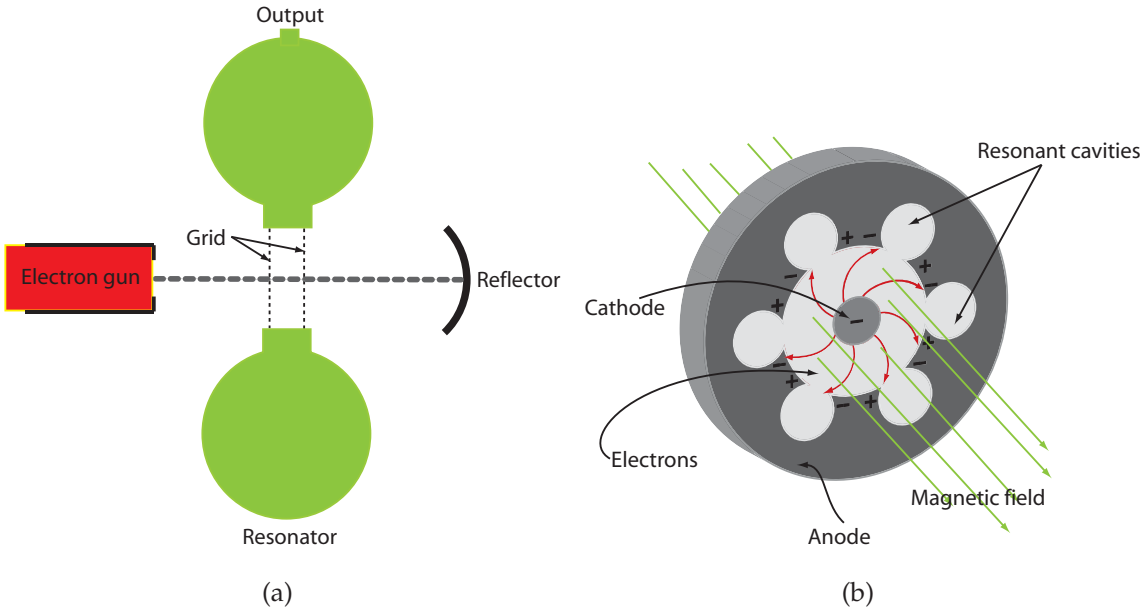

Figure 2.4. Microwave radiation sources: Reflex klystron and magnetron. This figure depicts the schematic diagram of (a) a reflex klystron and (b) a magnetron. Details of these radiation sources are given in the text.

is known as the magnetron (Fig. 2.4b). In Fig. 2.4b, a heated cathode thermionically produces electrons. The electrons are then moved to the anode directly in the presence of an electric field. As a magnetic field exerts a magnetic force on these electrons, circular motion of travel to reach the anode is achieved (Dunlop and Smith 1994). Thus, the microwave radiation is generated from the orbiting electrons in the cavities. The magnetron is widely used as a source in applications such as microwave ovens and radar.

2.2.3 T-rays

The Terahertz (THz) or T-ray region of the electromagnetic spectrum has proven to be one the most elusive, ovelapping the microwave and infrared regions. T-rays are loosely defined between 0.1 THz to 10 THz, which corresponds to the wavelength range of 3 mm to 30 μm (Abbott and Zhang 2007). The T-ray band can be described in

terms of photon energy, that is from 0.41 meV to 41 meV. The early pioneering work carried out by Auston and his coworkers (Auston *et al.* 1984, Smith *et al.* 1988, Auston and Nuss 1988, Auston 1988) led to the advent of terahertz time-domain spectroscopy (THz-TDS) in the late 1980s (van Exter *et al.* 1989). The introduction of THz-

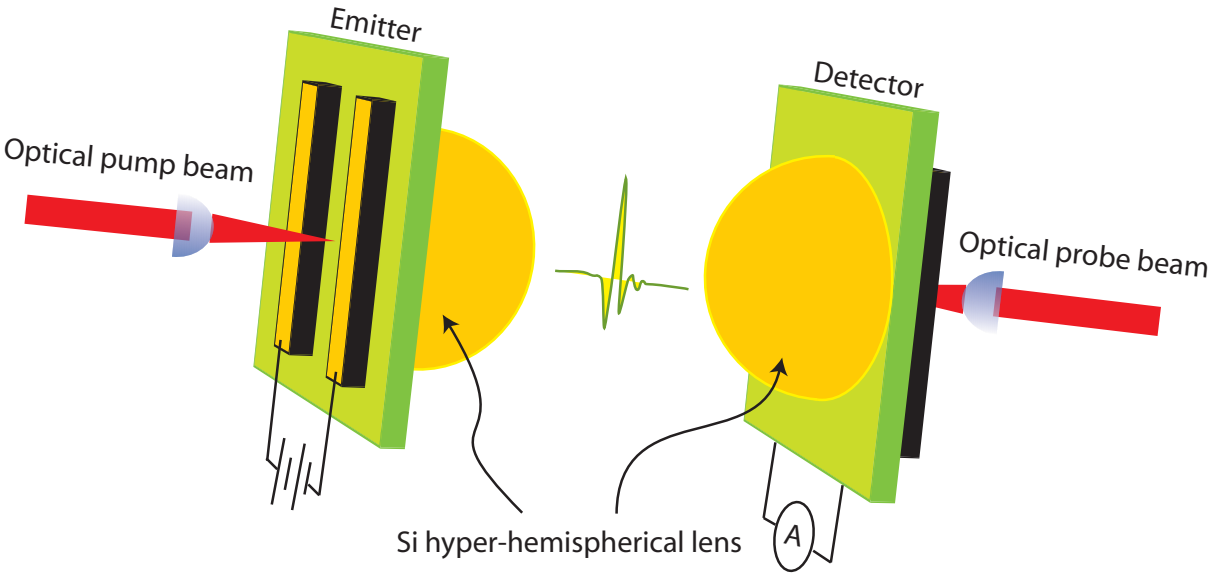

Figure 2.5. Generation and detection of THz radiation using photoconductive antennas. Schematic illustration of a typical photoconductive antenna pair for generation and detection of THz radiation. The antennas consist of parallel metal striplines with a gap of several tens of micrometres deposited on a galium arsenide (GaAs) semiconductor substrate. An optical pump beam is illuminated onto the stripline's gap of the transmitting antenna to generate photocarriers. These photocarriers are accelerated by applying a bias voltage to produce THz pulse. A silicon (Si) hyper-hemispherical lens is used for coupling and collimation purposes. On the detector, photocarriers are generated as the optical probe beam illuminates the photoconductor in the gap of a stripline antenna. The generated carriers on the detector end are driven by the incoming THz electric field, which then produces current. A silicon hyper-hemispherical lens is used at the detector to couple the incoming THz beam into the photoconductive detector.

TDS offered a new and elegant technique to explore the THz region of the electromagnetic spectrum. In general, the generation and detection of THz radiation relies on either transient photoconductivity in semiconductor materials or optical rectification in electro-optic crystals with an ultrafast femtosecond laser as a pumping source. A typical generation and detection mechanism for THz radiation using transient photoconductivity is illustrated in Fig. 2.5. Complete detail on the method of generation and detection of THz radiation based on transient photoconductivity will be discussed

in Chapter 3. Vibrational motions of organic compounds, lattice vibrations in solids, rotational transitions of molecules, and intraband transitions in semiconductors are some of the unique characteristics of a material response to THz radiation (Lee 2009). These characteristics lead to a variety of applications ranging from biomolecular spectroscopy, chemical recognition, medical imaging, communication, and security.

2.2.4 Infrared

Sir William Frederick Herschel, an English astronomer of German origin, discovered infrared radiation in the year 1800 while he was conducting an experiment with a prism in sunlight (Fig. 2.6). As the sunlight hits the prism, he found that a spectrum of visible light ranging from violet to red appeared. Herschel recorded the temperature of each colour using a thermometer and found that the temperature increases progressively from violet to red. As he moved the thermometer beyond the red end of the visible region, he found that the temperature continued to increase (Spiro and Schlessinger 1989). Thus, Herschel confirmed the presence of energy beyond the red

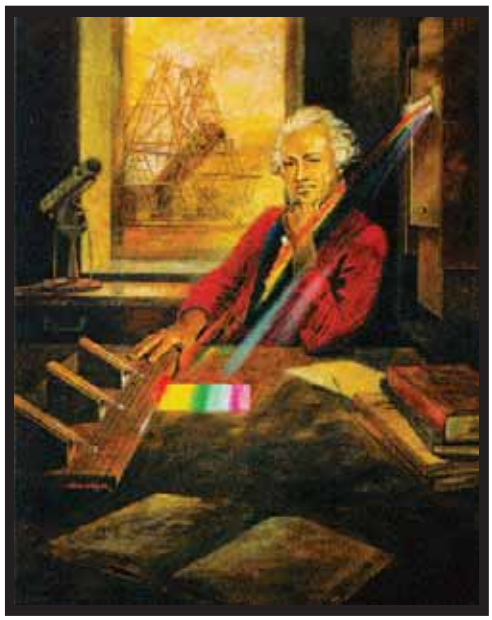

Figure 2.6. Sir William Frederick Herschel (1738 - 1822) and his experimental setup. This figure shows the picture of and his experimental arrangement for detecting infrared radiation. Adapted from Herschel (2000).

and concluded that there is an invisible form of light beyond the visible spectrum, which has come to be known as infrared (IR). Infrared radiation spans a section of the electromagnetic spectrum with frequency ranging from a few THz to approximately

0.4 PHz that is a few μm to 780 nm in wavelength (Band 2006). Infrared radiation has a photon energy ranging from 41 meV to 1.65 eV. Today, infrared is of great interest to physicists and chemists because it gives vibrational information within molecules. Furthermore, infrared is also used in imaging, short range wireless comunications, and weather forecasting.

2.2.5 Visible light

The visible band in the electromagnetic spectrum falls in the frequency range of approximately 0.4 PHz to 0.8 PHz or 1.65 to 3.3 eV with corresponding wavelengths of 780 nm - 390 nm. According to the spectrum in Fig. 1.1, visible light has a colour range from violet, the shortest wavelength, to red, the longest wavelength. In 1672, Sir Isaac Newton (Fig. 2.7) demonstrated the refraction of light using a prism (Fig. 2.8). In this experiment, he showed the decomposition of sunlight into a spectrum of colours.

Figure 2.7. Sir Isaac Newton (1643 - 1727). Adapted from Anthony (1960).

2.2.6 Ultraviolet (UV)

Following Herschel's discovery of infrared radiation beyond the red end of the visible spectrum, Johann Wilhelm Ritter (Fig. 2.9) reported the existence of ultraviolet (UV) radiation beyond the violet of the visible spectrum 1801. According to his investigation, blackening of silver chloride was not limited to visible light but extended

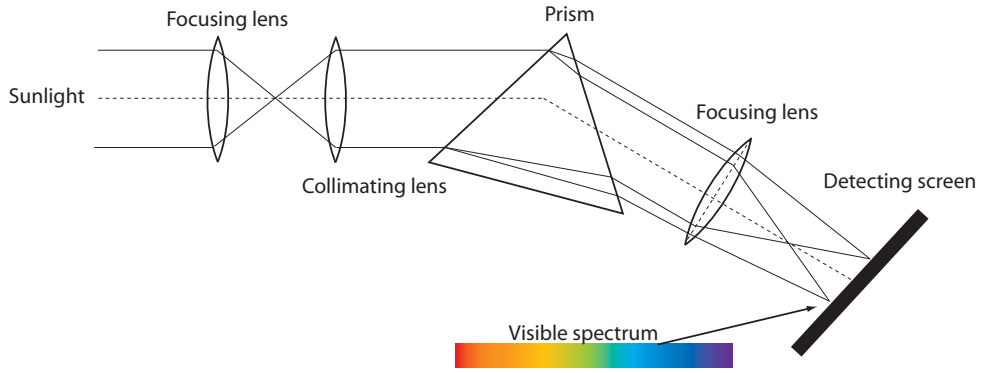

Figure 2.8. Isaac Newton's experimental setup to illustrate visible spectrum of light generated from sunlight. Adapted from Brittain *et al.* (1970).

beyond the violet end of the spectrum (Beeson and Mayer 2008, Friedberg 1997). Here, Ritter demonstrated that radiation existed at wavelengths shorter than violet. The frequency band of ultraviolet is approximately between 0.8 PHz and 0.1 EHz (or photon energy ranging from 3.3 eV to 411 eV) that is between the wavelengths of 390 nm and 3 nm (Band 2006). Moreover, UV is classified as ionising radiation due to its high photon energy that could cause harm to human health. Today, UV is widely used in applications such as pest control and food industries.

NOTE:
This figure is included on page 15
of the print copy of the thesis held in
the University of Adelaide Library.

Figure 2.9. Johann Wilhelm Ritter (1776 - 1810). Adapted from Berg (2008).

2.2.7 X-rays

On November 8, 1895, Wilhelm Konrad Röntgen (Fig. 2.10) discovered X-rays while investigating cathode rays produced in a Crookes' vacuum tube invented by Sir William Crookes in the 1870s. While he was working in a darkened room, he noticed something unusual when an electric discharge occured in his tube causing a nearby piece of paper coated with barium platocyanide to fluoresce (Simon 2004). According to Röntgen, the vacuum tube was completely covered in a black cardboard to avoid any light from leaking and reaching the coated paper.

Figure 2.10. Wilhelm Konrad Röntgen (1845 - 1923). The discoverer of X-rays. After Elizabeth (2007).

Yet, a greenish glow was observed on the coated paper. He also found that X-rays could penetrate through cardboard, wood, cloth, and a thick book but not metal. Röntgen also observed a shadow of his bones on the coated screen. Thus, Röntgen concluded that a new type of ray had been produced in the vacuum tube. In an interview, Röntgen said that this ray could not be deflected or reflected; that it could not be seen or felt. "What is it then? I know not" (Elizabeth 2007). This new ray was given the designation X, the scientific symbol for the unknown. Wilhelm Konrad Röntgen was awarded a Nobel Prize in Physics in 1901 for his discovery. Figure 2.11 shows the earliest X-ray record taken by Röntgen of his wife's hand with a ring. According to Band (2006), X-rays lie between the UV and γ-rays at approximately 0.1 EHz to 10 ZHz which corresponds to the wavelength range of 3 nm to 3 pm. The X-ray photon energy is between

411 eV and 411 keV. Such high photon energy categorises X-rays as ionising. Today, X-rays are widely used in applications such as medical imaging and security.

Figure 2.11. X-ray of Röntgen's wife's hand with a ring. This scan is known to be the world's first X-ray: the skeletal structure of his wife's hand with a ring. Adapted from Elizabeth (2007).

2.2.8 γ-rays

Paul Ulrich Villard, a French physicist (Fig. 2.12), is credited with the discovery of gamma rays (γ-rays) in 1900 while experimenting with Marie and Pierre Curie's newly discovered radioactive element radium. According to L'Annunziata (2007), the Curies found radium rays (i.e., α-rays and β-rays), emitted by highly radioactive salts of barium, are capable of converting oxygen into ozone. Furthermore, they had also reported a colouring action of the rays on glass and on barium platinocyanide that is used as a fluorescent screen. These findings motivated Villard's interest to explore the reflection and refraction properties of cathode rays and β-rays in the presence of a magnetic field (Gerward 1999). According to Villard's experimental results, β-rays behave in all respects like cathode rays. The experimental method used by Villard to measure the reflection and refraction of these rays is shown in Fig. 2.13. A sample of barium chloride containing radium in a glass ampoule is located within a lead shield that has an opening. As a magnetic field is applied to the collimated beam of radiation from the radium source, the α-rays are deviated and absorbed by the black paper wrapping of

Figure 2.12. Paul Ulrich Villard (1860 - 1934). French physicist, Paul Ulrich Villard, the discoverer of γ-rays. Adapted from Gerward (1999).

the photographic plates. The β-rays are deflected by the magnetic field and hit the first photographic plate.

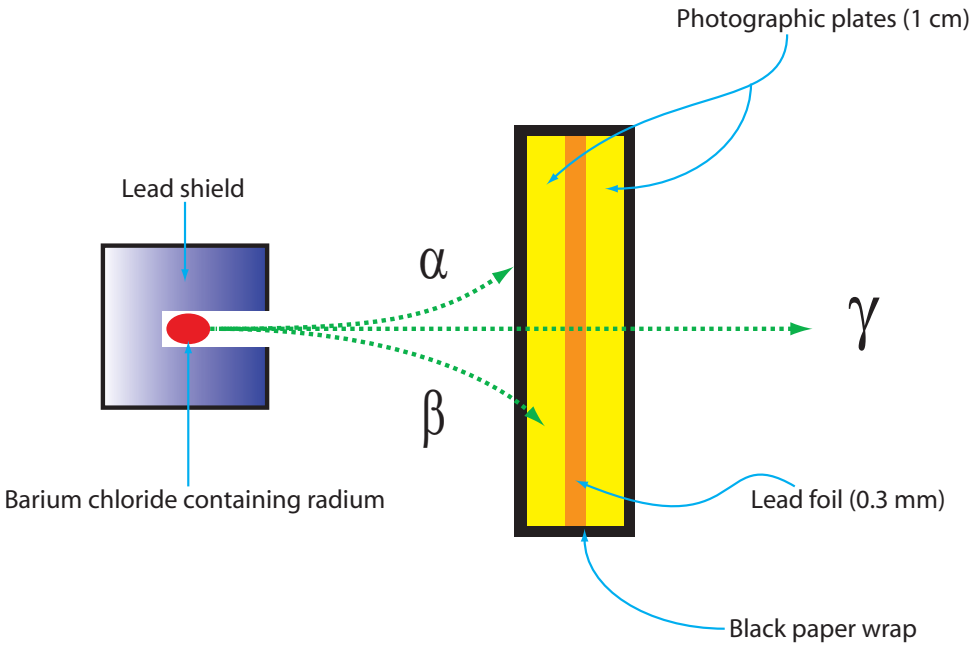

Figure 2.13. Experimental setup for γ-ray generation. Detailed description on the γ-ray generation is given in Sec. 2.2.8.

Table 2.1. Electromagnetic spectrum definitions. This table summarises each electromagnetic frequency band according to its frequency range, wavelength range, and photon energy.

EM band	Frequency	Wavelength	Photon energy
Radiowaves	$\leqslant$ 1 GHz	$\geqslant$ 30 cm	$\leqslant$ 4.1 μeV
Microwaves	1 GHz - 1 THz	30 cm - 0.3 mm	4.1 μeV - 4.1 meV
T-rays	0.1 THz - 10 THz	3 mm - 30 μm	0.41 meV - 41 meV
Infrared	a few THz - 0.4 PHz	a few μm - 780 nm	meV -1.65 eV
Visible light	0.4 PHz - 0.8 PHz	780 nm - 390 nm	1.65 eV - 3.3 eV
Ultraviolet	0.8 PHz - 0.1 EHz	390 nm - 3 nm	3.3 eV - 411 eV
X-rays	0.1 EHz - 0.1 YHz	3 nm - 3 pm	411 eV - 411 keV
γ-rays	$\geqslant$ 0.1 YHz	$\leqslant$ 3 pm	$\geqslant$ 411 keV

Moreover, Villard also observed an unknown non-deviable radiation propagating along an absolute straight line through photographic plates and 0.3 mm lead foil in the presence of a magnetic field. The unknown radiation was strongly penetrating and also known to have a much shorter wavelength than X-rays, which then was named gamma rays (γ-rays) by Rutherford in 1903 (Gerward 1999, L'Annunziata 2007). According to Band (2006), γ-rays are defined as the region of the electromagnetic spectrum above 0.1 YHz with the highest photon energy of above 411 keV, which corresponds to wavelengths below 3 picometres.

2.3 Chapter summary

In this chapter, the historical development of the electromagnetic spectrum has been discussed. A summary of each electromagnetic frequency band is given in Table 2.1. This sets the historical context for now introducing T-rays. In the following chapter, a detailed description of T-rays, which are relatively unexplored is given. Methods of generation and detection using transient photoconductivity are discussed.

Chapter 3

Terahertz time-domain spectroscopy (THz-TDS)

THE generation and detection techniques for terahertz radiation have advanced remarkably in the past two decades with the advent of ultrashort femtosecond lasers. In this chapter, a fundamental overview of the basic principles of terahertz time-domain spectroscopy (THz-TDS) is given. A method of generation and detection of terahertz radiation based on transient photoconductivity is discussed. A comprehensive terahertz-TDS data analysis technique is described.

3.1 Introduction

What is terahertz (THz) or T-ray radiation? According to the definition from the electromagnetic spectrum in Fig. 1.1, THz covers the spectral range from 0.1 THz to 10 THz overlapping the microwave and infrared regions. The advent of femtosecond lasers led researchers to generate and detect coherent THz radiation based on an optically-gated detection technique that allows the measurement of the transient electric field, and not only the intensity as in case of the traditional far-infrared sources. With the measurements of the transient electric field, one can determine both the real and imaginary parts of the dielectric function of a medium without having to carry out a Kramers-Kronig analysis.

In 1984, Auston *et al.* (1984) showed a first demonstration of generation and detection of THz radiation based on photoconductive antennas. In their experimental setup, a colliding-pulse passively modelocked (CPM) ring dye laser with a pulse duration of 100 fs was used to illuminate a pair of 10 μm gap transmitting and receiving dipole antennas that were located symmetrically on opposite sides of a thin dielectric slab. With this setup configuration, they produced a terahertz pulse with a duration of approximately 1.6 ps propagating in space from the point of generation to detection (Auston *et al.* 1984). In the late 1980s, van Exter *et al.* (1989) described the first application of the terahertz system by analyzing the propagation of the terahertz pulses through water vapour. Today, this is also known as a terahertz time-domain spectroscopy (THz-TDS) system.

Several different types of THz-pulse emitting and detecting devices, such as electro-optic (EO) emitters and detectors, have been developed. In principle, the generation and detection of THz radiation relies on either a transient photoconductivity in a semiconductor material or optical rectification in electro-optic crystals with an ultrafast femtosecond laser as a pumping source. Both the generation and detection techniques are widely used by the THz community. In this Thesis, the generation and detection of THz radiation using transient photoconductivity are presented.

3.1.1 Objectives and framework

In this chapter fundamental principles of THz-TDS using a transient photoconductivity for emission and detection of pulsed THz radiation are outlined. This chapter is

structured as follows: In Sec. 3.2, the principles of terahertz pulse emission and detection based on photoconductive antennas are introduced. The types of photoconductive antennas used in our setup are described in detail. Moreover, the transmission THz-TDS experimental configuration is explained in this section. A typical analytical formula used for signal extraction is described in Sec. 3.3 followed by a brief discussion and validation of the results obtained via measurement of a polymer sample under test.

3.2 Principles of terahertz pulse emission and detection

3.2.1 Terahertz pulse emission using photoconductive emitters

Figure 3.1 illustrates a standard THz radiation generation scheme using a photoconductive antenna. An ultrashort femtosecond laser is illuminated onto a stripline structured coplanar transmission line that is fabricated on a GaAs semiconductor substrate. Photocarriers are generated within the semiconductor when the ultrashort femtosecond laser with photon energy greater than the bandgap energy of the semiconductor is focused near the anode of the striplines. A transient photocurrent is formed as the photo-generated carriers are accelerated at an enormous rate by a DC-biased electric field and a decay with the time constant given by the carrier lifetime of the semiconductor. A silicon (Si) hyper-hemispherical lens is attached to the back of the semiconductor for coupling the resulting transient pulse into free space. Also, the lens is used for increasing the collimation of the transient electromagnetic pulse.

Simple analytical model for terahertz generation using photoconductive switch

In this section, we demonstrate a simple analytical model for terahertz generation using a photoswitch emitting (tx) antenna. The time-dependent photocurrent density in the emitter is expressed as the convolution of the optical laser pulse and the impulse response of the photoswitch (Duvillaret *et al.* 2001, Lee 2009),

$$j_{\mathrm{tx}}(t) = P_{\mathrm{opt}}(t) * [n_{\mathrm{tx}}(t) q v_{\mathrm{tx}}(t)] \, . \tag{3.1}$$

Here, $P_{\mathrm{opt}}(t)$ is the incoming femtosecond laser pulse. The $n_{\mathrm{tx}}(t)$, q, and $v_{\mathrm{tx}}(t)$ are denoted as density, charge, and velocity of the photocarriers respectively. The dynamics of the time-dependent carrier density under an impulsive optical excitation is given by

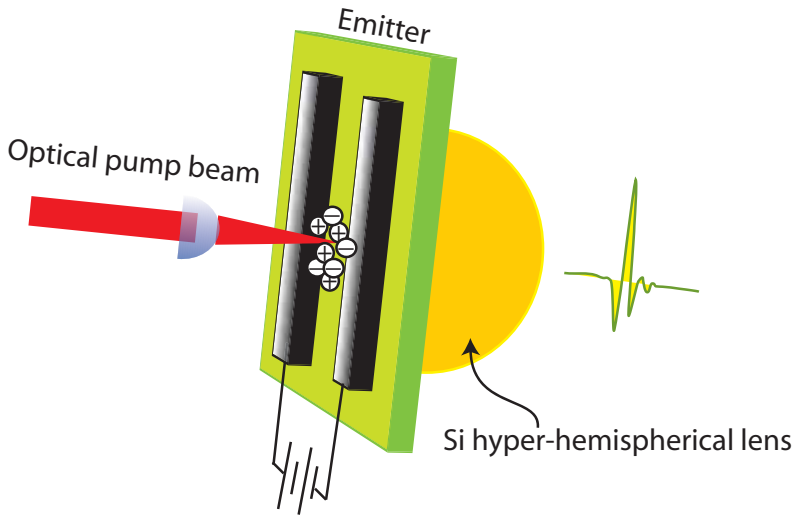

Figure 3.1. Transmitting photoconductive switch. This figure depicts a schematic illustration of a transmitting photoconductive switch. It consists of a DC-biased two parallel metal striplines embedded in a GaAs semiconductor substrate. A typical value of the stripline separation is 30-200 μm. Photocarriers are created as the femtosecond laser is incident near the stripline anode. Here, the generated photocarriers are accelerated by the DC bias that then creates transient photocurrent.

the following equation (Piao *et al.* 1999, Lee 2009):

$$\frac{dn(t)}{dt} = -\frac{n(t)}{\delta\tau_c} + \delta(t)\ , \tag{3.2}$$

where τ_c denotes the carrier lifetime and $\delta(t)$ is the impulsive optical excitation. Based on the Drude-Lorentz model, the average velocity of the carriers accelerated in the bias electric field is given as follows (Duvillaret *et al.* 2001):

$$\frac{dv(t)}{dt} = -\frac{v(t)}{\delta\tau_s} + \frac{q}{m}E(t)\ , \tag{3.3}$$

where τ_s is the carrier scattering time and m denotes the effective mass of the carriers, and $E(t)$ is the constant DC bias field. We suppose that the temporal profile of the femtosecond laser is Gaussian with a pulse duration of τ_{las}. Thus, substituting the carrier density and average carrier velocity derived from Eqs. 3.2 and 3.3 into Eq. 3.1 gives the following equation (Duvillaret *et al.* 2001):

$$\begin{aligned} j_{tx}(t) \propto \int_0^\infty \frac{P_{tx}}{\tau_{las}} E_{DC} \exp\left(-\frac{4\ln 2(t-t')^2}{\tau_{las}^2}\right) \\ \times \exp\left(-\frac{t'}{\tau_{tx}}\right)\frac{\delta\tau_{tx}}{m_{tx}}\left(1-\exp\left(-\frac{t'}{\delta\tau_{tx}}\right)\right)dt'\ . \end{aligned} \tag{3.4}$$

Here, τ_{tx} denotes the carrier lifetime and P_{tx} is the average incident power. In a typical dipolar emitting antenna, the THz radiated electric field, $E_{THz}(t)$ is directly proportional to the temporal derivative of the transient photocurrent generated in the transmitting antenna (Duvillaret *et al.* 2001, Hoffmann 2006, Piao *et al.* 1999),

$$E_{THz}(t) \propto \frac{dj_{tx}(t)}{dt} . \tag{3.5}$$

With references to Eqs. 3.4 and 3.5, one could plot the time-dependent photocurrent and the THz radiated electric field as shown in Fig. 3.2.

NOTE:
This figure is included on page 25
of the print copy of the thesis held in
the University of Adelaide Library.

Figure 3.2. Photocurrent and electric field amplitude of the THz radiation as a function of time. This figure illustrates the photocurrent and the THz radiated electric field as a function of time obtained based on a simple analytical model described in Eqs. (3.1 - 3.5). The fitting parameters are obtained from Duvillaret *et al.* (2001).

3.2.2 Terahertz pulse detection using a photoconductive detector

The THz detection principle of a photoconductive antenna is almost identical to the THz emission principle. Figure 3.3 shows a typical H-structured dipole photoconductive antenna. Here, the electrodes are connected to a lock-in amplifier to measure current instead of connecting it to a DC bias voltage source. An ultrashort femtosecond laser is focused onto the 5 μm wide gap between the electrodes to generate photocarriers within the semiconductor. The photocarriers are then accelerated by the incoming electric field of the focused THz radiation, which are then detected as a photocurrent

by the lock-in amplifier. The photocurrent detected is proportional to the incident THz radiation. Repetitive photoconductive sampling is required to measure the THz transient due to the lack of fast electronics to capture the fast signals. Moreover, to reproduce the terahertz wave generated by the emitter, the carrier lifetime of the detecting photoconductive antenna has to be much shorter than the THz pulse so that it acts as a gated sampling signal. Thus, the entire THz pulse can be mapped out by introducing an optical delay line on the femtosecond laser. The average photocurrent, j_{rx} detected with the photoconductive antenna for a relative time delay, τ, can be expressed by the convolution of the transient conductance, $\sigma(t)$ and the incident THz radiation, $E_{THz}(t)$ across the photoconductor (Park *et al.* 1999):

$$j_{rx}(\tau) \propto \int E_{THz}(t)\sigma(t-\tau)dt\ . \tag{3.6}$$

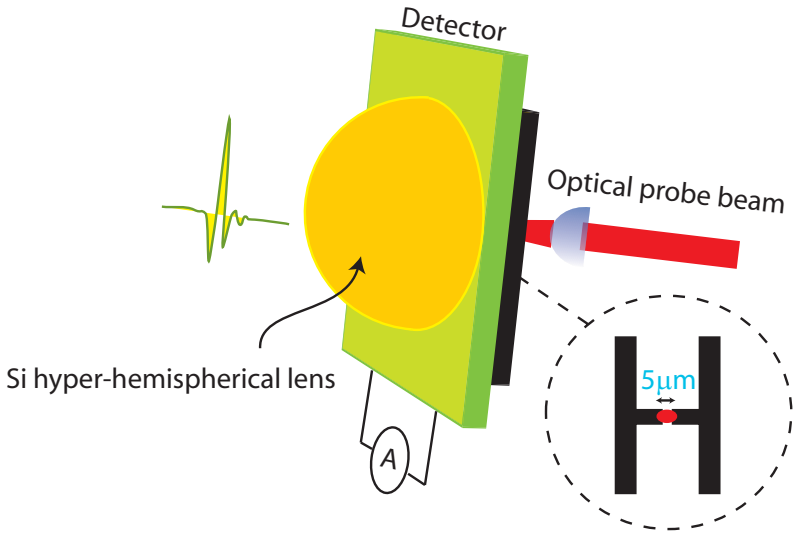

Figure 3.3. H-structured photoconductive detector switch. This figure shows a schematic illustration of a 5 μm gap H-structured detecting photoconductive switch. A Si hyper-hemispherical lens is used for coupling of the incoming THz beam into the photoconductive detector. As the THz radiation and the ultrashort femtosecond laser incident onto the 5 μm gap receiving antenna synchoronously, a photocurrent is generated. A low noise lock-in amplifier is used to capture the photocurrent for signal processing.

Simple illustration of repetitive photoconductive sampling at the detector

An illustration of repetitive THz pulse detection is shown in Fig. 3.4. According to Eq. 3.6, the detected photocurrent is the convolution of the transient conductance and the incident THz radiation. This explanation covers only one segment of the sampling

described in Fig. 3.4. However, due to lack of fast electronics, repetitive photoconductive sampling is required at each delay point, which then results in an averaged photocurrent signal (Fig. 3.4a). Thus, the averaged photocurrent at each delay point is used to map out the THz transient (Fig. 3.4b).

3.2.3 Photoconductive antennas

The photoconductive antennas used in our transmission-mode THz setup are described in this section. Figure 3.5a shows a commerically available single stripline pair of GaAs photoconductive antenna from Zomega Terahertz Corporation. This antenna has a gap width of 200 μm between two metal striplines. This allows a bias voltage of approximately 100 Vpp and maximum power rating of 400 mW. Figure 3.5b depicts a multiple 5 μm gap width H-structured silicon-on-sapphire (SOS) photoconductive antenna built-in one chip. This antenna is obtained from The University of Freiburg. It has a maximum power rating of approximately 20 mW with low bias voltage. In our setup, we use the stripline pair as an emitter and the H-structure as a detector. These antennas are mounted on a specially designed antenna mounts, which will be described in Sec. 3.2.5.

3.2.4 THz-TDS configuration

In this section, we outline a basic technique of transmission mode THz time-domain spectroscopy (THz-TDS) system based on photoconductive antennas. A typical transmission mode THz-TDS system is shown in Fig. 3.6. A MiraSeed (Coherent) Ti-sapphire femtosecond modelocked laser is used as a source of the optical pulses. It is pumped by the Verdi (Coherent) V6 with a wavelength of 532 nm. According to the MiraSeed's laser manual, the femtosecond laser produces an output pulse duration of approximately 20 fs at a repetition rate of 76 MHz. The laser has an output power of 1 W with a center wavelength of 800 nm. The femtosecond source is split into a probe beam and a pump beam using a non-polarised 50:50 beamsplitter. An optical chopper with SR540 controller is used to modulate the pump beam at approximately 2 kHz. The modulated beam is then focused onto the emitting stripline photoconductive antenna using a 6 mm diameter plano-convex optical lens that has a focal length of 12 mm. Here, the photoconductive antenna is at 90 Vdc using a standard low current power supply. As the modulated laser beam hits the emitter, a THz pulse is generated. The THz pulse

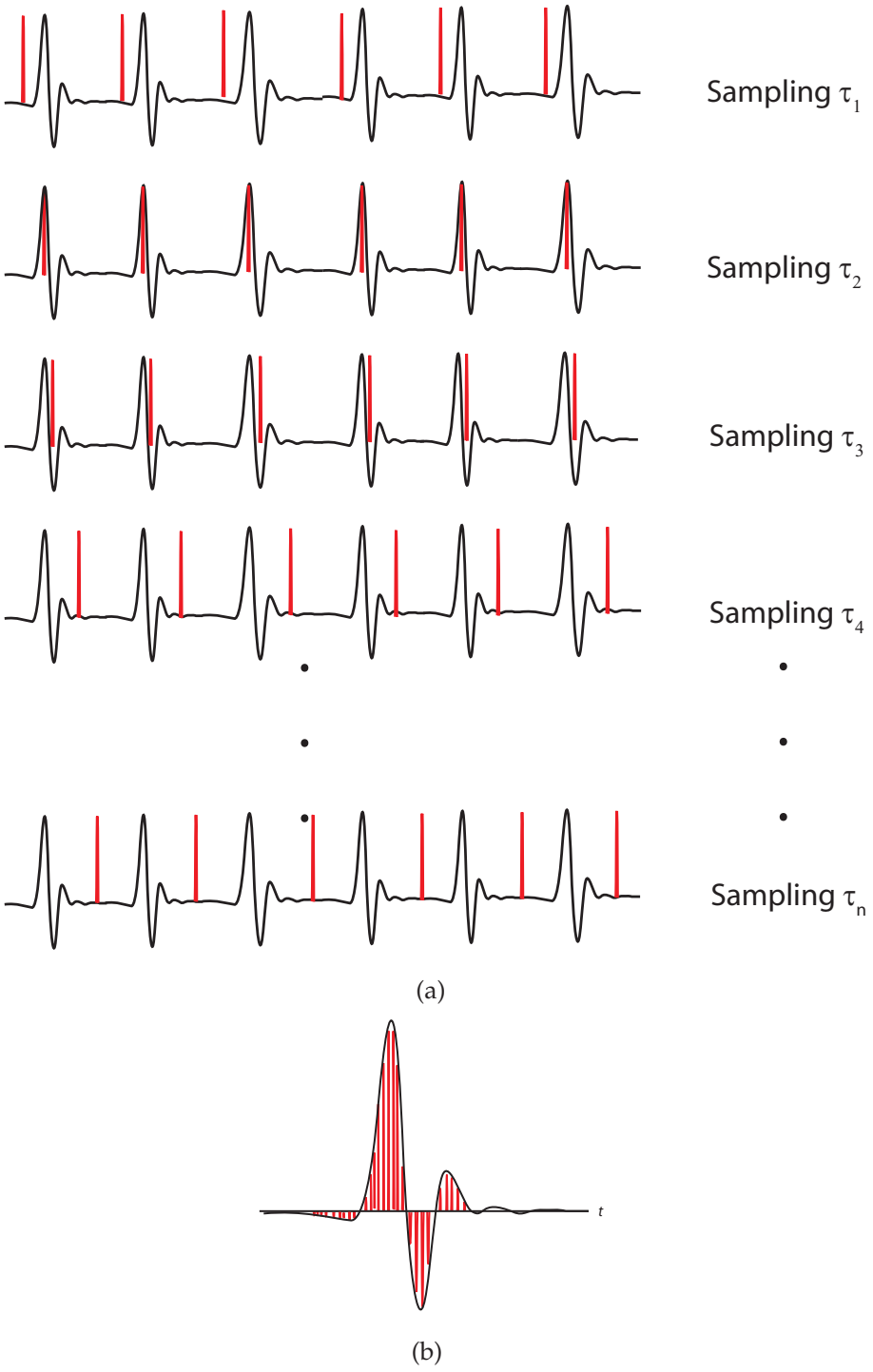

Figure 3.4. Illustration of repetitive sampling with variable delay. This figure depicts the schematic illustration of repetitive sampling. (a) shows the repetitive sampling at varying time delay. Here, an averaged photocurrent is produced at each delay point. This averaged photocurrent is then used to plot the averaged THz pulse (b).

is coupled and collimated into free space using a Si hyper-hemispherical lens, which

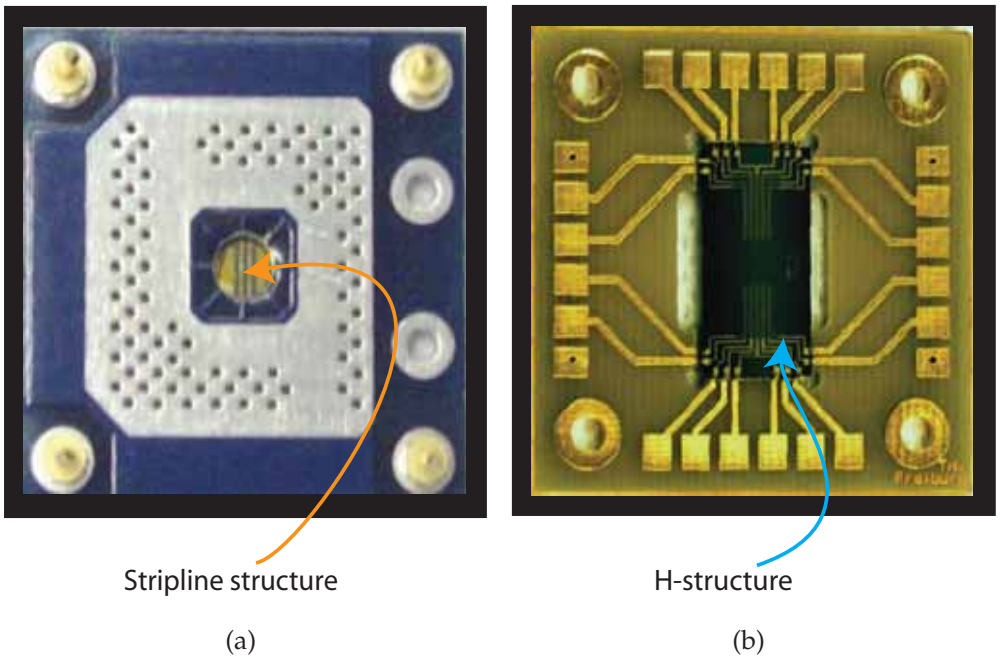

Figure 3.5. Photoconductive antennas. This figure shows the photoconductive antennas used in our setup. (a) depicts the stripline photoconductive antenna from Zomega THz Corp. The stripline pair deposited on the GaAs semiconductor is directly attached onto a printed circuit board (PCB) without the need for wire bonding. (b) illustrates the H-structured photoconductive antenna from The University of Freiburg. Here, the metal H-structure is deposited onto a silicon-on-sapphire (SOS) semiconductor.

is then further collimated using a pair of off-axis 90° paraboloidal mirrors. The collimated THz beam is focused onto the sample as shown in Fig. 3.6. The transmitted pulse is then recollimated and refocused onto the photoconductive detector using a second pair of off-axis 90° paraboloidal mirrors. In Fig. 3.6, the paraboloidal mirrors are arranged according to a $f - 2f - 2f - 2f - f$ geometry. The probe beam gates the transmitted THz pulse by focusing the probe laser beam using a plano-convex lens onto the photoconductive detector. The averaged THz pulse can be sampled by varying the time delay of the retroreflector mounted onto a delay stage. A lock-in amplifier model SR830 is used to extract the signal received at the detector. Signal analysis and data processing are carried out using LabVIEW and Matlab software packages (See Appendix C & D).

Component list of the THz-TDS spectrometer

The components used in the spectrometer illustrated in Fig. 3.7 are listed as follows:

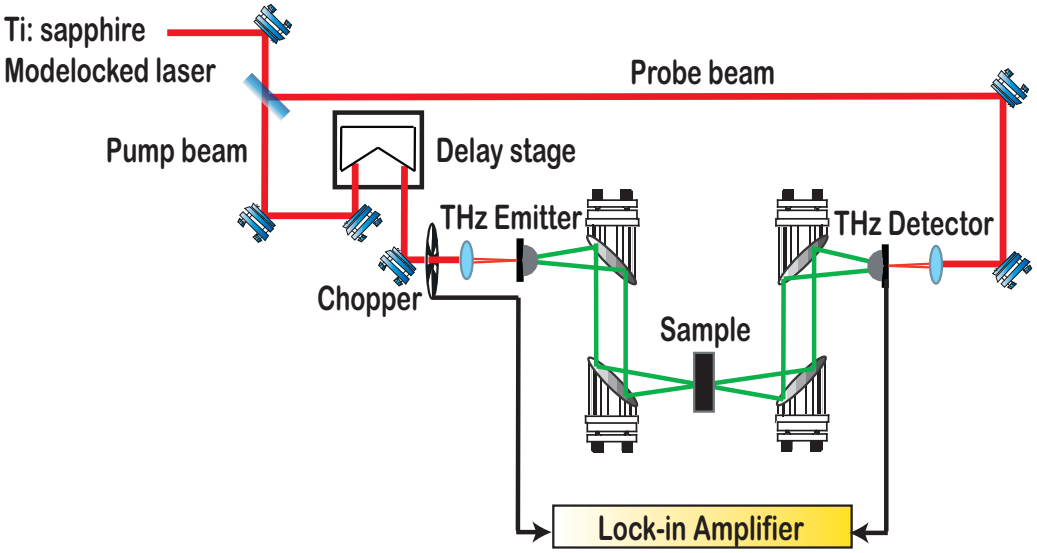

Figure 3.6. THz time domain spectrometer. This schematic diagram shows a typical THz-TDS spectrometer used in our lab. The sample under test is placed at the focal plane.

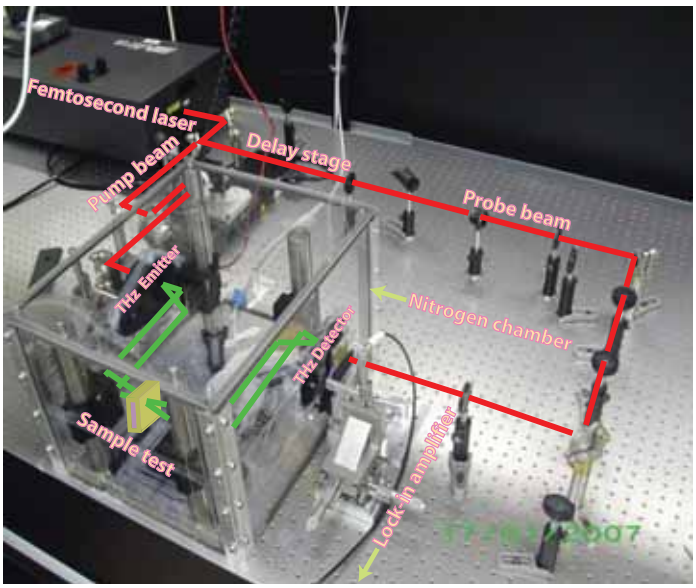

Figure 3.7. Custom built THz time-domain spectrometer. This figure illustrates a custom-built THz-TDS spectrometer. It was built from scratch by the author for the research in this thesis. The ultrashort femtosecond laser is highlighted in red and the terahertz beam is highlighted in green. A custom-built nitrogen chamber is designed for this spectrometer.

- MiraSeed (Coherent) Femtosecond Modelocked Ti: Sapphire laser
- Diode-Pumped laser (Coherent) Verdi V6 (not shown)
- XPS motion controller
- ILS linear stage – (Newport)
- SR540 chopper controller with 30 slots chopper blade
- SR830 lock-in amplifier
- Zomega stripline GaAs photoconductive antenna as an emitter
- Freiburg H-structured SOS photoconductive antenna as a detector
- Standard biasing power supply
- Paraboloidal mirrors – (Edmund Optics)
- Retroreflector – (Edmund Optics)
- Plano convex lens – 6 mm diameter with a focal length of 12 mm
- Custom-built plano convex lens holder
- IR filters (Newport)
- XYZ stages – (Newport)
- Non-polarised beamsplitter – (Thorlabs)
- Custom-built antenna mount modules
- Valumax mirrors – (Newport)

Temporal electric field and spectral amplitude

The temporal electric field and its corresponding spectral amplitude obtained from the THz-TDS spectrometer illustrated in Fig. 3.7 are shown in Fig. 3.8. Figure 3.8a, shows a typical temporal profile of a reference signal. In Fig. 3.8b, the spectral amplitude is obtained by fast Fourier transforming the temporal profile. Since this measurement was conducted in ambient atmosphere, the presence of various water lines can be clearly

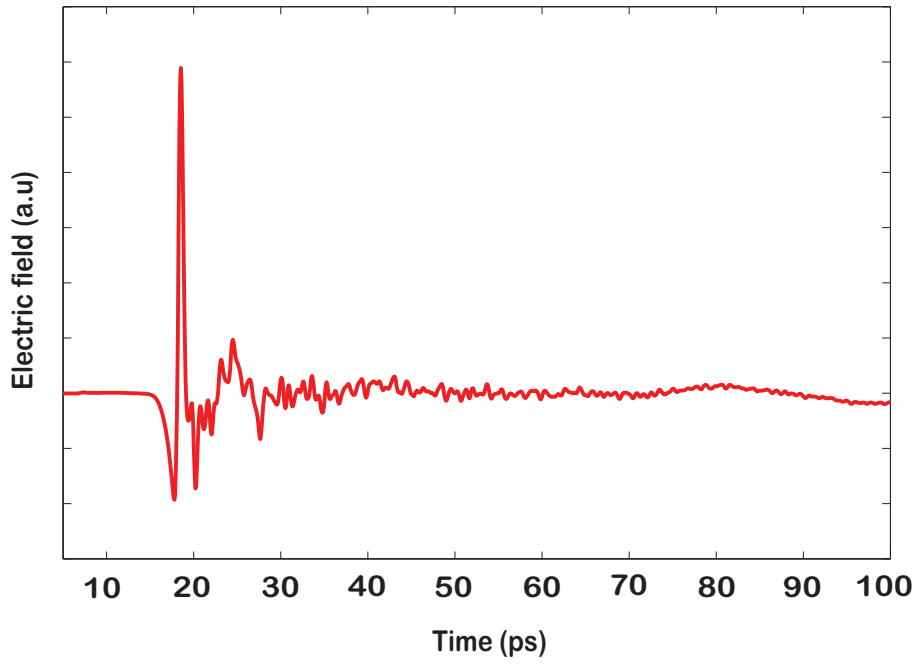

(a)

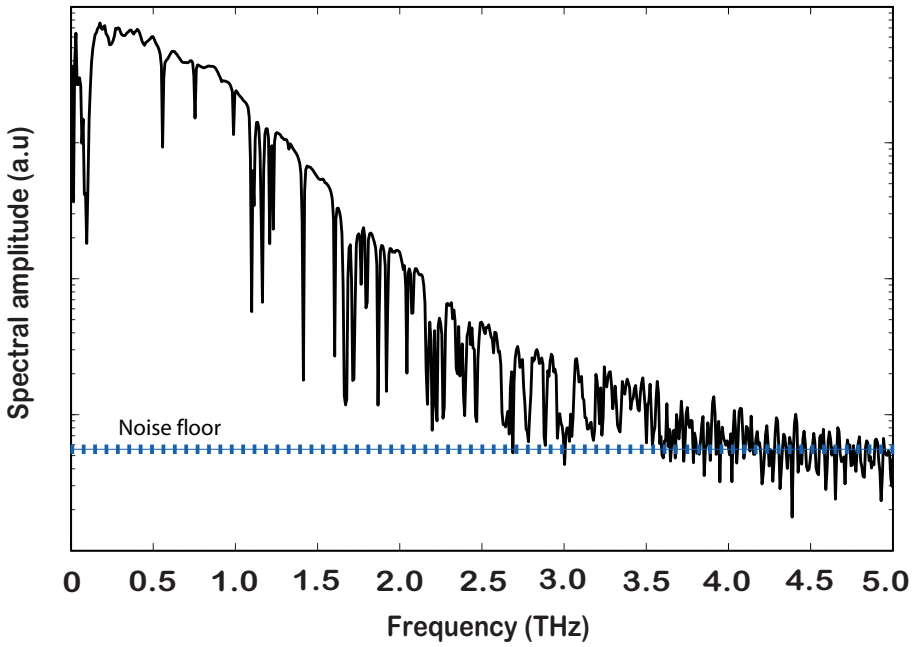

(b)

Figure 3.8. Typical temporal profile and spectral amplitude. This figure illustrates (a) a typical temporal profile of a reference signal and (b) its corresponding spectral amplitude of our transmission setup. A bandwidth of up to 3.5 THz is obtained from our experimental setup illustrated in Fig. 3.7. The presence of water lines is clearly identified in Table 3.1.

seen. Table 3.1 summarises the presence of water lines in our setup. Here, we compare the water lines in our work with that in the literature and we find an excellent agreement with the published work. According to Fig. 3.8b, a bandwidth of approximately 3.5 THz is achieved in our setup configuration. Here, the bandwidth is mainly controlled by the pulse width of the optical source (i.e., femtosecond laser), carrier lifetime of the photoconductive antenna, and also the water vapour absorption. Therefore, in order to maximise bandwidth, a femtosecond laser with a pulse width of approximately 20 fs and photoconductive antennas made of material such as GaAs and SOS (i.e., described in Fig. 3.5) that have a very short carrier lifetime are used. Furthermore, the water line effects can be reduced by purging the nitrogen chamber with nitrogen gas.

3.2.5 Novel antenna mounts

A novel custom-built antenna mount module is illustrated in Fig. 3.9. This module is used for hinging the photoconductive antenna described in Fig. 3.5. The module is made of five main different parts including: XY stage, hemispherical lens slider, antenna slider, supply voltage adapter, main body, and base plate. The XY stage is composed of two single-axis stages mounted on each other to form XY directions. The hemispherical lens slider is attached to the XY stage for adjusting the Si hyper-hemispherical lens. Here, the Si hyper-hemispherical lens is mounted onto the lens slider as shown in Fig. 3.9a. A teflon polymer material is used to hold the Si hyper-hemispherical lens. Furthermore, the use of teflon prevents damages to the Si hyper-hemispherical lens. The photoconductive antenna mounted on a PCB is glued to the antenna slider for height adjustments. The entire mount is supported by the main body and a base plate for clamping purposes. The antenna mount modules for both the transmitter and the detector are similar, however, the Bayonet Neill-Concelman (BNC) adapter at the emitter is connected to a bias supply voltage whereas the BNC adapter at the detector is linked to the lock-in amplifier. The back view of the antenna mount is shown in Fig. 3.9b. The cables connected to the BNC connectors are made as short as possible to avoid noise interference.

Table 3.1. Water lines in THz regime. The frequencies of known water lines in the range of approximately 0.2 THz to 3.5 THz are shown. Water lines obtained from our measurement are visually compared with Lucia (2003), National Physical Laboratories (NPL), and Sandia National Laboratories (SNL). An excellent match is demonstrated.

Lucia (2003)	In this work	NPL [1]	SNL [2]
0.234 THz	✓	✓	–
0.440 THz	✓	✓	✓
0.556 THz	✓	✓	✓
0.750 THz	✓	✓	✓
0.988 THz	✓	✓	✓
1.113 THz	✓	✓	✓
1.099 THz	✓	✓	✓
1.165 THz	✓	✓	✓
1.208 THz	✓	✓	✓
1.230 THz	✓	✓	✓
1.326 THz	✓	✓	✓
1.414 THz	✓	✓	✓
1.604 THz	✓	✓	✓
1.670 THz	✓	✓	✓
1.720 THz	✓	✓	✓
1.765 THz	✓	✓	✓
1.794 THz	✓	✓	✓
1.868 THz	✓	✓	✓
1.919 THz	✓	✓	✓
2.021 THz	✓	✓	✓
2.043 THz	✓	✓	✓
2.073 THz	✓	✓	✓
2.168 THz	✓	✓	✓
2.197 THz	✓	✓	✓
2.227 THz	✓	✓	✓
2.263 THz	✓	✓	✓
2.322 THz	✓	✓	✓
2.351 THz	✓	✓	✓
2.366 THz	✓	✓	✓
2.395 THz	✓	✓	✓
2.432 THz	✓	✓	–
2.468 THz	✓	✓	✓
2.571 THz	✓	✓	✓
2.644 THz	✓	✓	✓
2.666 THz	✓	✓	✓
2.688 THz	✓	✓	–
2.783 THz	✓	✓	–
2.886 THz	✓	✓	–
2.959 THz	✓	✓	–
3.003 THz	✓	✓	–
3.032 THz	✓	✓	–
3.047 THz	✓	✓	–
3.179 THz	✓	✓	–
3.215 THz	✓	–	–
3.230 THz	✓	–	–
3.340 THz	✓	–	–
3.501 THz	✓	–	–
3.538 THz	–	–	–

[1] NPL – National Physical Laboratories (Naftaly and Dudley 2009)

[2] SNL – Sandia National Laboratories (Foltynowicz *et al.* 2005)

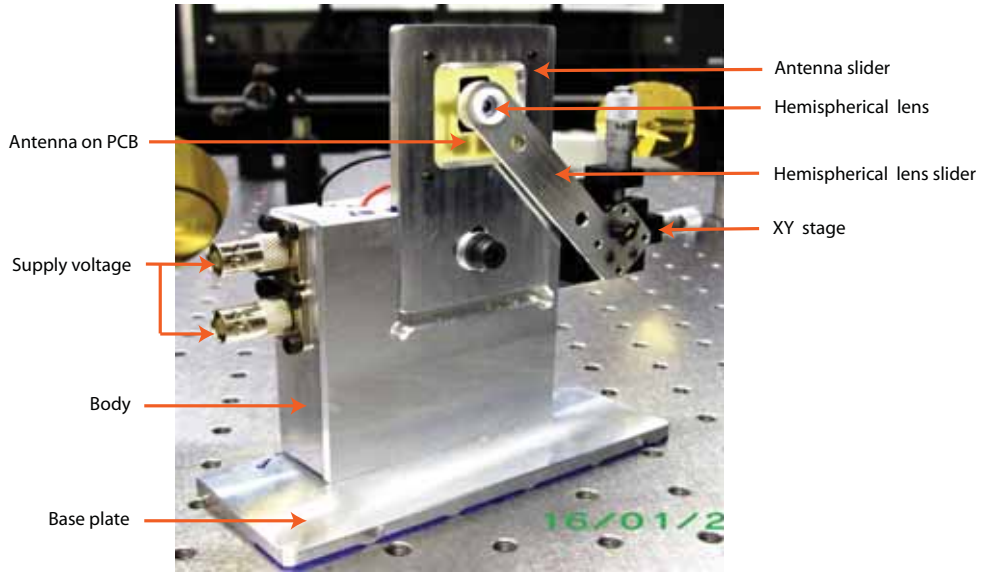

(a) Front view

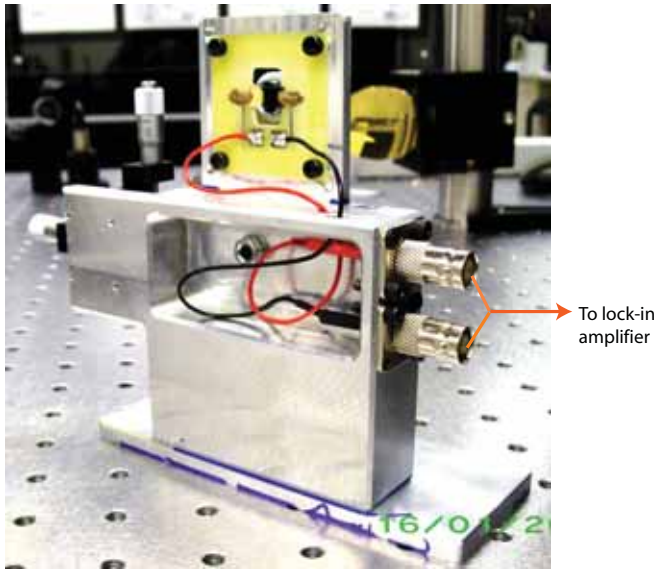

(b) Back view

Figure 3.9. Novel custom-built antenna mount module. This figure depicts our custom-built antenna mount module made of aluminium. The detailed description of this module is given in Sec. 3.2.5.

3.3 Data analysis

Since the early days of terahertz, dielectric properties of a wide variety of materials including: gases, semiconductors, explosives, and liquids have been studied. Here, the dielectric properties of a material are determined by measuring the temporal profiles of the terahertz pulses twice: one measurement without sample in the terahertz beam

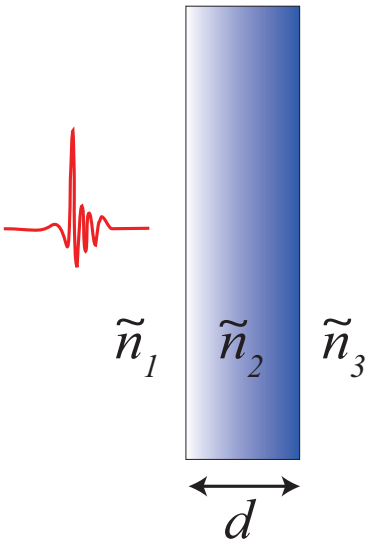

Figure 3.10. Homogeneous sample test. This figure depicts a homogeneous sample test with a thickness of d, and refractive index, $\tilde{n}_2$. Here, $\tilde{n}_1 = \tilde{n}_3 = 1$, denotes the refractive index of air.

path denoted as $E_{\text{reference}}(t)$, and another one with sample in the terahertz beam path denoted as $E_{\text{sample}}(t)$. Fast Fourier transforming of the temporal profiles, $E(t)$, reveals the complex amplitude spectra, $E(\omega)$. A complex transmission coefficient of the sample can be obtained by taking the ratio of the complex amplitude spectra of the sample, $E_{\text{sample}}(\omega)$, and the reference, $E_{\text{reference}}(\omega)$. Based on the complex transmission coefficient of the sample, the dielectric properties of the sample can be extracted. In the following section, the assumption and the dielectric properties extraction method are described.

3.3.1 Assumption and method of extraction

Prior to sample measurements, several assumptions have to be made in order to standardize the measurement technique. The assumptions made are as follows:

- The sample is sufficiently thick to avoid Fabry-Pérot reflection
- The sample is homogeneous without scattering
- The terahertz radiation is normal incident to the sample.

Figure 3.10 shows an example design of a sample test. Based on the assumptions made, one can determine the frequency dependent complex spectral component of the terahertz signal transmitted through the sample as follows (Duvillaret *et al.* 1996):

$$\widetilde{E}_{\text{sample}}(\omega) = T_{12}(\omega) \cdot\ P_2(\omega, d) \cdot\ T_{23}(\omega) \cdot\ A(\omega) \cdot \text{FP}(\omega)\ . \tag{3.7}$$

For sample oriented normal incidence to the THz beam path, the propagation equations can written as follows (Duvillaret *et al.* 1996):

$$T_{\text{ab}}(\omega) = \frac{2\tilde{n}_{\text{a}}}{\tilde{n}_{\text{a}} + \tilde{n}_{\text{b}}}\ , \tag{3.8}$$

$$R_{\text{ab}}(\omega) = \frac{\tilde{n}_{\text{a}} - \tilde{n}_{\text{a}}}{\tilde{n}_{\text{a}} + \tilde{n}_{\text{b}}}\ , \tag{3.9}$$

where $T_{\text{ab}}(\omega)$ is the transmission amplitude coefficient from medium a to medium b and $R_{\text{ab}}(\omega)$ is the reflection amplitude coefficient from medium a to medium b. The $P_{\text{a}}(\omega, d)$ denotes the propagation coefficient in medium a over thickness d,

$$P_{\text{a}}(\omega, d) = \exp\left(-j\frac{\tilde{n}_{\text{a}}\omega d}{c}\right)\ , \tag{3.10}$$

where c is the speed of light. Also, $A(\omega)$ accounts for the amplitude of each frequency component. The $\text{FP}(\omega)$, Fabry-Pérot reflection term in Eq. 3.7 is the multiple reflections between two plane parallel interfaces shown in Fig. 3.10. For large number of multi-reflections between the two parallel interfaces, the $\text{FP}(\omega)$ can be approximated by (Duvillaret *et al.* 1996)

$$\text{FP}(\omega) = \frac{1}{1 - \text{R}_{21}\text{R}_{23}\exp\left(-j\frac{\tilde{n}_2\omega d}{c}\right)}\ , \tag{3.11}$$

which can be written as

$$\text{FP}(\omega) = \frac{1}{1 - (\frac{\tilde{n}_2 - \tilde{n}_1}{\tilde{n}_2 + \tilde{n}_1})(\frac{\tilde{n}_2 - \tilde{n}_3}{\tilde{n}_2 + \tilde{n}_3}) \cdot \exp\left(-j\frac{\tilde{n}_2\omega d}{c}\right)}\ . \tag{3.12}$$

The Fabry-Pérot reflections only become crucial in thin samples. Here, in order to avoid complications from the $\text{FP}(\omega)$, it is assumed that the sample under test is sufficiently thick so that the Fabry-Pérot reflections can be isolated.

The frequency dependent complex spectral component of the terahertz signal transmitted through the air is given below (Duvillaret *et al.* 1996):

$$\widetilde{E}_{\text{reference}}(\omega) = T_{13}(\omega) \cdot \; P_{\text{air}}(\omega, d) \cdot \; A(\omega) \; . \tag{3.13}$$

Therefore, the ratio of the above $\tilde{E}_{\text{sample}}(\omega)$ and $\tilde{E}_{\text{reference}}(\omega)$ produces a complex transmission coefficient,

$$\tilde{T}(\omega) = \frac{\tilde{E}_{\text{sample}}(\omega)}{\tilde{E}_{\text{reference}}(\omega)} = \rho e^{-j\phi} \; . \tag{3.14}$$

Here, ρ is defined as a magnitude and ϕ as a phase. With the refractive index of air $\tilde{n}_1 = \tilde{n}_3 = 1$, Eq. 3.14 can be simplified as follows:

$$\frac{\tilde{E}_{\text{sample}}(\omega)}{\tilde{E}_{\text{reference}}(\omega)} = \frac{4\tilde{n}_2(\omega)}{(\tilde{n}_2(\omega)+1)^2} \exp(-j\frac{\omega d}{c}(\tilde{n}_2(\omega)-1)) \cdot \text{FP}(\omega) \; . \tag{3.15}$$

According to Mickan *et al.* (2002b), the complex refractive index of a sample can be estimated using an iterative approximation or analytically. For sufficiently thick sample, the $\text{FP}(\omega)$ term given in the above equations can be easily isolated. Thus, one may extract the n and κ of the sample analytically (Duvillaret *et al.* 1999). By subtituting the complex refractive index of the sample, $\tilde{n}_2 = n_2 - j\kappa_2$ into Eq. 3.15, the magnitude, ρ can be written as follows:

$$\rho(\omega) = \frac{4n_2(\omega)}{(n_2(\omega)+1)^2} \exp\left(-\frac{\omega d \kappa_2}{c}\right) \; , \tag{3.16}$$

and the phase, ϕ as:

$$\phi(\omega) = \frac{\omega d}{c}(n_2(\omega)-1) \; . \tag{3.17}$$

Therefore, the index of refraction can be obtained by rearranging Eq. 3.17,

$$n_2(\omega) = 1 + \frac{c\phi(\omega)}{\omega d} \; . \tag{3.18}$$

Rearranging Eq. 3.16 produces the extinction coefficient as follows:

$$\kappa_2(\omega) = -\frac{c}{\omega d} \ln \left(\frac{(n_2(\omega)+1)^2}{4n_2(\omega)} \rho(\omega) \right) . \tag{3.19}$$

Thus, the absorption coefficient can be defined as

$$\alpha(\omega) = 2\frac{\kappa(\omega)\omega}{c} , \tag{3.20}$$

which can also be written as follows:

$$\alpha(\omega) = -\frac{2}{d} \ln \left(\frac{(n_2(\omega)+1)^2}{4n_2(\omega)} \rho(\omega) \right) . \tag{3.21}$$

Phase unwrapping

In order to calculate index of refraction, (n) and subsequently the absorption coefficient, (α), a phase information, (ϕ) is required. The phase information obtained directly from the measurement is not continuous however, and has jumps of 2π (Hoffmann 2006). In order to obtain continuous phase greater than or above 2π, we unwrapped the original phase information. Simple Matlab code for phase unwrapping is given below.

$$\texttt{phase} = \texttt{unwrap}(\texttt{angle}(\texttt{transmission})) , \tag{3.22}$$

where `transmission` denotes the complex transmission coefficient, $\tilde{T}(\omega)$, and `angle` refers to the wrapped phase information. It is stated by Duvillaret *et al.* (1996) that the signal at the lower frequency end is very small relative to the noise. This means that the relative amplitudes of the sine and cosine components at the lower frequency end are dominated by the noise. Therefore, the unwrapping method given in Eq. 3.22 may end up distorting the phase information at low frequencies due to noisy signal. One may overcome this problem by artificially linear extrapolating the distorted phase at the low frequencies (Duvillaret *et al.* 1996).

Figure 3.11 shows an example of data analysis process of a 3 mm thick PMMA polymer sheet using the experimental setup described in Fig. 3.7. This experiment is conducted in a nitrogen purged environment to remove water lines interference. Fig. 3.11a depicts

the temporal profiles of the reference and sample pulses. The sample pulse is attenuated and a time delay is introduced as compared to the reference pulse. Fig. 3.11b shows corresponding spectral amplitudes of reference pulse and sample pulse after the fast Fourier transform process. The unwrapped phase with ringing at the low frequencies (in black) and an extrapolated phase (in cyan) are shown in Fig. 3.11c. For further detail on phase unwrap and extrapolation procedures, please refer to the Matlab code given in Appendix D. The absolute transmission coefficient of PMMA in the terahertz regime is described in Fig. 3.11d. Fig. 3.11e and Fig. 3.11f show the refractive index and absorption coefficient obtained based on the spectal amplitudes and the phase information illustrated in Fig. 3.11b and Fig. 3.11c. A detailed description on the THz dielectric properties of PMMA will be given in Chapter 4 and 5.

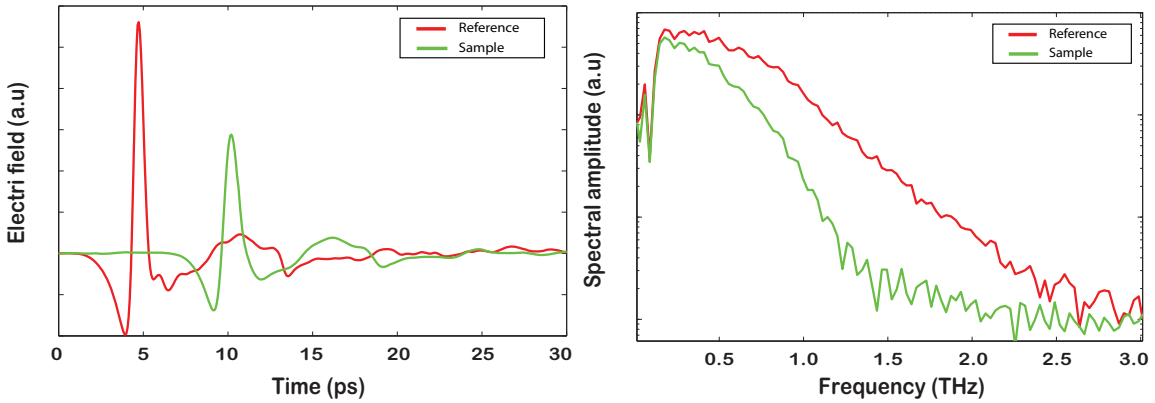

(a) Temporal profile

(b) Spectral amplitude

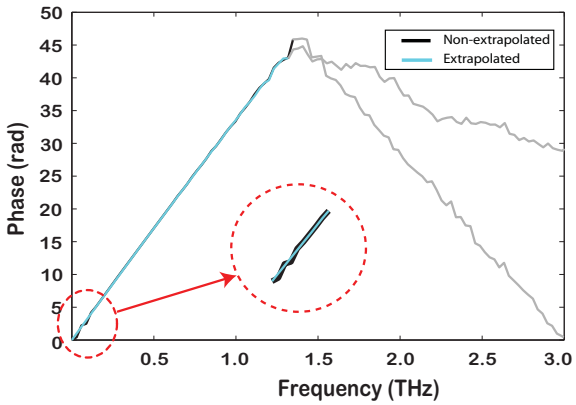

(c) Phase

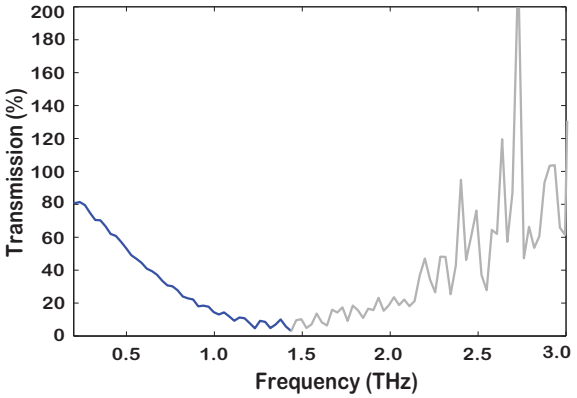

(d) Absolute transmission coeffcient

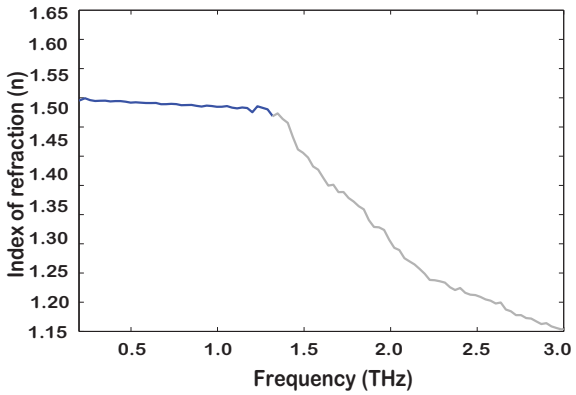

(e) Refractive index

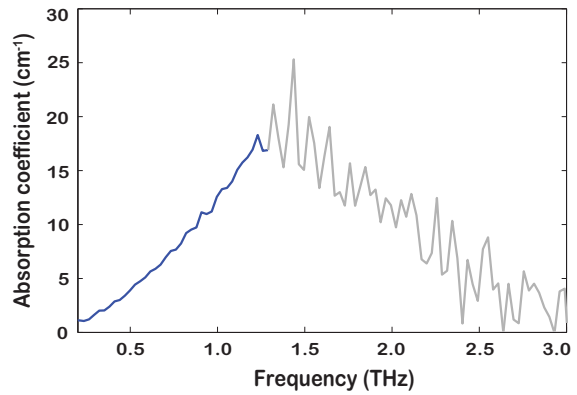

(f) Absorption coefficient

Figure 3.11. Terahertz data analysis procedures for a 3 mm PMMA polymer sheet. This figure illustrates step-by-step data analysis proceduces based on Eqs. 3.7 – 3.18 to determine the dielectric properties of a sample under test (i.e., 3 mm PMMA sheet). The measurement results match well with the literature presented in Piesiewicz *et al.* (2007a) and Jin *et al.* (2007).

3.4 Chapter summary

In this chapter, we have presented a detailed description on the generation and detection of terahertz radiation based on transient photoconductivity. A comphrehensive data analysis technique is described. Here, we have validated the measurement technique by measuring the THz properties of a PMMA polymer sheet. The THz-TDS experimental configuration and analytical formulas for signal extraction described in this chapter will be used in the following chapters of this Thesis.

Characterising the THz dielectric properties of a range of polymers with a view of identifying a suitable window material is crucial for the development of the fixed dual-thickness window spinning technique described in Ch. 8. This is further elaborated in detail in the following chapter.

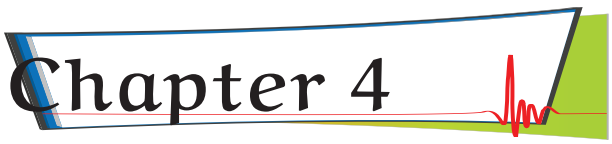

THz dielectric properties of polymer materials

POLYMER materials are commonly used as sample holder windows for THz experiments. In this chapter, we report experimental results of the THz dielectric properties of various polymer materials obtained through the THz-TDS system described in Sec. 3.2.4 and verify the results with the literature. The motivation of this chapter is to characterise a range of polymers with a view to identifying the best THz window material for the development of the fixed dual-thickness window spinning wheel technique presented in Ch. 8.

4.1 Brief introduction on macromolecules or polymers

Polymers in the form of plastics, rubbers, and fibres have played an important role in everyday life since the early 1800s. The first truly commercial process for the production of polymer materials from cellulose nitrate (celluloid) was made by John Hyatt of Albany, New York State (1868) (Ebewele 1996). Hyatt invented the celluloid billiard ball, which is still in use today. Since then, many developments in polymers have been made. However, a clear understanding of the molecular structure of polymers was not made till 1920. In the early 1920s, Hermann Staudinger, a German organic chemist (Fig. 4.1), formulated a macromolecular concept to describe a molecular structure of polymers (Gedde 1999). Staudinger showed that polymers were made of giant chainlike molecules, rather than aggregates of small molecules that give the false impression of giant molecules. He named these giant molecules *macromolecules*. A macromolecule or a polymer is a very large molecule made up of many small units linked together. These individual units are called monomers. Fig. 4.2a shows a single molecule (monomer) known as ethylene that has the ability to combine with identical molecules to create a polymer chain, known as polyethylene, as shown in Fig. 4.2b. The graphical representation of the polyethylene polymer chain is illustrated in Fig. 4.3. Following the groundwork laid by Staudinger, in 1896, his theory was further supported by Wallace Carothers who then invented nylon in 1935 (Teegarden 2004).

Figure 4.1. Hermann Staudinger (1881-1965). Staudinger discovered the structure of polymers. Adapted from Staudinger (2003).

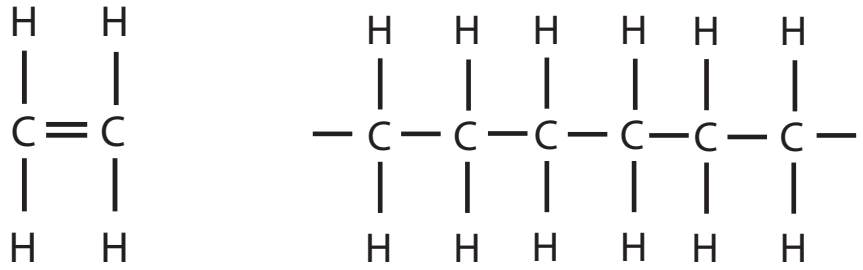

Figure 4.2. Monomer and polymer structures of ethylene. This figure depicts a simple representation of monomer and polymer structures of ethylene. Here, each carbon atom forms two single bonds with other carbon atoms and two single bonds with hydrogen atoms.

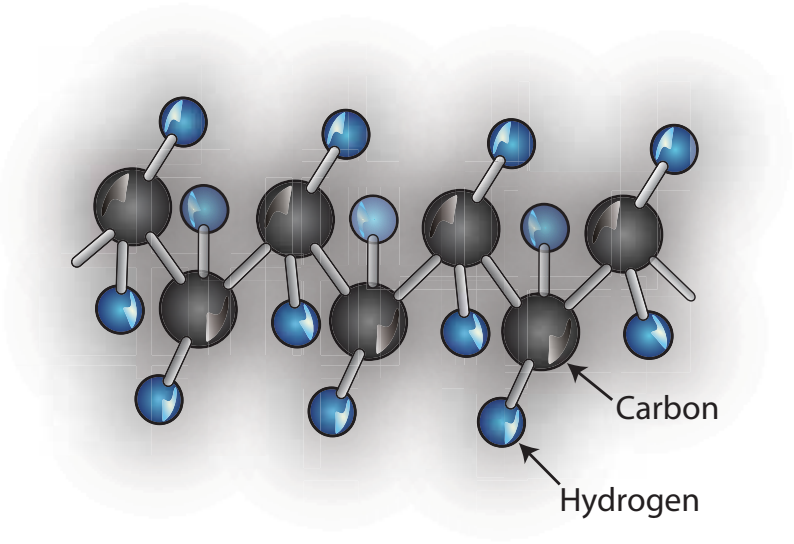

Figure 4.3. Structure of polyethylene. This figure illustrates a graphical representation of polymer chain of ethylene.

4.1.1 Objectives and framework

This chapter investigates and verifies the THz dielectric properties of polymer materials with a view to identifying optimal THz window material for the development of the fixed dual-thickness spinning wheel technique. The chapter is arranged as follows: In Sec. 4.2, thermoplastic and thermoset polymers are introduced. Here, various chain branches of thermoplastic and thermoset polymers are described. In the following section, the chemical and physical properties of polymer materials such as HDPE,

PTFE, COC, PMMA, and PC are elaborated, followed by the THz dielectric properties of these materials.

4.2 Polymers today

Polymer materials are used throughout the industrial world for a variety of different purposes in the chemical, pharmaceutical, and manufacturing industries. Polymers can be divided into two groups: thermoplastic polymers and thermoset polymers. Thermoplastic polymers are those which undergo no permanent change on heating. Once formed, a thermoplastic polymer can be heated and reformed again. This type of polymer facilitates recycling. In contrast, thermoset polymers are irreversible once formed, i.e. they cannot be reshaped by heating (Cheremisinoff 1989).

The thermoplastic polymers are typically categorized as linear chain polymers (Fig. 4.4a) and branched chain polymers (Fig. 4.4b), whereas the thermoset polymers are categorized as crosslinked chain polymers (Fig. 4.4c). Based upon the arrangement of the molecular chains, the polymer characteristics, such as toughness, viscocity, and glass transition temperature, can be determined. The molecular chain arrangement shown

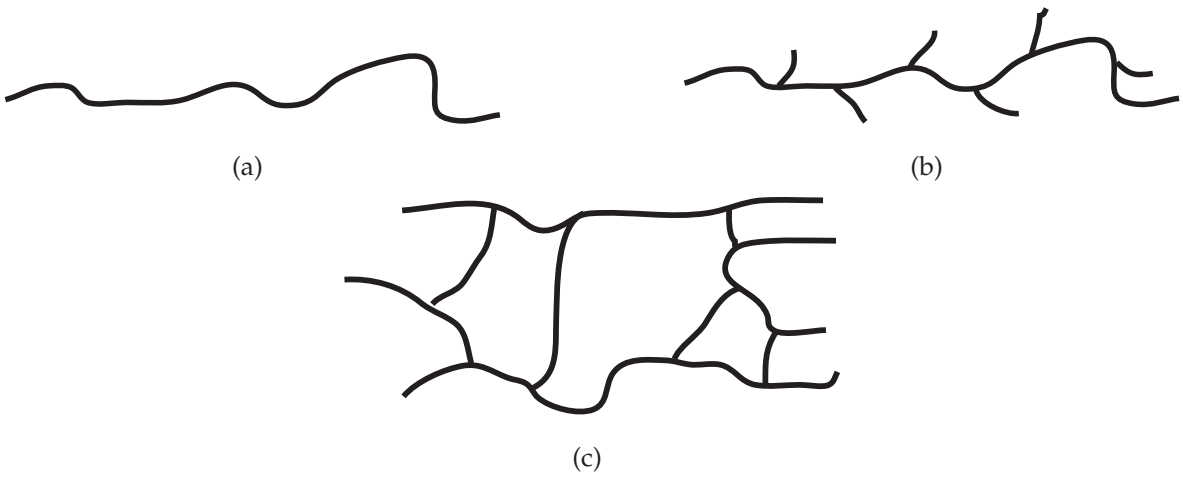

Figure 4.4. Molecular chain representation of thermoplastic and thermoset polymers. This figure demonstrates a simple representation of linear, branched, and crosslinked chains found in thermoplastic polymers and thermoset polymers.

in Fig. 4.4 can be further characterised by its morphology. According to Housecroft and

Constable (2006), morphology is defined as a form and a shape of a substance. Polymers have characteristically amorphous and semicrystalline morphologies. Semicrystalline morphology shows a high degree of order formed by folding and stacking of the polymer chains, whereas amorphous morphology is formless and the polymer chains are entangled in random coils.

In this chapter, our focus will be on linear chain thermoplastic polymer materials. Thus, from now on, it will be assumed that the polymer materials used in this chapter are linearly chained unless otherwise stated. A simplified classification of linearly chained thermoplastic polymer materials, used in this chapter, is illustrated in Fig. 4.5.

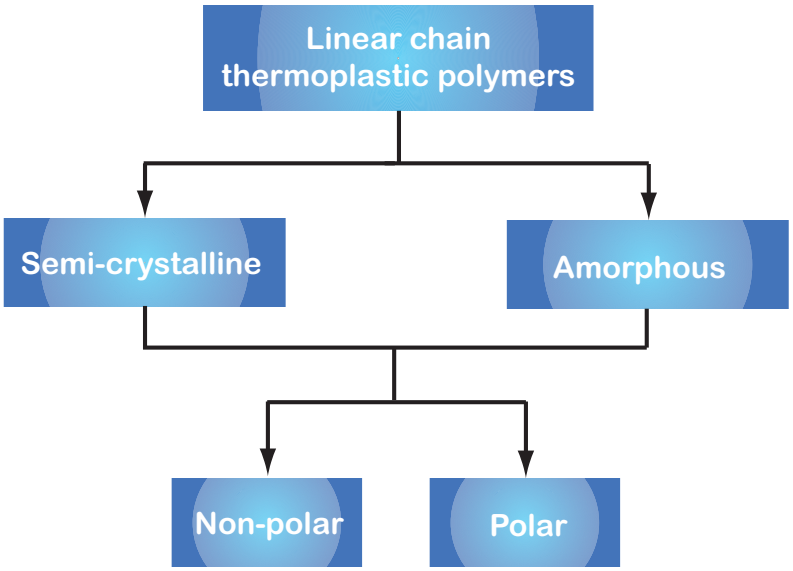

Figure 4.5. Classification of linear chain thermoplastic polymers. This diagram classifies linear chain thermoplastic polymers into semicrystalline and amorphous morphologies. Semicrystalline polymers show a high degree of order formed by folding and stacking of the polymer chains. In amorphous polymers, the molecules are oriented randomly and are intertwined, much like cooked spaghetti. These types of polymers can be further subcatergorised into polar and non-polar polymers. More details on polar and non-polar polymers can be found in Ch. 5.

4.3 Polymer T-ray spectroscopy

Since the discovery of the macromolecular concept, there has been a great interest in characterising the details of the structural properties of a polymer material. Various

analytical methods have been introduced to characterise chemical structures of polymers including: UV-visible absorption spectroscopy, Fourier transform infrared spectroscopy (FTIR), Raman spectroscopy, and nuclear magnetic resonance (NMR). Each spectroscopic technique has a range of applications. In this section, the relatively unexplored T-ray spectroscopic technique described in Chapter 3 is employed to characterise linear chain thermoplastic polymer materials in the low terahertz frequency range extending from 0.2 THz to 2.0 THz. The correct choice of polymer as a sample holder or window material is of significance for a transmission-mode THz-TDS system and is of particular interest for THz liquid spectroscopy.

4.3.1 High density polyethylene (HDPE)

Polyethylene is generally classified into several categories according to its density and branching. Here, we describe the high density polyethylene (HDPE) that is a non-polar thermoplastic polymer, discovered by Karl Zieglar in 1954 (Wittcoff *et al.* 2004). According to the polymer classification scheme of Fig. 4.5, HDPE is categorised as a linear molecular chain polymer, which means that the molecular chains are closely packed. An abundance of closely packed polymer chains results in a tough material of moderate stiffness. HDPE is characterised as a semicrystalline polymer, made up of crystalline regions and amorphous regions.

In terms of thermal characteristics, HDPE has a melting point at approximately 120°C (HDPE 2009), which indicates that this polymer can be used for relatively high temperature applications. Generally, HDPE is visually opaque due to its blurry white colour. A terahertz spectroscopy of HDPE reveals the dielectric properties; absorption coefficient (α) and refractive index (n). In Fig. 4.6a, absorption coefficient of HDPE is illustrated. Based on Fig. 4.6a, one can say that the absorption coefficient, α for HDPE is less than 2.0 cm^{-1}. According to Chantry (1971), a sharp absorption peak lies at 2.2 THz. This peak can be clearly seen when the polymer is cooled down to a very low temperature, whereas Fig. 4.6a is obtained at room temperature. Since HDPE is categorised to be semicrystalline, the presence of an absorption peak at 2.2 THz is due to low-energy intermolecular vibrations of crystalline regions. Here, the sharp absorption peak at 2.2 THz is also known as phonon absorption. Chantry (1971), also presented the absorption coefficient of HDPE at room temperature, however, the sharp absorption peak is spread out due to the vibrational activity of the molecules. In our measurement on

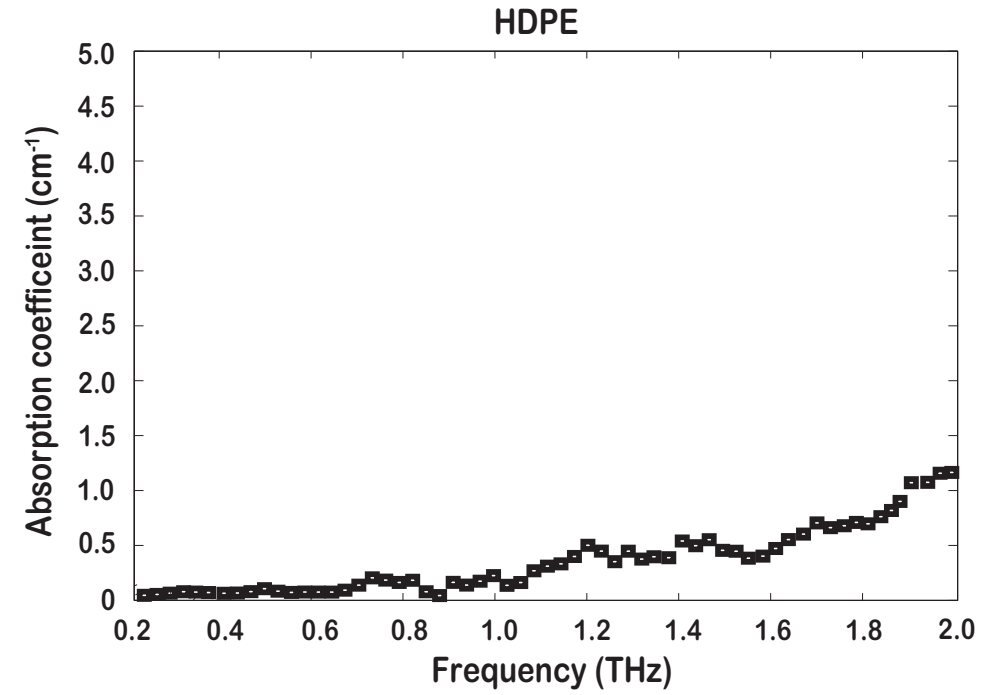

(a)

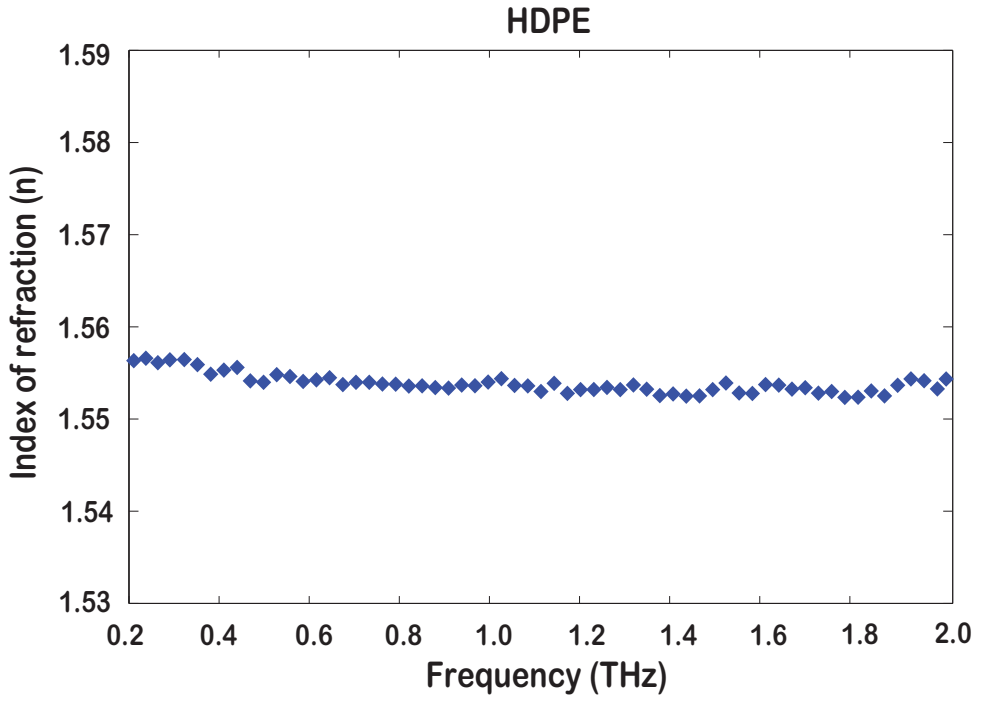

(b)

Figure 4.6. Absorption coefficient (α) and refractive index (n) spectra of HDPE. This figure depicts the absorption coefficient and refractive index of HDPE at room temperature. The absorption coefficient for HDPE is below 2 cm^{-1} and the refractive index is approximately between 1.55 and 1.56, which coincides with the optical refractive index.

HDPE, a continuum absorption with the increase in frequency is seen. The continuum rise in absorption is mainly caused by the amorphous regions of the polymer. Also, due to the limited dynamic range, no absorption peak is observed.

4.3.2 Polytetrafluoroethylene (PTFE)

Polytetrafluoroethylene (PTFE) was discovered by Roy J. Plunkett of DuPont in 1938, while attempting to make new chlorofluorocarbon (CFC) refrigerant (Ebnesajjad 2003). In today's industries, PTFE is widely used in applications such as non-stick frying pan surfaces, and medical equipment. Note that PTFE is a linear polymer formed by monomers of tetrafluoroethylene. This polymer is the completely fluorine-subtituted analogue of polyethylene (Fig. 4.7). Also, PTFE is known to have a helical chain con-

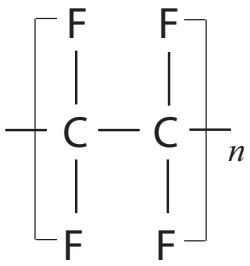

Figure 4.7. Repeating units of PTFE. This figure depicts a simple representation of repeated n units of PTFE. Here, each carbon atom forms two single bonds with other carbon atoms and two single bonds with fluorine atoms.

formation as compared to a planar zigzag chain in PE. As a result, the intermolecular forces present in PTFE differ from HDPE. The melting point of PTFE is known to be at 300°C (PTFE 2009), which indicates that this polymer can also be used for high temperature applications. PTFE is a white solid with a waxy appearance, which makes it visually opaque.

The terahertz transmission properties of PTFE are illustrated in Fig. 4.8. According to Fig. 4.8a, absorption coefficient is below 4 cm^{-1} and index of refraction is approximately 1.43. According to Klöpffer (1984), several phonon absorption peaks have been noticed in PTFE at cooled temperatures. These peaks are due to highly crystalline structures of PTFE (Bershtein and Ryzhov 1994). Furthermore, among the observed peaks, a split on the peak at 1.7 THz has been observed (Bershtein and Ryzhov 1994, Chantry *et al.* 1974). According Chantry *et al.* (1974), this split is caused the presence of

two PTFE chains per unit cell. Spectroscopic measurements conducted at room temperature reveal that all absorption peaks observed at cool temperatures diffuse due to strong molecular vibration modes (Bershtein and Ryzhov 1994, Chantry *et al.* 1974). In our measurements, PTFE shows a broad absorption profile at room temperature, thus agrees well with the literature. According to the literature and our measurements, it is obvious that PTFE may not be suitable as a window material at cooled temperatures due to its strong phonon absorption peak. In contrast, this material is highly recommended as a window material for applications at room temperature and above due to the absence of the phonon absorption peaks.

4.3.3 TOPAS Cyclic-olefin copolymer (COC) 5013L10 & 6013S04

A thermoplastic cyclic olefin copolymer (COC) is a relatively new class of polymeric material composed of ethylene and norbornene monomers (Fig. 4.9). Moreover, COC is a non-polar amorphous transparent copolymer possessing a cyclic olefin structure. Note that TOPAS™ is the trade name of a COC developed by Topas Advanced Polymer GmbH. It is known that COC possesses attractive properties from the perspective of optical clarity, low birefringence, low moisture absorption, low refractive index, high chemical resistance and heat deflection, and relatively high glass transition temperature (Shin *et al.* 2005). There are several types of COC grades based on different types of monomers and physical properties. However, in our investigation, we only consider COC grades 5013L10 and 6013S04. According to the manufacturer's specifications, COC grades 5013L10 and 6013S04 are excellent candidates for the use in the optical field. Generally, COC 5013L10 has a high flowability, which allows a precision molding and an excellent mold transferability. The COC 6013S04 is superior in its mechanical strength as compared to COC 5013L10 (Polyplastics 2009).

Application for COC in the terahertz region was first discovered by the University of Freiburg (Fischer *et al.* 2005c). Extensive studies on COC as a window material have been conducted (Fischer *et al.* 2005b, Balakrishnan *et al.* 2009b, Sengupta *et al.* 2006) since then. The terahertz properties of COC 5013L10 and COC 6013S04 are illustrated in Fig. 4.10 and Fig. 4.11 respectively. According to Fig. 4.10a, the absorption coefficient stay below 2 cm^{-1} and the refractive index is approximately 1.53 in Fig. 4.10b. As for COC 6013S04, the absorption coefficient is similar to COC 5013L10, however,

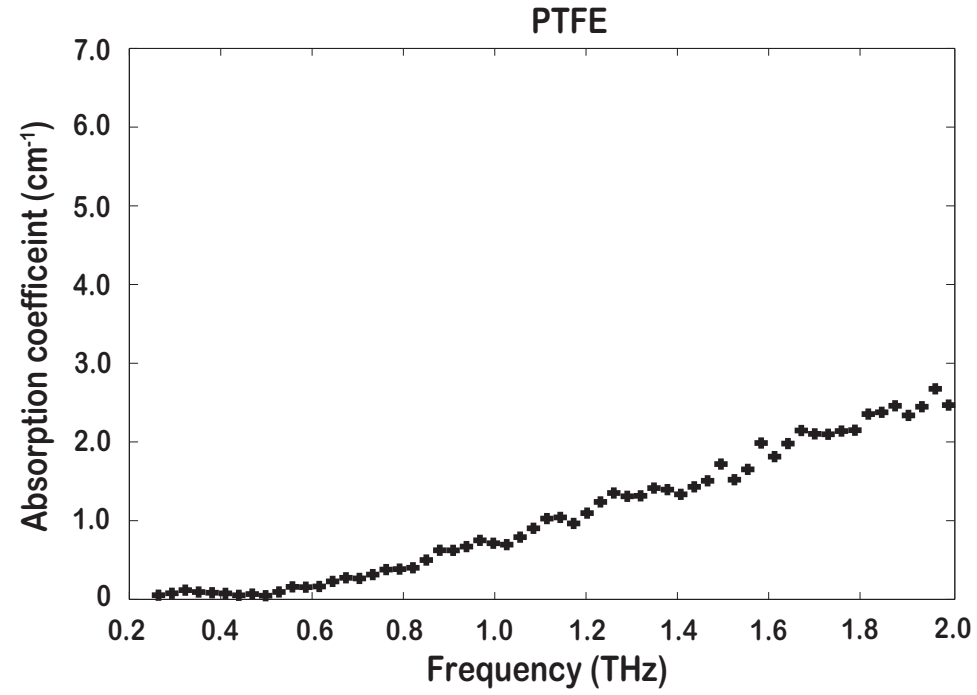

(a)

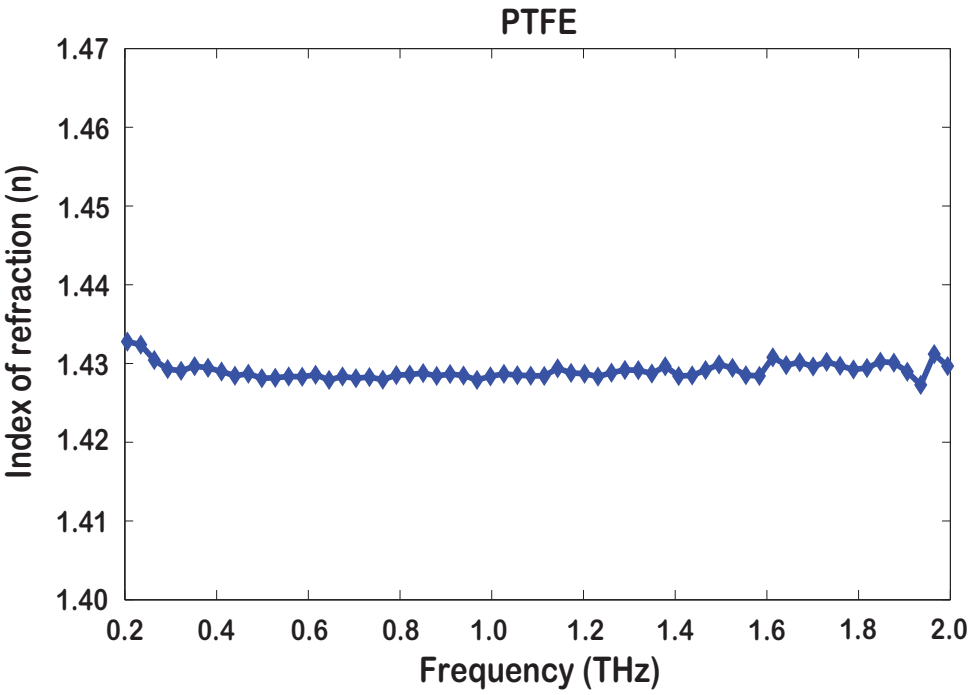

(b)

Figure 4.8. Absorption coefficient and refractive index spectra of PTFE. This figure illustrates the THz transmission properties of PTFE measured at room temperature. A continuum rise can be seen as frequency increases. This is due to the amorphous regions in the polymer.

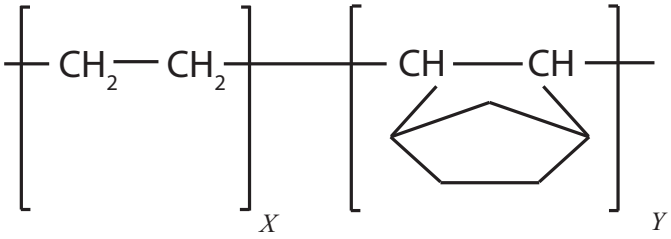

Figure 4.9. Repeating units of TOPAS™ COC copolymer. COC copolymer composed of repeated units, X of ethylene monomers and repeated units, Y of norbornene monomers. According to Khanarian and Celanese (2001), large amounts of norbornene makes the copolymer amorphous.

the refractive index is 1.52, slightly lower than COC 5013L10 (Fig. 4.11b). The refractive index obtained from terahertz spectroscopy measurements for COC 5013L10 and COC 6013S04 is close to the refractive index in the optical region provided in the manufacturer's specification. Due to its amorphous molecular structure, no absorption peaks at cooled temperatures have been reported (Fischer 2005) as compared to HDPE and PTFE. Thus, COC 5013L10 and COC 6013S04 can be highly regarded as a window material for terahertz applications.

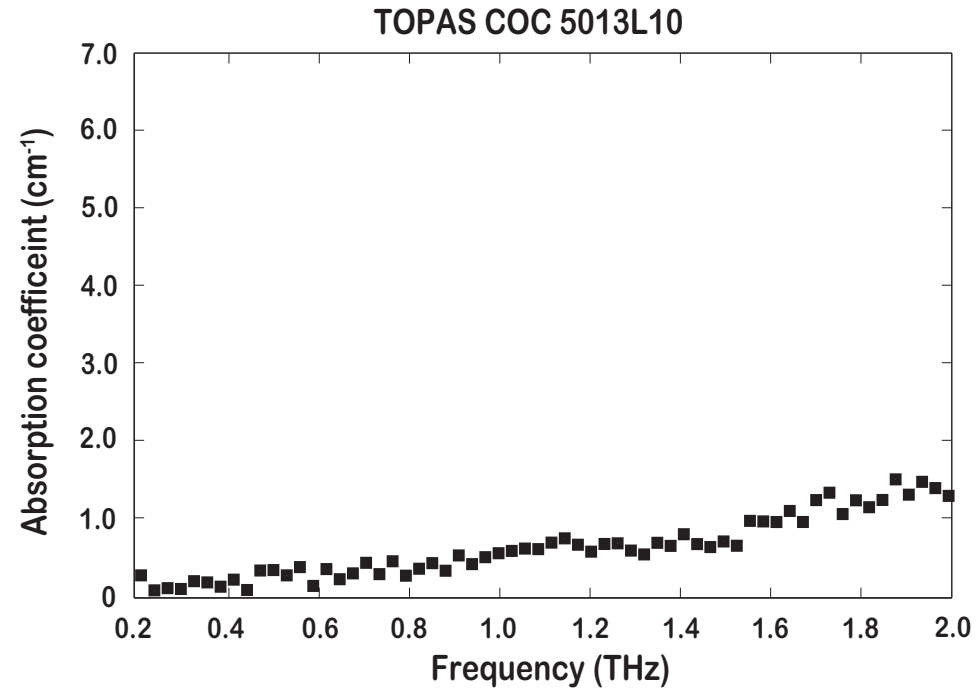

(a)

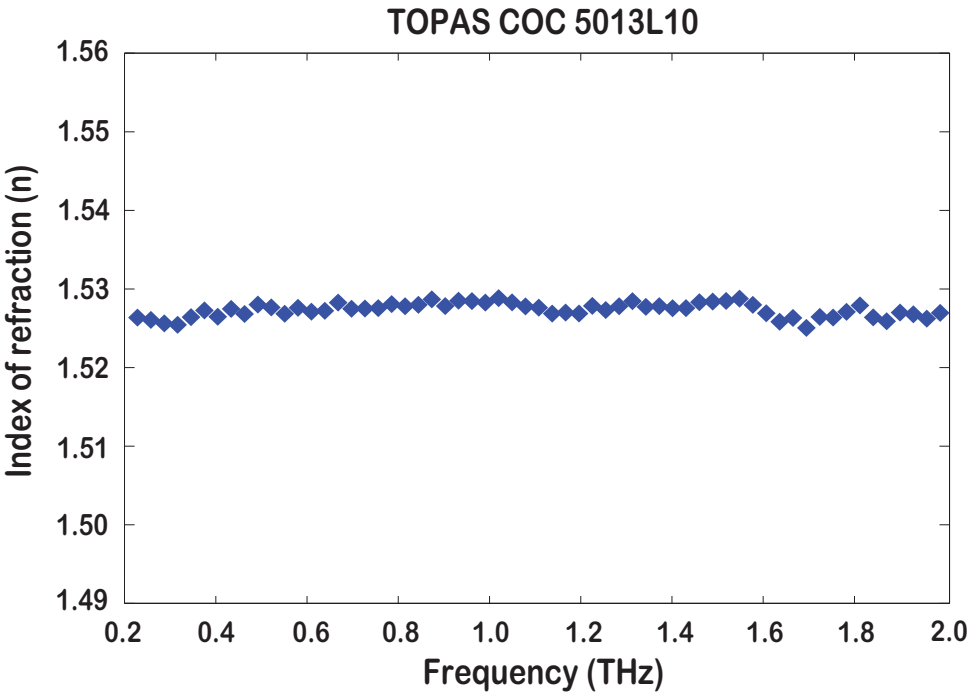

(b)

Figure 4.10. Absorption coefficient (α) and refractive index (n) of COC 5013L10. This figure depicts the terahertz transmission properties of COC 5013L10. Nearly transparent absorption and relatively low refractive index makes it ideal as a terahertz window material.

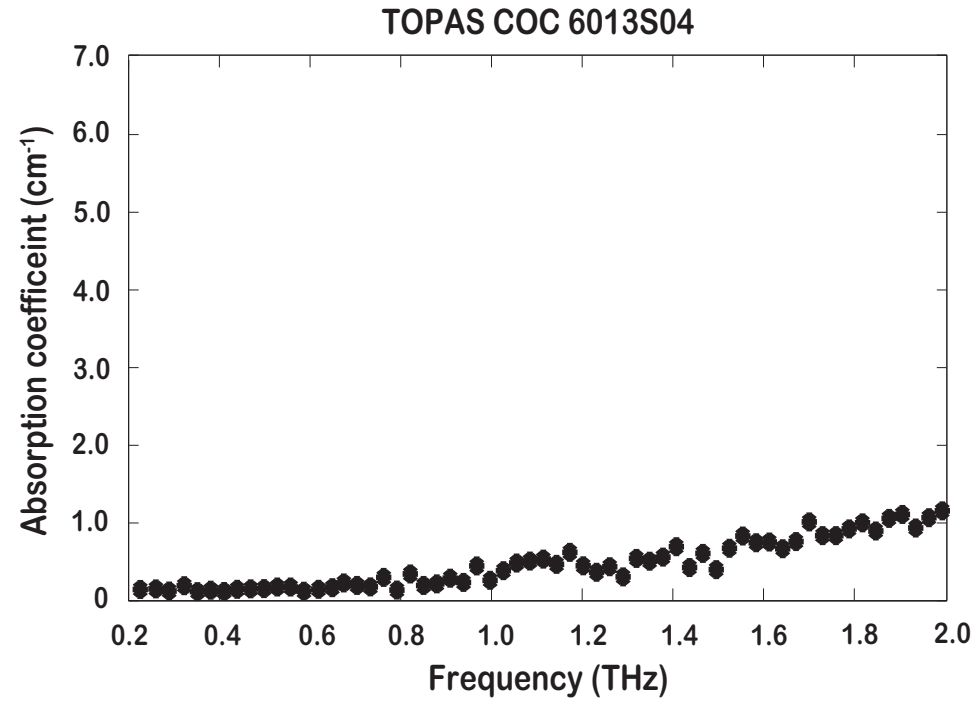

(a)

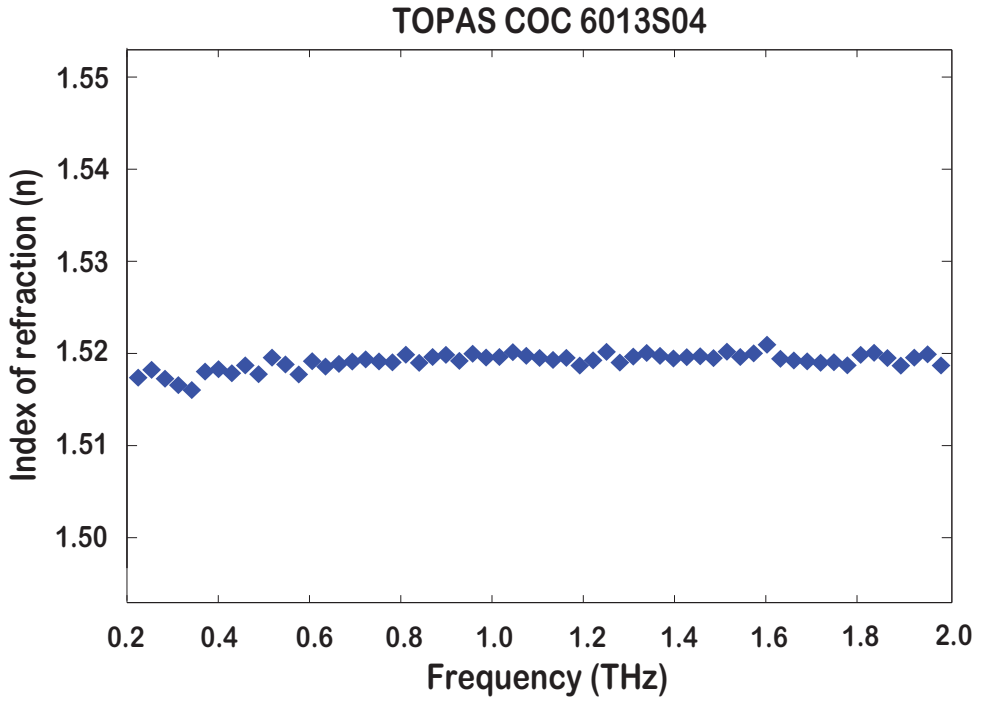

(b)

Figure 4.11. Absorption coefficient (α) and refractive index (n) of COC 6013S04. This figure illustrates the terahertz transmission properties of COC 6013S04. This copolymer has similar terahertz properties as COC 5013L10, however it is superior in its mechanical strength.

4.3.4 Poly(methyl methacrylate)–(PMMA)

Poly(methyl methacrylate) or, in short, PMMA is one of the most important polymers in current use. PMMA is also known as plexiglass or acrylic polymer. This polymer is composed of methyl methacrylate monomers (Fig. 4.12). PMMA is an amorphous polymer with methyl polar side groups. PMMA has good transmittance prop-

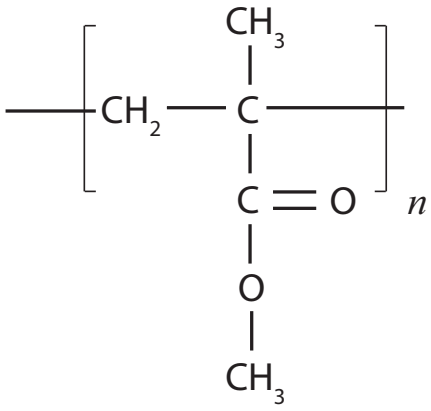

Figure 4.12. Repeating units of PMMA. This figure shows n repeated units of PMMA that is composed of methyl methacrylate monomers.

erties in the visible frequency range with high mechanical stability and is extensively used in optical applications. Here, we investigate the terahertz dielectric properties of PMMA at room temperature. It is found that PMMA is heavily absorbing in the terahertz frequency range. According to Fig. 4.13a, the absorption coefficient increases with the increase in frequency. Here, one can conclude that the increase of the absorption on PMMA is caused by its amorphous molecular structure and its methyl polar side groups. It is observed that the absorption coefficient of PMMA can be as high as 15 cm^{-1} at 1 THz. The index of refraction for PMMA is between 1.53 and 1.55. The results obtained through our measurement agree well with the literature (Piesiewicz *et al.* 2007a, Jin *et al.* 2006). Thus, we find that PMMA can be an excellent optical material in the visible frequency range but not for the terahertz region because of its high absorption coefficient.

4.3.5 Polycarbonate (PC)

Polycarbonate is a transparent amorphous polymer, which has the ability to transmit light like glass. Polycarbonate is composed of repeated units of phenyl and methyl groups on the molecular chain (Fig. 4.14). Polycarbonate has a good thermal resistance

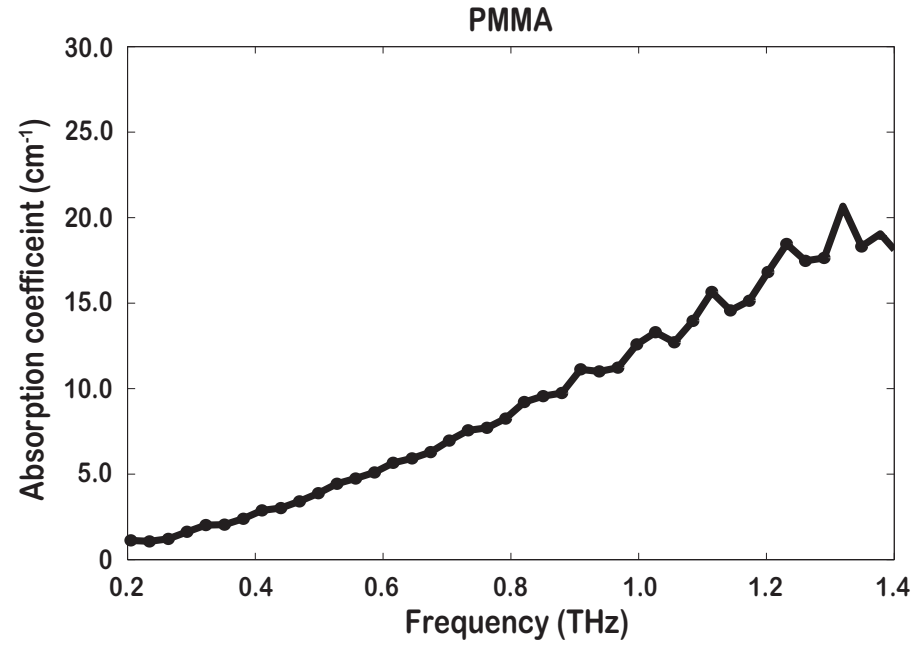

(a)

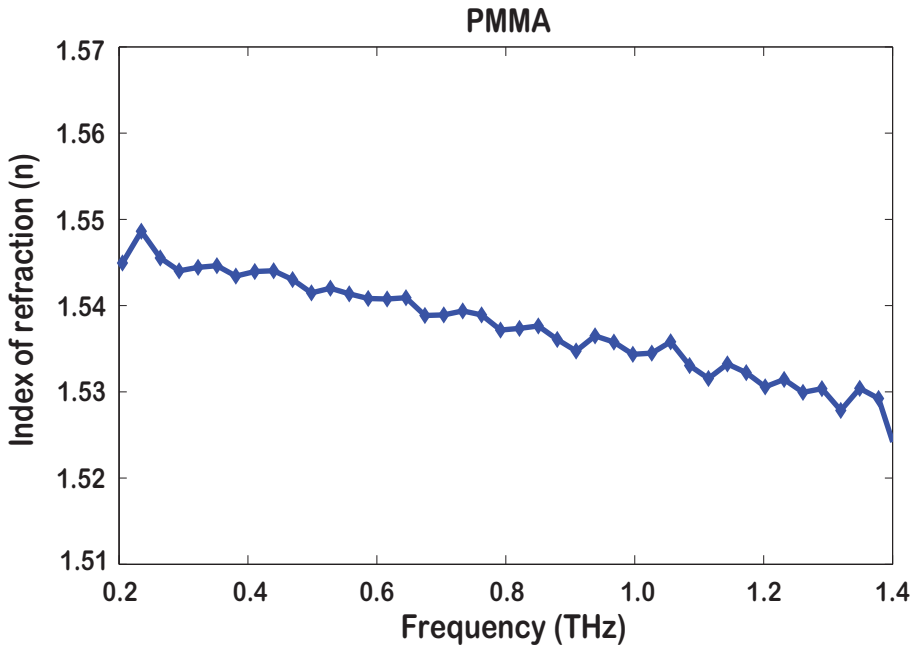

(b)

Figure 4.13. Absorption coefficient (α) and refractive index (n) of PMMA. This figure shows the terahertz transmission properties of PMMA. (a) continuous absorption as frequency increases is observed. At 1 THz, the absorption coefficient is 15 cm^{-1}, which is considered to be highly absorbing as compared to other polymers described above. The refractive index decreases as frequency increases (b).

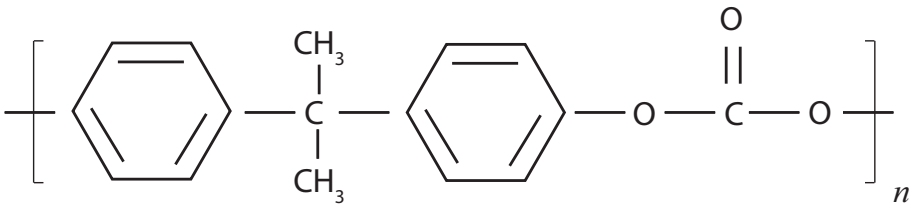

Figure 4.14. Repeating units of PC. This figure depicts a typical repeating molecular structure for PC. The molecule consists of a methyl group and a phenyl group.

but relatively high viscosity (i.e., low melt flow) during processing. The light transmittance for polycarbonate in the visible frequency range is similar to that of PMMA. Terahertz transmission spectroscopy reveals that polycarbonate can be highly absorbing. A continuum rise in the absorption coefficient caused by the amorphous region of the polymer has been observed as frequency increases. Figure 4.15 shows the terahertz dielectric properties of PC. According Fig. 4.15a, the absorption coefficient is approximately 10 cm^{-1} at 1 THz, which is considered to be highly absorbing as a window material in the terahertz bands. The refractive index of PC is approximately 1.63 at 1 THz (Fig. 4.15b). The THz transmission properties of PC reported in the literature (Jin *et al.* 2006, Piesiewicz *et al.* 2007a) matches well with our measurements. Hence, one may conclude that PC is definitely not suitable as window material for terahertz applications.

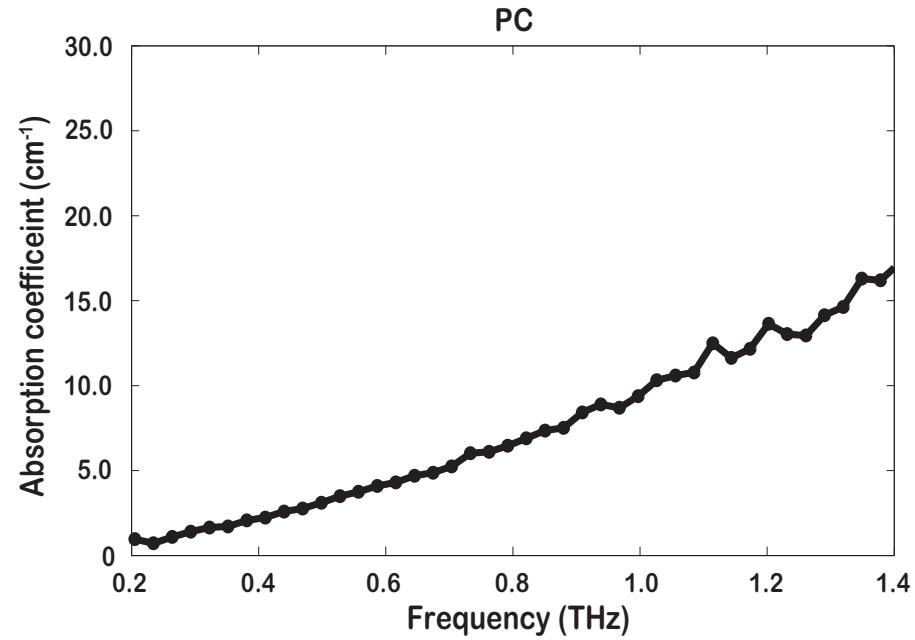

(a)

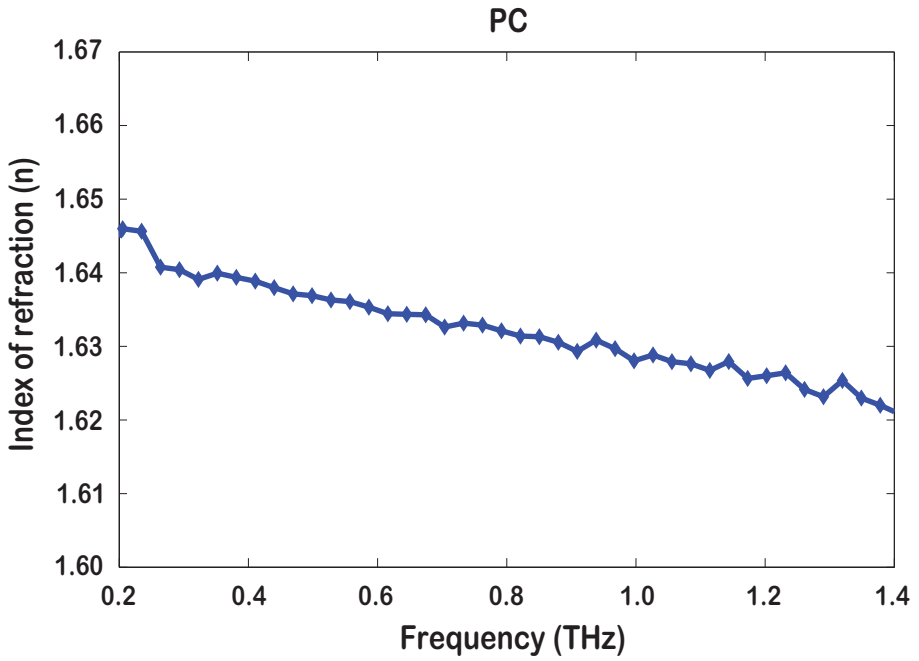

(b)

Figure 4.15. Absorption coefficient (α) and refractive index (n) of PC. This figure shows the terahertz dielectric properties of PC. (a) shows a continuum rise as frequency increases. This is strongly undesirable as a window material in terahertz region region. (b) the refractive index decreases as frequency increases.

Table 4.1. Terahertz dielectric properties of polymer materials. This table summarises the THz dielectric properties of amorphous and semicrystalline polymer materials at 1 THz.

Polymer material	α cm^{-1}	index (n)	Morphology
HDPE	<0.5	~1.54	Semicrystalline
PTFE	<1.0	~1.43	Semicrystalline
COC 5013L10	<1.0	~1.53	Amorphous
COC 6013S04	<1.0	~1.52	Amorphous
PMMA	~15.0	~1.53	Amorphous
PC	~10.0	~1.63	Amorphous

4.4 Chapter summary

This chapter describes polymer studies using a conventional terahertz time-domain spectroscopy (THz-TDS) system in the frequency range extending from 0.2 THz to 2.0 THz. All polymers described in this chapter can be catergorised into semicrystalline and amorphous morphologies. We have verified that the semicrystalline polymers, (i.e., HDPE and PTFE) can be used as a sample holder window materials at room temperature. In this chapter, we have also demonstrated that the amorphous polymers (i.e., PMMA and PC) are not suitable as a window materials due to their strong absorbing property in the terahertz band. A new class of thermoplastic, COC, appears to be the most desirable polymer as it is amorphous and has non-polar side groups. A combination of amorphous morphology and non-polar side groups results in very low absorption in the terahertz region and also has low moisture absorption (moisture absorption of COC will covered in detail in Chapter 5). A summary of terahertz dielectric properties of all the polymer materials measured in this chapter is given in Table 4.1. Based on the experimental results and Table 4.1, COC is highly recommended as a window material for transmission THz spectroscopy.

In the next chapter, we present hygroscopicity measurements using a linear absorption model on the polymer materials described in this chapter in order to verify which are suitable as window materials for THz liquid spectroscopy in terms of aqueous solutions.

Chapter 5

Sensing the hygroscopicity of polymer and copolymer materials

HYGROSCOPICITY of polymer and copolymer materials in the low terahertz frequency range using a linear absorption model is investigated to identify suitable window materials for THz spectroscopy of aqueous solutions. Here, we identify COC 6013S04 and COC 5013L10 as optimal THz window materials, possessing both low hygroscopicity and high transmission in the THz regime.

5.1 Introduction

Over the past two decades, there has been a tremendous growth in THz technology. Many potential applications including medical diagnostics (Knobloch *et al.* 2002, Png *et al.* 2008), spectroscopy of biomolecules (Fischer *et al.* 2007), security sensing (Liu *et al.* 2007, Baker *et al.* 2007, Dobroiu *et al.* 2007), and communications (Moeller *et al.* 2008, Piesiewicz *et al.* 2007b) have been explored. A number of significant studies have motivated the need for THz spectroscopy of liquids, including: characterising the hydration state in solution (Arikawa *et al.* 2008), investigating inflammable liquids (Ikeda *et al.* 2005), solvent diffusion in polymers (Obradovic *et al.* 2007), dielectric properties of oil-water complexes (Gorenflo *et al.* 2006), and solvation dynamics of liquid mixtures (Venables and Schmuttenmaer 2000a, Venables and Schmuttenmaer 2000b). Due to the fact that water significantly absorbs terahertz, i.e approximately 200 - 230 cm^{-1} at 1 THz (Kindt and Schmuttenmaer 1996), a window material that is high in transmission, and has low hygroscopicity is required for liquid spectroscopy applications. Although a number of papers on polymer window materials for THz spectroscopy have been presented (Naftaly and Miles 2007, Podzorov and Gallot 2008, Jin *et al.* 2006, Sengupta *et al.* 2006, Fischer 2005), the hygroscopicity of polymer windows that could hamper terahertz transmission has not been investigated yet. Thus, we present hygroscopicity measurements on polar and non-polar polymer materials using transmission-mode terahertz time-domain spectroscopy (THz-TDS) system. The frequency range of our results is in the 0.2 THz to 2.0 THz band.

5.1.1 Objectives and framework

This chapter is focused on hygroscopicity measurements on polar and non-polar polymer materials using a standard transmission-mode terahertz time-domain spectroscopy (THz-TDS) system. In this study, a linear absorption model has been used to determine the hygroscopic level of the polymer materials. This chapter is structured as follows: A short introduction on the polar and non-polar polymers is presented in Sec. 5.2. Also, in this section, polymer hygroscopicity will be introduced. The sample preparation technique is described in Sec. 5.3 followed by the analysis technique in Sec. 5.4. The results for several polymer materials are given and discussed in Sec. 5.5. The chapter summary and future recommendations are presented in Sec. 5.6.

5.2 Polar and non-polar polymers

It is well known for a long time that dipole forces in polar polymers are created by an imbalance in the distribution of electrons. Moreover, in the presence of an electric field the dipoles will attempt to align with the field. On the other, it has been demonstrated that non-polar polymers are truly covalent and generally have symmetrical molecules. Here, there are no dipole forces present and the application of an electric field does not force alignment of any dipoles (Housecroft and Constable 2006).

5.2.1 Polymer hygroscopicity

Hygroscopicity is the ability of a substance (e.g. a polymer) to absorb water molecules. The hygroscopicity measurement of polymer materials has been well explored using techniques such as FTIR-ATR (Sammon *et al.* 1998) and the standard ASTM D570 weight test method for water absorption of polymers (*Standard Test Method for Water Absorption of Plastics* 1986). However, a detailed investigation in the THz regime to identify optimal polymer window materials with low hygroscopicity has not yet been reported. Therefore, we investigate the hygroscopicity of polar and non-polar polymer materials using terahertz radiation. In this technique, the hygroscopicity of polymer materials is determined by observing the changes in the absorption coefficient (α) before and after hydration of the polymer materials in distilled water. We have selected several polar polymers (i.e., poly-methyl methacrylate (PMMA), polycarbonate (PC)), non-polar polymers (i.e., high density polyethylene (HDPE), poly-tetrafluoroethylene (PTFE)) and non-polar copolymers (i.e., cyclic-olefin copolymer (COC) 6013S04 and 5013L10) for this investigation.

5.3 Sample preparation

Two sets of polar and non-polar polymer materials are investigated under two conditions: (i) dehydrated in a vacuum oven and (ii) hydrated in distilled water. The temperature used in the vacuum oven to dehydrate the samples is 80°C. The lowest and the highest melting temperature T_m for all the polymer materials measured are 130°C and 330°C respectively. Thus, dehydrating the conditioned samples in the vacuum oven at 80°C is well below the melting point. Based on these conditions, the absorption coefficient of the polymer materials are measured after 24 hours and 120

hours. Five averaged scans are used to increase the signal-to-noise ratio of the measurements. Moreover, the measurements are conducted in a nitrogen purged environment to minimize the effect of water lines interfering with the results. The excess water on the surface of the sample is removed before the measurement. Also, in order to increase the accuracy of the measurements, the samples are measured immediately after conditioning. The thickness of the measured samples is approximately 3 mm. The experiments are conducted at room temperature. Figure 5.1 shows the process diagram of the experiment.

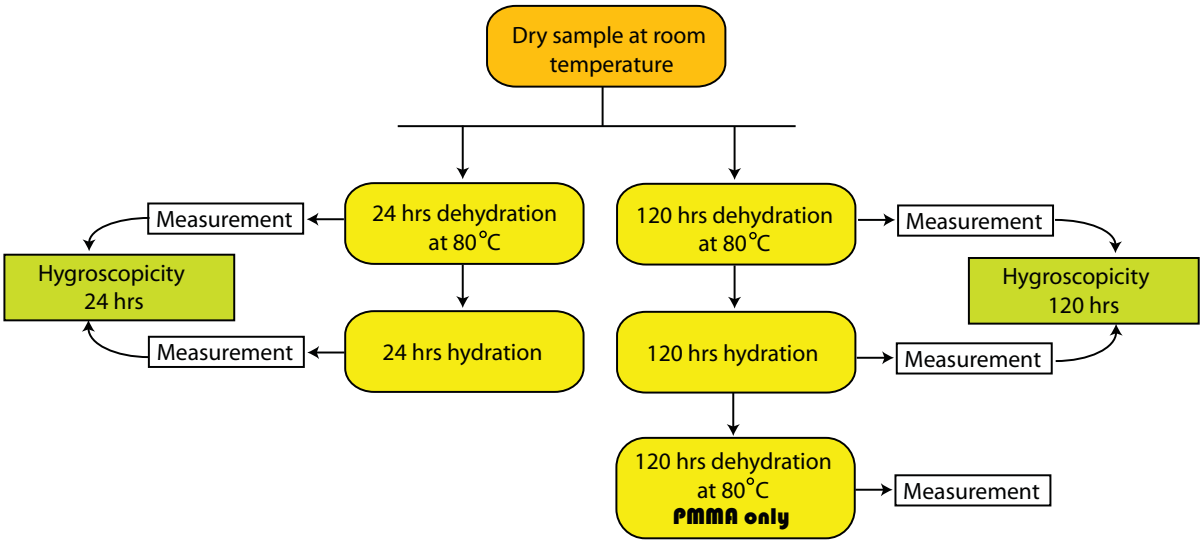

Figure 5.1. Process diagram of the experiment. This figure shows the procedures involved in determining the hygroscopicity of a polymer. Here, in order to show that the optical properties PMMA are not affected by the dehydration and hydration process, the PMMA is dehydrated again for remeasurement. The results and discussion of the measurements are given in Sec. 5.5.

5.4 Analysis

Assuming that the terahertz radiation is incident to the measured polymer material, the spectral components at angular frequency ω of the electric field of the terahertz wave transmitted through the sample and reference can be written as (refer to Sec. 3.3.1):

$$\widetilde{E}_{\text{sample}}(\omega) = T_{12}(\omega).\, P_2(\omega, d).\, T_{23}(\omega).A(\omega).\text{FP}(\omega) \tag{5.1}$$

$$\widetilde{E}_{\text{reference}}(\omega) = T_{13}(\omega).\, P_{\text{air}}(\omega, d).\, A(\omega)\,, \tag{5.2}$$

where $\widetilde{E}_{\text{sample}}(\omega)$ and $\widetilde{E}_{\text{reference}}(\omega)$ are the complex spectral components of the sample and the reference pulses respectively. Here, P_2 and P_{air} refer to the propagation coefficient of the polymer and air and T_{ab} is the transmission amplitude coefficient of a THz wave from medium a to b. Also $A(\omega)$ accounts for the amplitude of each frequency component and d is the thickness of the polymers. The Fabry-Pérot reflection, $\text{FP}(\omega)$ term is ignored for this measurement since the thickness of the samples measured is sufficiently thick to ensure that there are no multiple reflections in the recorded time window. The ratio of the transmission spectra is as follows:

$$\widetilde{T}(\omega) = \frac{\widetilde{E}_{\text{sample}}}{\widetilde{E}_{\text{reference}}} . \tag{5.3}$$

Thus, based on the ratio, the extinction coefficient (κ), and absorption coefficient (α) of the polymers can be extracted based on the following formulas:

$$\kappa(\omega) = -\frac{c_0}{\omega d}\ln\left(\frac{(1+n(\omega))^2}{4n(\omega)}p(\omega)\right) , \tag{5.4}$$

$$\alpha(\omega) = 2\frac{\kappa(\omega)\omega}{c_0} . \tag{5.5}$$

Here, $p(\omega)$ is the magnitude obtained from the ratio of the transmission spectra and $n(\omega)$ is the refractive index. The speed of light in vacuum is denoted as c_0. The hygroscopicity is determined by using the linear absorption model which can be written as follows (Gorenflo *et al.* 2006):

$$\alpha_{\text{H}}(\omega) = (1-c_{\text{x}})\alpha_{\text{DH}}(\omega) + c_{\text{x}}\alpha_{\text{w}}(\omega) \tag{5.6}$$

where $\alpha_{\text{H}}(\omega)$ is the absorption coefficient of the hydrated polymer. The $\alpha_{\text{DH}}(\omega)$ is the absorption coefficient of a dehydrated polymer (after drying at 80°C) and $\alpha_{\text{w}}(\omega)$ is the absorption coefficient of distilled water at 1 THz. Here, c_{x} denotes the water absorption, which is also known as the water concentration (Gorenflo *et al.* 2006). Rearranging the above equation gives the following formula to calculate the amount water absorbed by the samples,

$$c_{\text{x}} = 100\frac{\alpha_{\text{H}}(\omega) - \alpha_{\text{DH}}(\omega)}{\alpha_{\text{w}}(\omega) - \alpha_{\text{DH}}(\omega)} . \tag{5.7}$$

Here, c_{x} for 24 hours measurement is obtained by comparing $\alpha_{\text{H}}(\omega)$ and $\alpha_{\text{DH}}(\omega)$ of 24 hours and c_{x} for 120 hours measurement is obtained by comparing $\alpha_{\text{H}}(\omega)$ and $\alpha_{\text{DH}}(\omega)$ of 120 hours.

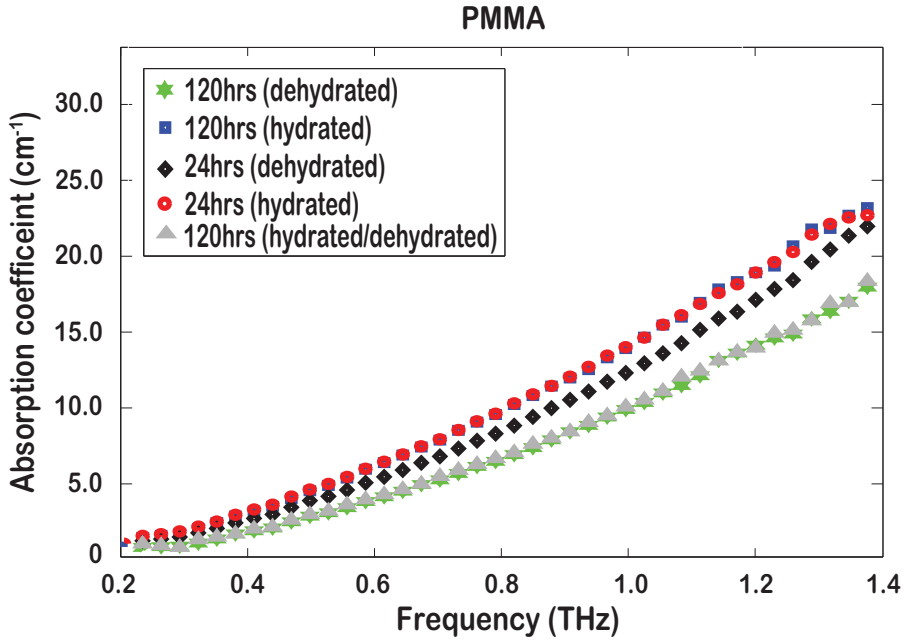

Figure 5.2. Absorption spectra of PMMA. This figure illustrates the absorption coefficient of PMMA at different hydration levels. It can be observed that there is a distinct difference between the hydrated and the dehydrated state. Also, it is noted that the hydration state of PMMA saturates after 24 hrs. The hygroscopicity measurement indicates that the PMMA absorbs 0.75 % of water after 24 hours and 1.8 % after 120 hours of hydration. The increase in absorption after the hydration for 24 hours and 120 hours is due to its methyl (CH_3) polar group, which binds strongly to water molecules.

5.5 Results and discussion

Measurements on seven different polymer materials have been conducted. The experimental results of the absorption coefficients are presented in Figs. 5.2 - 5.4. These figures illustrate the variation in the absorption coefficients between hydrated and dehydrated polymers. In these figures, the error bars have not been plotted for clarity, as they are about the same size as the symbols that represent the data points. Figure 5.2 shows the absorption coefficient of PMMA measured at different hydration levels. It is noted that as the hydration period increases, the hydration level increases. However, PMMA shows no difference in hydration level after 24 hours. This is because it has reached the saturation point. To show that the optical properties of PMMA are not affected by the hydration and dehydration process, the sample is dehydrated again for 120 hours in a vacuum oven at 80°C after the dehydration and hydration process. The results obtained show that the absorption coefficient remains unchanged compared to

the original dehydrated sample, which indicates that the optical properties of PMMA are not affected after 120 hours of the hydration and then the dehydration process.

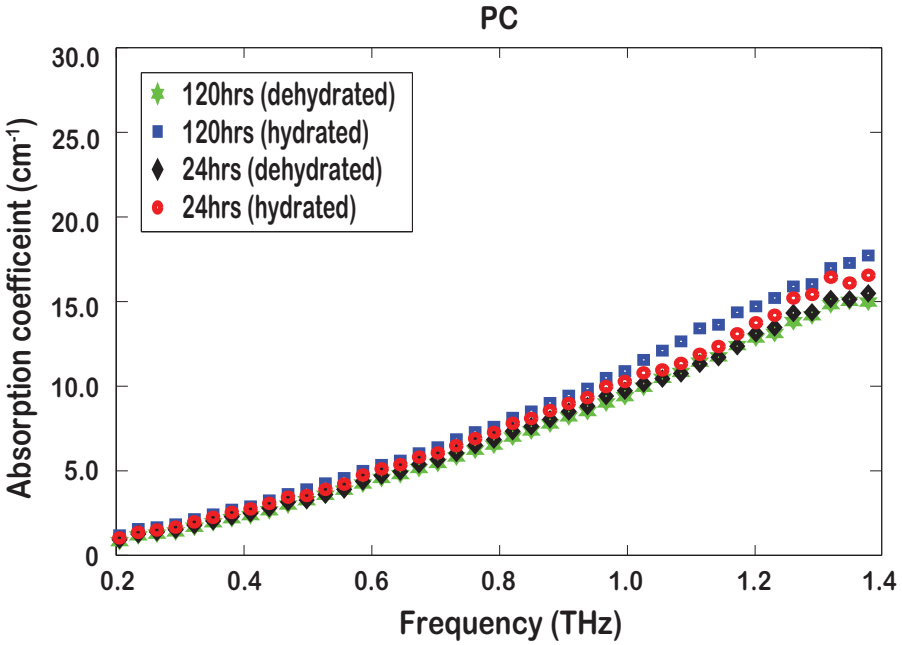

Figure 5.3. Absorption spectra of PC. This figure depicts the absorption coefficient of PC at different hydration levels.

In Fig. 5.3, the absorption spectra for polycarbonate (PC) are presented. The hydration level is proportional to the hydration period. The increase in the hydration level is due to the strong polar group (C=O), which binds strongly the water molecules. The hygroscopicity measured at 1 THz is 0.21 % for 24 hours of hydration and 0.69 % for 120 hours of hydration.

The absorption spectra for COC 6013S04 are presented in Fig. 5.4. Note that COC 6013S04 is a crystal clear non-polar polymer, which has a symmetrical molecular structure. Such a structure prevents water molecules from binding with polymer molecules. Thus, it can be seen from Fig. 5.4 that the hydration process has a lesser effect on the COC 6013S04. The hygroscopicity measured for COC 6013S04 at 1 THz is less than 0.01 % for 24 hours of hydration and 0.09 % for 120 hours of hydration. A summary on the variation of the absorption coefficient at 1 THz for all the measured polymer materials is shown in Table 5.1. Also, the hygroscopicity of the polymers obtained using Eqs. 5.6 and 5.7 is given in Table 5.1. The hygroscopicity obtained from the literature based on the American Society for Testing and Material, ASTM D570 weight test method is also included in the table to verify agreement.

Table 5.1. The variation in absorption coefficient and hygroscopicity of polymer materials. The hydration and dehydration of the polymer materials are measured at 24 hours and 120 hours. The variation of the absorption coefficient for all polymer materials is obtained at 1 THz. The hygroscopicity data obtained from Eqs. 5.6 and 5.7 are compared with the standard test method for water absorption of polymers (ASTM D570) confirming agreement. Note that there is no prior literature for 120 hours hydration.

	Absorption (cm^{-1})				Hygroscopicity (%)			
	24 hours		120 hours		This work		Literature	
Polymers	**Hydrated**	**Dehydrated**	**Hydrated**	**Dehydrated**	**24 hours**	**120 hours**	**24 hours (ASTM D570)**	**120 hours**
COC 6013S04	0.269	0.240	0.361	0.160	0.01	0.09	0.01	-
COC 5013L10	0.334	0.315	0.485	0.290	0.01	0.08	0.01	-
HDPE	0.259	0.215	-	-	0.02	-	0.01	-
PTFE	-	-	0.552	0.450	-	0.04	0.01	-
PMMA	14.020	12.393	14.015	10.000	0.75	1.80	0.5	-
PC	10.346	9.800	10.977	9.457	0.21	0.69	0.25	-

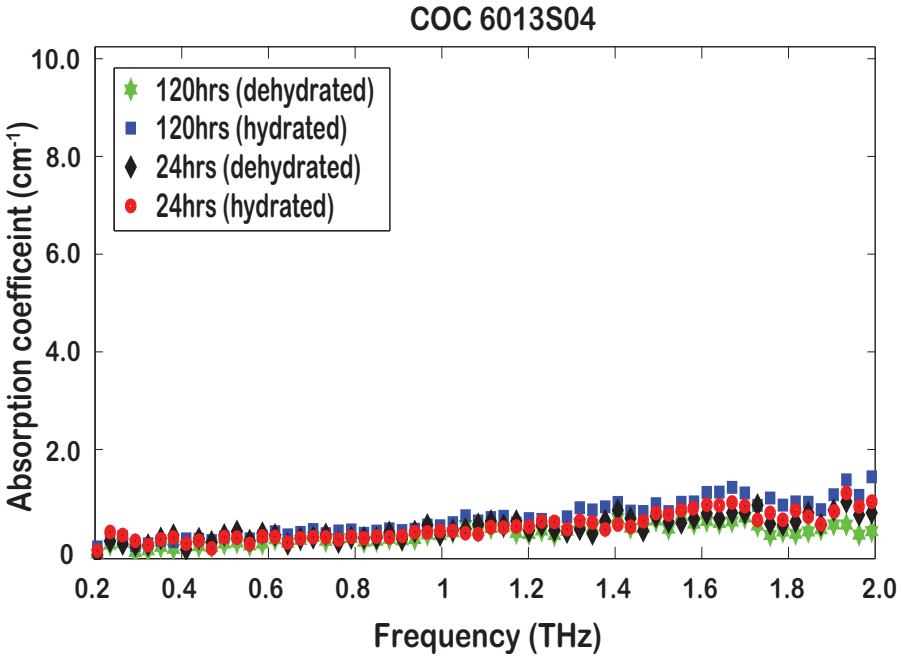

Figure 5.4. Absorption spectra of COC 6013S04. This figure compares the absorption coefficients of non-polar polymer COC 6013S04 at different hydration levels. It is clear that the effects of hydration are much less compared to PC and PMMA.

Based on Table 5.1, all non-polar polymer materials have absorption coefficients less than 1 cm^{-1} at 1 THz. This is obviously due to their covalent bonds and symmetrical molecular structures, which do not create any dipole polarization in the presence of an electric field. However, polar polymer materials exhibit strong absorption. This is mainly caused by the imbalance of electrons, which create a dipole polarization in the presence of an electric field. According to Table 5.1, the hygroscopicity measurements conducted here shows a close match to the ASTM D570 standard that is an international standard used for water absorption in polymer materials for 24 hours. However, no document has been presented by the ASTM for a water absorption for 120 hours. Thus, our measurements conducted for 120 hours are not compared with the literature. All the non-polar polymer and copolymer materials measured exhibit a very low hygroscopity for both the 24 hours and 120 hours of hydration and dehydration cycles. However, polar polymer materials such as PMMA have a very high hygroscopicity and absorption coefficient, which may not be suitable as window materials in the THz regime. Therefore, according to Table 5.1, HDPE, PTFE, COC 6013S04, and COC 5013L10 are identified as an optimal window material with low hygroscopicity and low absorption coefficient in THz regime.

5.6 Chapter summary

In this chapter, we have demonstrated the hygroscopicity of polymer and copolymer materials using the linear absorption model in the terahertz frequency band. This is achieved by observing the changes in the absorption coefficients of the measured samples before and after hydration for 24 hours and 120 hours. Good agreement in hygroscopicity is produced when compared with the ASTM D570 water absorption standard. All measured non-polar polymer and copolymer materials are potential window materials for liquid spectroscopy applications since they exhibit a low absorption coefficient and are less affected by water absorption, however, in certain liquid spectroscopy applications, PTFE and HDPE may not be suitable as window material due to their optical opaqueness. This is because the optical opaqueness of PTFE and HDPE prevents visual inspection which could hinder liquid measurements. Thus, we recommend COC 6013S04 and COC 5013L10 as optimal window materials for terahertz liquid spectroscopy applications.

T-ray spectroscopy of liquid may reveal useful information such as liquid dynamics, solvation processes, and biological systems. Over the past decade, various sample holders with various window cell geometries have been used to conduct liquid measurement in the THz regime. In this chapter, we have shown several potential window materials for THz liquid spectroscopy application. In the following chapter, various liquid cells for terahertz liquid spectroscopy using some of the potential polymer materials described in this chapter are explained.

THz-TDS sample cells for liquid spectroscopy

LIQUID spectroscopy allows an analysis of chemical composition and provides a better understanding of the solvation dynamics of various types of liquids. Significant progress in THz liquid spectroscopy in recent years has motivated the need for various window cell geometries for liquid measurements. A review on various window cell geometries used in THz liquid spectroscopy is given in this chapter. Custom-built window cells based on transmission and dual-thickness geometries using a COC 5013L10 polymer material are presented. The parameter extraction technique for each window cell geometry is elaborated.

This chapter forms a basic understanding of various window cell geometries for the development of the fixed dual-thickness window spinning wheel technique discussed in Ch. 8.

6.1 Introduction

Significant progress has been achieved over the last two decades relating to experimental and theoretical aspects of a terahertz spectroscopy of liquids. Terahertz spectroscopy has been widely used to study liquid dynamics, solvation processes, and biological systems.

Kindt and Schmuttenmaer (1996) investigated the frequency-dependent THz optical properties of polar liquids such as water, methanol, ethanol, 1-propanol and liquid ammonia. These liquids were held in a high density polyethylene (HDPE) bag sandwiched between two parallel high-resistivity silicon or high-density polyethylene windows. Thrane *et al.* (1995) reported T-ray optical properties of liquid water measured at 292 K, followed by Rønne *et al.* (1997) who have studied T-ray spectra of liquid water as a function of temperature. These measurements were performed using a window cell based on reflection geometry. It has been reported that the absorption of polar liquids is due to the interaction of polar molecules with the permanent dipole moments of the individual molecules (Pedersen and Keiding 1992). According to their work, a strong rise in absorption is due to the picosecond range of time constant of the oriented dipoles in the presence of an electric field.

On the other hand, Pedersen and Keiding (1992) reported that an absorption of non-polar liquids is due to transient dipole moments (temporary dipole moments) induced via collisions in the liquid. For this reason, non-polar liquids have absorption coefficients 100 times smaller than polar liquids (Mickan 2003). Pedersen and Keiding (1992) examined non-polar liquids such as benzene, carbon tetrachloride, and cyclohexane. In another study conducted by Yu *et al.* (2003), the dielectric relaxation properties of non-polar solvent carbon disulphide, CS_2 have been investigated and fitted with a single Debye relaxation model. An experimental investigation of the dipole correlation functions in selected liquid benzenes (C_6H_{12}, C_6H_6, C_6D_6, $C_6H_3F_3$, and C_6F_6) has been reported by Keiding (1997).

Asaki *et al.* (2002) studied the solvation dynamics of lithium salts in water, methanol, and propylene carbonate and verified the results using the Debye relaxation models. An investigation on the interaction between solute and non-polar solvents has been conducted by Oka and Tominaga (2006). According to Oka and Tominaga (2006),

the extinction coefficient of solutions with polar solutes decreases as a function of frequency whereas that of a non-polar solute increases. The solvation dynamics of $CHCl_3$ and CCl_4 have been explained by Flanders *et al.* (1996). In their work, the presence of bulk dipoles reducing mechanism, possibly due to clustering of $CHCl_3$ molecules with CCl_4 has been demonstrated. Recently, Dutta and Tominaga (2009) presented the solvation dynamics of solution acetone in cyclohexane. Here, the dynamics and the interaction are analyzed by a model analytic time correlation function (TCF) of the solute dipole moment. The solvation dynamics of highly absorbing polar liquids, water and acetonitrile (Venables and Schmuttenmaer 1998), acetone, acetonitrile, methanol, and water (Venables and Schmuttenmaer 2000a) have also been reported. In their study, molecular dynamics (MD) simulations were used to interpret the experimental spectra of the solvation dynamics.

Lately, there has been a considerable interest in both the experimental and theoretical investigations of biomolecules in aqueous solutions. Mickan *et al.* (2002a) measured the terahertz-frequency response of nano-sized particles of protein in organic solvents. In their work, a real-time, non-invasive and label-free method of monitoring chemical interactions has been demonstrated. They have shown that the addition of Subtilisin Carlsberg (SC) protein to a mixture of dioxane and water lowers the dielectric constant of the mixture. Also, Globus *et al.* (2006) measured T-ray spectra of DNA in liquid phase (gel). In their study, they have demonstrated reproducible spectra that show multiple resonances. These resonances are produced by the low frequency vibrational modes within the biological macromolecules in solutions. Zhang and Durbin (2006) conducted a study on myoglobin (Mb)–water mixtures at various concentrations. They reported a molar absorptivity of Mb as a function of water content. Moreover, terahertz spectroscopy has been widely used as a nondestructive and contactless technique for measuring inflammable liquids in beverage plastic bottles (Ikeda *et al.* 2005). In the work presented by Ikeda *et al.* (2005), measurements on inflammable liquids such as gasoline, gas oil, kerosene, benzine, and toluene through PE and PET beverage plastic bottles have been demonstrated. In another study conducted by Jepsen *et al.* (2008), the alcohol content of an aqueous solution in a bottle has been characterised.

Therefore, it has been proven that T-ray spectroscopy of liquids may reveal useful information such as liquid dynamics, solvation processes, and biological systems despite the fact that terahertz radiation is heavily absorbed by liquid water. Significant

progress in THz liquid spectroscopy in the recent years has motivated the need for various window cell geometries for liquid measurement.

6.1.1 Objectives and framework

According to the literature, various window cell geometries to perform a THz liquid spectroscopy have been presented. In this chapter, we will concentrate on describing several window cell geometries that include a single-thickness window cell geometry, an air tight window cell geometry, a dual-thickness window cell geometry, and a reflection window cell geometry. This chapter is structured as follows: In Sec. 6.2, an introduction on each is given along with data analysis techniques are presented in this section. For each geometry, existing liquid cells used in the literature are presented.

6.2 Window cell geometries

In this section, various window cell geometries used in the transmission and reflection modes for a THz liquid spectroscopy are discussed. An understanding of these cells are crucial for the development of the fixed dual-thickness window cell which will be described in Ch. 8.

6.2.1 Single-thickness window cell geometry

A typical single-thickness window cell geometry used for liquid spectroscopy is illustrated in Fig. 6.1. This geometry consists of a spacer located in between two homogeneous parallel plates. Figure 6.1a shows a window cell set up with an air gap for reference measurements. Here, a spacer with a thickness, d_{liquid}, is inserted in between the parallel plates. The thickness of the parallel plates is denoted as d_{mat}. T-rays are illuminated through the window cells to produce $E_{\text{reference}}$. As for sample measurements, the air gap with thickness, d_{liquid}, is filled with liquid. Illumination by T-rays through this window cell set up produces E_{sample} (Fig. 6.1b). The experimentally measured spectral components of the reference and sample signal can be modelled by (refer to Sec. 3.3.1)

$$\begin{aligned}\widetilde{E}_{\text{reference}}(\omega) = T_{12}(\omega) \cdot P_2(\omega, d_{\text{mat}}) \cdot T_{23_{\text{air}}}(\omega) \cdot P_{3_{\text{air}}}(\omega, d_{\text{liquid}}) \cdot T_{3_{\text{air}}4}(\omega) \\ \cdot P_4(\omega, d_{\text{mat}}) \cdot T_{45}(\omega) \cdot A(\omega)\end{aligned} \tag{6.1}$$

$$\widetilde{E}_{\text{sample}}(\omega) = T_{12}(\omega) \cdot P_2(\omega, d_{\text{mat}}) \cdot T_{23_{\text{liquid}}}(\omega) \cdot P_{3_{\text{liquid}}}(\omega, d_{\text{liquid}}) \cdot T_{3_{\text{liquid}}4}(\omega) \cdot P_4(\omega, d_{\text{mat}}) \cdot T_{45}(\omega) \cdot A(\omega) \cdot \text{FP}(\omega) \tag{6.2}$$

where T_{ab} is the transmission amplitude coefficient from interface a to interface b and $P_a(\omega,d)$ is the propagation coefficient in medium a over thickness d. Also, $A(\omega)$ accounts for the amplitude of each frequency component. Taking the ratio of Eqs. 6.1 and 6.2 gives the complex transmission coefficient as described in Sec. 3.31,

$$\widetilde{T}(\omega) = \frac{\widetilde{E}_{\text{sample}}(\omega)}{\widetilde{E}_{\text{reference}}(\omega)} = \rho e^{-j\phi} \, . \tag{6.3}$$

Here, ρ is denoted as the magnitude and phase, ϕ of the complex transmission coefficient, $\widetilde{T}(\omega)$. By substituting Eqs. 6.1 and 6.2 into Eq. 6.3, one can rewrite Eq. 6.3 as follows:

$$\widetilde{T}(\omega) = \frac{T_{23_{\text{liquid}}}(\omega) \cdot P_{3_{\text{liquid}}}(\omega, d_{\text{liquid}}) \cdot T_{3_{\text{liquid}}4}(\omega)}{T_{23_{\text{air}}}(\omega) \cdot P_{3_{\text{air}}}(\omega, d_{\text{liquid}}) \cdot T_{3_{\text{air}}4}(\omega)} \cdot \text{FP}(\omega) \, . \tag{6.4}$$

The $\text{FP}(\omega)$ accounts for multiple reflections or Fabry-Pérot reflection. Here, in order to avoid complications from the $\text{FP}(\omega)$, it is assumed that the window cell and liquid sample under investigation are sufficiently thick so that $\text{FP}(\omega) = 1$. Thus, Eq. 6.4 can be simplified and expressed as

$$\widetilde{T}(\omega) = \frac{\tilde{n}_{3_{\text{liquid}}}(\tilde{n}_2 + 1)^2}{(\tilde{n}_2 + \tilde{n}_{3_{\text{liquid}}})^2} \exp\left(\frac{-j\omega d_{\text{liquid}}}{c}(\tilde{n}_{3_{\text{liquid}}} - 1)\right) , \tag{6.5}$$

where the complex refractive index of the window cell is $\tilde{n}_2 = \tilde{n}_4$. The refractive index of air is denoted as $\tilde{n}_1 = \tilde{n}_5 = \tilde{n}_{\text{air}} = 1$. Here, $\tilde{n}_{3_{\text{liquid}}}$ is the complex refractive index of the liquid. With the above assumption, the analytic expression for the THz material parameters can be found with some approximation given in Duvillaret *et al.* (1999). Substituting the complex refractive index, $\tilde{n}_{3_{\text{liquid}}} = n_{3_{\text{liquid}}} - j\kappa_{3_{\text{liquid}}}$ into Eq. 6.5 reveals the frequency dependent phase information,

$$\phi(\omega) = \frac{\omega d_{\text{liquid}}}{c}(n_{3_{\text{liquid}}}(\omega) - 1) \, , \tag{6.6}$$

and the frequency dependent magnitude

$$\rho(\omega) = \frac{n_{3_{\text{liquid}}}(\omega)(n_2+1)^2}{(n_2+n_{3_{\text{liquid}}}(\omega))^2}\exp(-\frac{\omega d_{\text{liquid}}}{c}\kappa_{3_{\text{liquid}}}(\omega)) \,. \tag{6.7}$$

Rearranging Eq. 6.6 produces frequency dependent refractive index,

$$n_{3_{\text{liquid}}}(\omega) = \frac{\phi(\omega)c}{\omega d_{\text{liquid}}} + 1 \,, \tag{6.8}$$

The frequency dependent extinction coefficient can be obtained by rearranging Eq. 6.7. Thus, the extinction coefficient can be expressed as

$$\kappa_{3_{\text{liquid}}}(\omega) = -\frac{c}{\omega d_{\text{liquid}}}\ln[\rho((\omega))\frac{(n_2+n_{3_{\text{liquid}}}(\omega))^2}{n_{3_{\text{liquid}}}(\omega)(n_2+1)^2}] \,. \tag{6.9}$$

The frequency dependent absorption coeffient can be written as follows:

$$\alpha_{\text{liquid}}(\omega) = 2\frac{\kappa_{3_{\text{liquid}}}(\omega)\omega}{c} \,. \tag{6.10}$$

One may rewrite Eq. 6.10 as follows:

$$\alpha_{\text{liquid}}(\omega) = -\frac{2}{d_{\text{liquid}}}\ln[\rho(\omega)\frac{(n_2+n_{3_{\text{liquid}}}(\omega))^2}{n_{3_{\text{liquid}}}(\omega)(n_2+1)^2}] \,. \tag{6.11}$$

Various liquid cells based on a single-thickness window cell geometry that are used for terahertz liquid spectroscopy are presented. Figure 6.2 shows a typical stainless steel Bruker's liquid cell (http://www.bruker.com.au) that is commonly used for measuring THz dielectric properties of liquids. The liquid cell has two liquid inlets; one for liquid insert and the other one to release excess water. The window material used is made of HDPE that is almost transparent to terahertz at room temperature (details on HDPE in Chapter 4 and 5). A spacer is required in order to introduce a liquid thickness of d_{liquid}. This spacer is sandwiched between the two parallel HDPE plates. Moreover, the liquid cell holder is made of stainless steel to reduce a contamination.

Figure 6.3 depicts a liquid cell made by Starna (http://www.starna.com.au). The functionality of this liquid cell is similar to the Bruker's liquid cell, however, this liquid cell has a fixed thickness, which means that one may not be able to change the thickness of the sample under test. The window material used in this liquid cell is quartz that

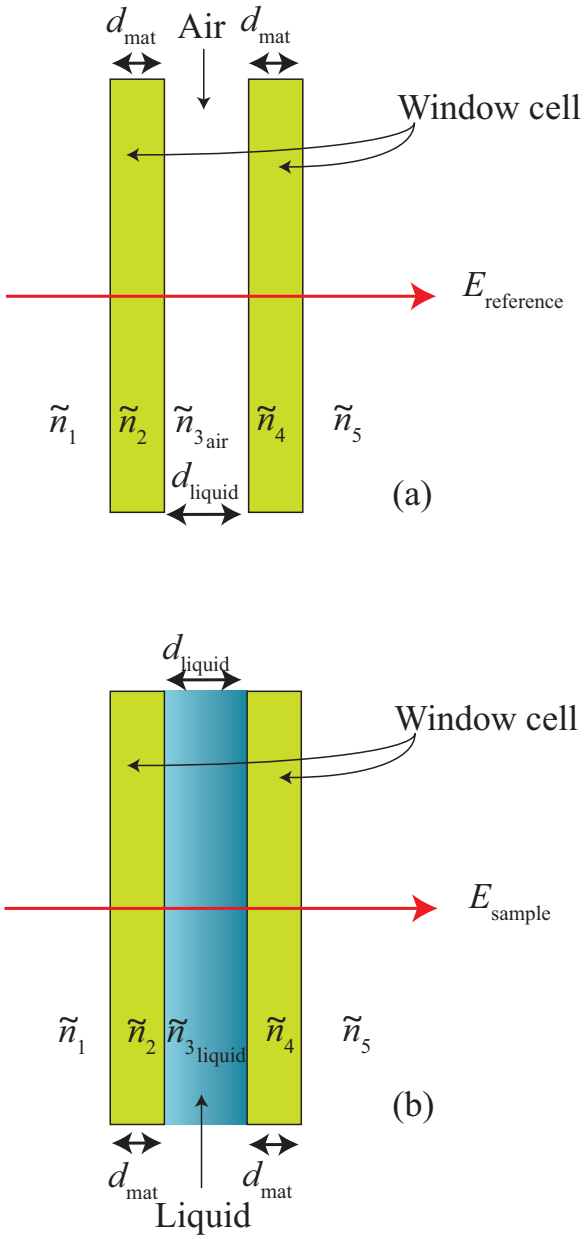

Figure 6.1. Transmission notation for a single-thickness window cell geometry. This schematic illustrates the notation for specifying T-ray propagation through liquid sample, inserted in polymer window cell. In Fig. 6.1a, window cell is prepared with a thickness gap of d_{liquid}, with no liquid is inserted. Here, $\tilde{n}_1$, $\tilde{n}_{3_{\text{air}}}$, and $\tilde{n}_5$ are the complex refractive index of air that is equal to one and $\tilde{n}_2$ and $\tilde{n}_4$ are the refractive index of the window cell. Placing the prepared window cell in the T-ray beam path produces a reference signal, $E_{\text{reference}}$. In Fig. 6.1b, liquid sample with complex refractive index $n_{3_{\text{liquid}}}$ is inserted in polymer window cell with a thickness gap of d_{liquid}. Here, the window cell is now used for sample measurements. Therefore, placing the window cell in the T-ray beam path produces a sample signal, E_{sample}.

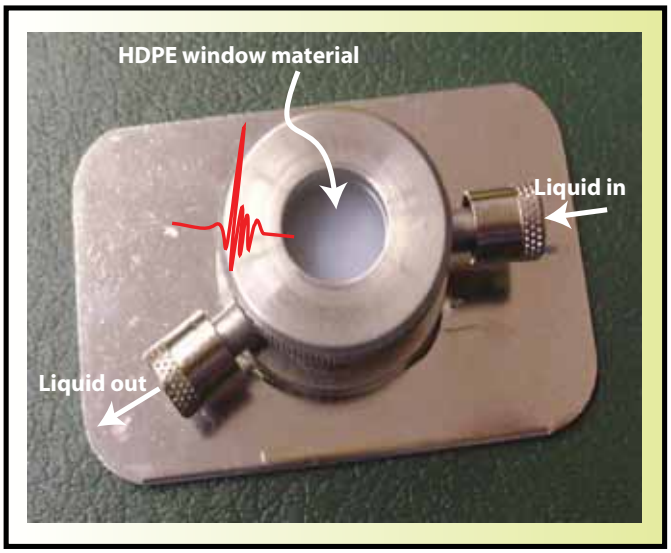

Figure 6.2. Bruker's liquid cell. This figure depicts a standard Bruker's liquid cell used for terahertz liquid measurements. The liquid is injected through one end of the liquid inlet and the excess is removed through the other end of of the inlet.

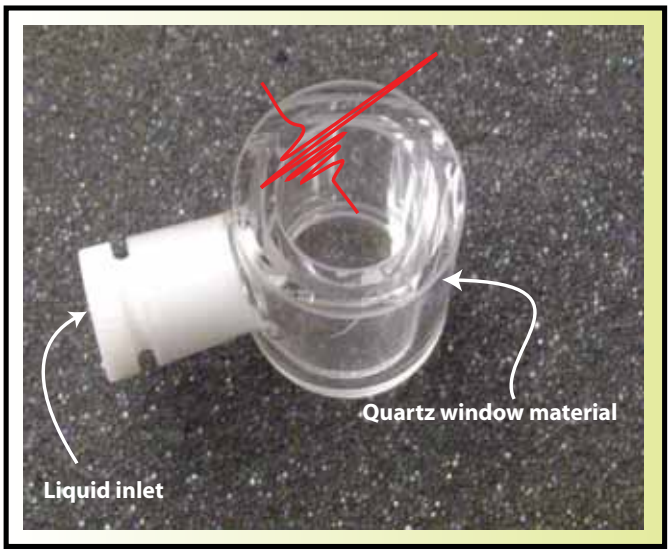

Figure 6.3. Starna's fixed thickness cylinderical liquid cell. This picture shows a cylindrical liquid cell made by Starna. The liquid is inserted through the Teflon cell top.

is low in transmission as compared to HDPE. However, optical transparency of quartz allows visual inspection, whereas HDPE is visually opaque due to its blurry colour.

Figure 6.4 depicts a custom-built liquid cell using TOPAS^{TM} COC 5013L10 as a window material. This material is low in hygroscopicity and has excellent THz transmission properties that is ideal as a window material for THz application. The liquid cell requires a spacer for introducing the liquid thickness, d_{liquid}. Height-adjustable feature has been included in this design. Moreover, the window cell has a diameter of 50 mm to eliminate signal diffractions.

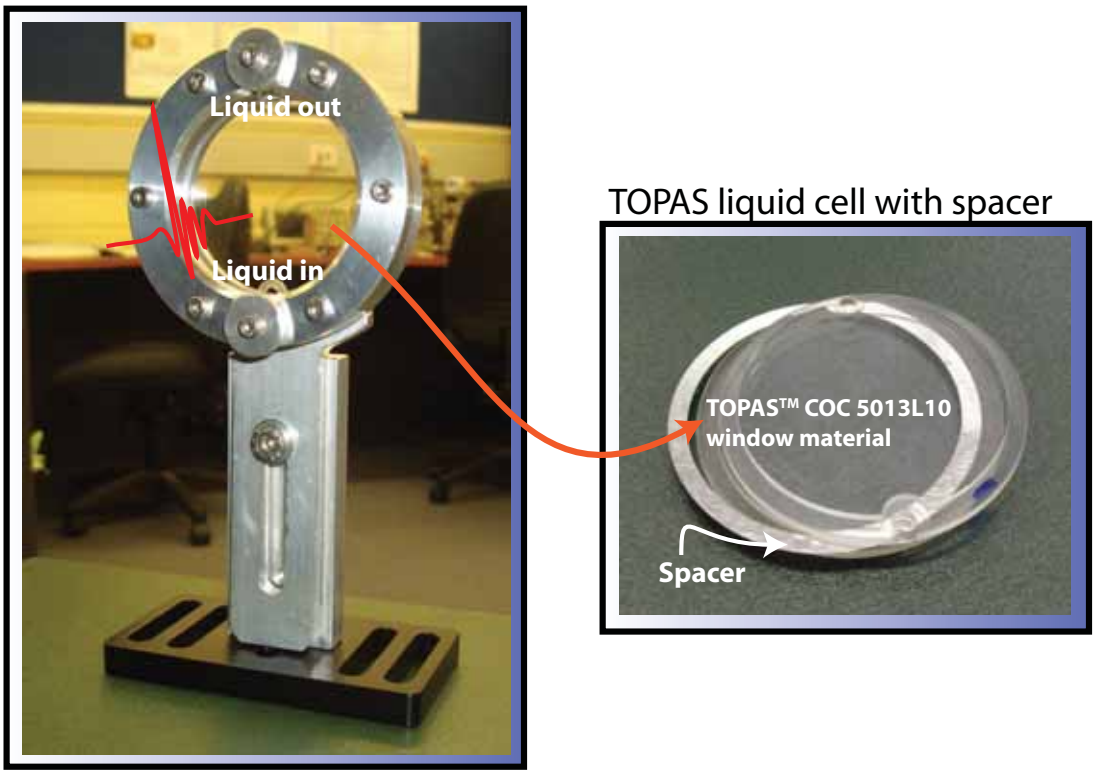

Figure 6.4. Custom-built variable thickness liquid cell. This figure shows our custom-built variable thickness window cell using TOPAS^{TM} COC 5013L10 as a window material. This window cell has two liquid inlets; one for liquid entry and one for removing excess liquid. The prepared window cell is then placed in the terahertz beam path at an appropriate height for liquid measurements.

Figure 6.5 shows another custom-built liquid cell using TOPAS^{TM} COC 5013L10 as a window material. This liquid cell allows one time sample preparation for measurements of reference and sample signals as compared to previously disccused liquid cells which requires separate sample preparation for each measurement.

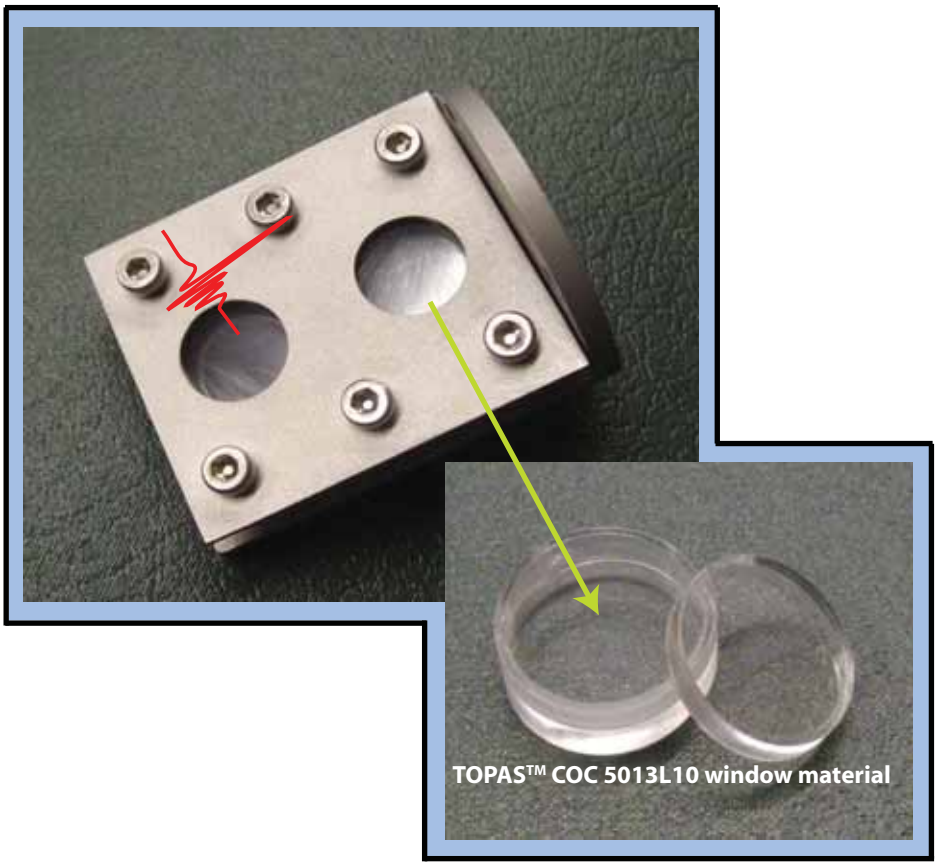

Figure 6.5. Custom-built fixed thickness liquid cell. This figure illustrates our custom-built fixed thickness liquid cell using TOPAS^{TM} COC 5013L 10 as a window material. This window cell is design with two windows; one for reference measurement and one for sample measurement.

6.2.2 Air tight window cell geometry

An alternative window cell geometry is shown in Fig. 6.6. Here, two homogeneous parallel plates similar to Fig. 6.1a are used. However, in this geometry, the plates are attached without any air gaps in between (Fig. 6.6a). The complex refractive index of the window cell is denoted as $\tilde{n}_2$ and $\tilde{n}_3$ and the complex refractive index of air is labelled as $\tilde{n}_1$, $\tilde{n}_4$, and $\tilde{n}_5$. Therefore, shining T-rays onto the window cell setup described in Fig. 6.6a produces $E_{\text{reference}}$. As for the sample measurement, an exact sample preparation described in Fig. 6.1b with liquid thickness, d_{liquid}, is required to obtain the E_{sample}. The spectral components of the reference and sample signal can be modelled by

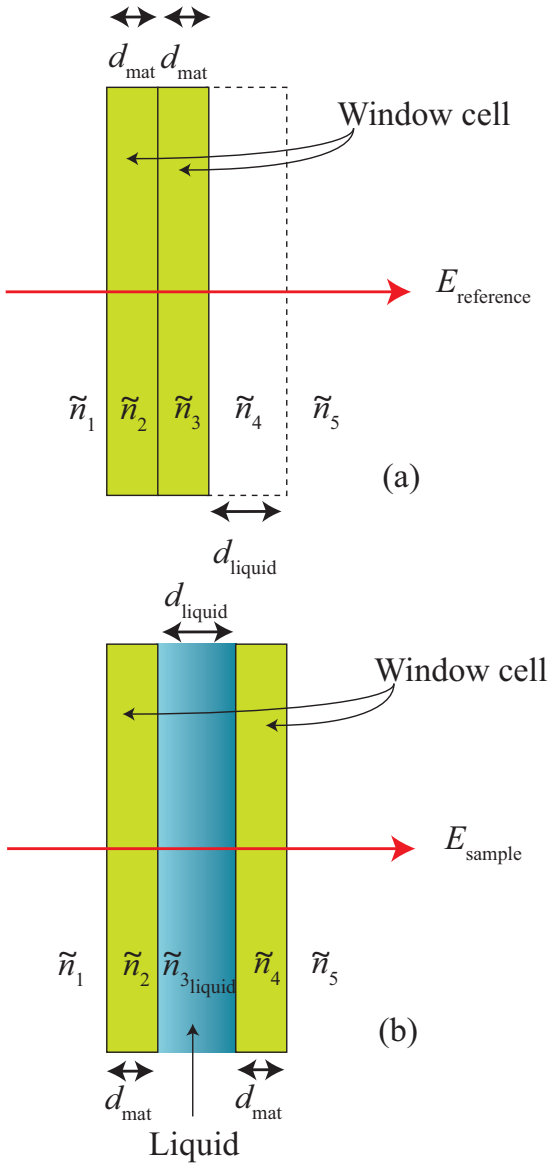

Figure 6.6. Transmission notation for air tight window cell geometry. This figure shows the notation for specifying T-ray propagation through liquid sample inserted in polymer window cells with and without the gap, d_{liquid}, being introduced. In Fig. 6.6a, the two homogeneous plates are pressed together with no air gap in between. Here, $\tilde{n}_1$, $\tilde{n}_4$, and $\tilde{n}_5$ are the complex refractive index of air that is equal to one and $\tilde{n}_2$ and $\tilde{n}_3$ are the refractive index of the window cell. Thus, placing the window cell in the T-ray beam path produces a reference signal, $E_{\text{reference}}$. In Fig. 6.6b, liquid sample with complex refractive index $n_{3_{\text{liquid}}}$ is inserted in polymer window cell with a thickness gap of d_{liquid}. Here, $\tilde{n}_1$ and $\tilde{n}_5$ are the complex refractive index of air that is equal to one and $\tilde{n}_2$ and $\tilde{n}_4$ are the refractive index of the window cell. Therefore, placing the window cell in the T-ray beam path produces a sample signal, E_{sample}.

$$\widetilde{E}_{\text{reference}}(\omega) = T_{12}(\omega) \cdot P_2(\omega, d_{\text{mat}}) \cdot T_{23}(\omega) \cdot P_3(\omega, d_{\text{mat}}) \cdot T_{34}(\omega) \cdot P_4(\omega, d_{\text{liquid}}) \cdot T_{45}(\omega) \cdot A(\omega) \,, \tag{6.12}$$

$$\widetilde{E}_{\text{sample}}(\omega) = T_{12}(\omega) \cdot P_2(\omega, d_{\text{mat}}) \cdot T_{23_{\text{liquid}}}(\omega) \cdot P_{3_{\text{liquid}}}(\omega, d_{\text{liquid}}) \cdot T_{3_{\text{liquid}}4}(\omega) \cdot P_4(\omega, d_{\text{mat}}) \cdot T_{45}(\omega) \cdot A(\omega) \cdot \text{FP}(\omega) \,. \tag{6.13}$$

Thus, based on the ratio formula described in Sec. 3.3.1, the complex transmission coefficient can be expressed as follows:

$$\widetilde{T}(\omega) = \frac{T_{23}(\omega).\, P_{3_{\text{liquid}}}(\omega, d_{\text{liquid}}).\, T_{34}(\omega)}{P_4(\omega, d_{\text{liquid}})}.\, \text{FP}(\omega) \,. \tag{6.14}$$

With the assumption that the sample measured is sufficiently thick, one may ignore the Fabry-Pérot reflection term, $\text{FP}(\omega)$. Rearranging Eq. 6.15 produces

$$\widetilde{T}(\omega) = \frac{4\tilde{n}_2\tilde{n}_{3_{\text{liquid}}}}{(\tilde{n}_2 + \tilde{n}_{3_{\text{liquid}}})^2} \exp\left(\frac{-j\omega d_{\text{liquid}}}{c}(\tilde{n}_{3_{\text{liquid}}} - 1)\right) . \tag{6.15}$$

Here, with $\text{FP}(\omega) = 1$, an analytical expression for obtaining the THz material properties can be estimated (Duvillaret *et al.* 1999). With $\tilde{n}_{3_{\text{liquid}}} = n_{3_{\text{liquid}}} - j\kappa_{3_{\text{liquid}}}$, one could extract the frequency dependent phase information as

$$\phi(\omega) = \frac{\omega d_{\text{liquid}}}{c}(n_{3_{\text{liquid}}}(\omega) - 1) \,, \tag{6.16}$$

and the frequency dependent magnitude as

$$\rho(\omega) = \frac{4n_2 n_{3_{\text{liquid}}}}{(n_2 + n_{3_{\text{liquid}}})^2} \exp\left(-\frac{\omega d_{\text{liquid}}}{c}\kappa_{3_{\text{liquid}}}\right) . \tag{6.17}$$

By rearranging Eqs. 6.17 and 6.18, the frequency dependent refractive index and extinction coefficient are expressed as follows:

$$n_{3_{\text{liquid}}}(\omega) = \frac{\phi(\omega)c}{\omega d_{\text{liquid}}} + 1 \,, \tag{6.18}$$

$$\kappa_{3_{\text{liquid}}}(\omega) = -\frac{c}{\omega d_{\text{liquid}}} \ln[\rho \frac{(n_2 + n_{3_{\text{liquid}}})^2}{4 n_2 n_{3_{\text{liquid}}}}] \,, \tag{6.19}$$

Thus, by using Eq. 6.10, the frequency dependent absorption coefficent can be written as

$$\alpha(\omega) = -\frac{2}{d_{\text{liquid}}} \ln[\rho \frac{(n_2 + n_{3_{\text{liquid}}})^2}{4 n_2 n_{3_{\text{liquid}}}}] \,. \tag{6.20}$$

The window cell geometry presented here can be implemented by using the thickness-adjustable liquid cells presented in Fig. 6.2 and Fig. 6.4. Here, one may need to remove the spacer and press the homogeneous plates together for a reference measurement. The settings for sample measurement, however, remains the same as single-thickness window cell geometry.

6.2.3 Dual-thickness window cell geometry

Terahertz liquid spectroscopy has also been presented using dual-thickness window cell geometry. In this geometry, a slight difference in the method of signal extraction have been introduced. The dual-thickness geometry is composed of two thicknesses of the same liquid, as shown in Fig. 6.7. Here, the liquid thickness for the reference measurement is less than the liquid thickness for a sample measurement. Moreover, in dual-thickness geometry, both reference and sample signals pass through the same interfaces which greatly simplifies the modelling of T-ray propagation. With the assumption that the dual-thickness window cell geometry is sufficiently thick, the spectral components of the reference and sample signals can be modelled by

$$\widetilde{E}_{\text{sample}}(\omega) = T_{12}(\omega) \cdot P_2(\omega, d) \cdot T_{23_{\text{liquid}}}(\omega) \cdot P_{3_{\text{liquid}}}(\omega, d_{\text{thick}}) \cdot T_{3_{\text{liquid}}4}(\omega) \cdot P_4(\omega, d) \cdot T_{45}(\omega) \cdot A(\omega) \tag{6.21}$$

$$\widetilde{E}_{\text{reference}}(\omega) = T_{12}(\omega) \cdot P_2(\omega, d) \cdot T_{23_{\text{liquid}}}(\omega) \cdot P_{3_{\text{liquid}}}(\omega, d_{\text{thin}}) \cdot T_{3_{\text{liquid}}4}(\omega) \cdot P_4(\omega, d) \cdot T_{45}(\omega) \cdot P_5(\omega, d_{\text{diff}}) A(\omega) \tag{6.22}$$

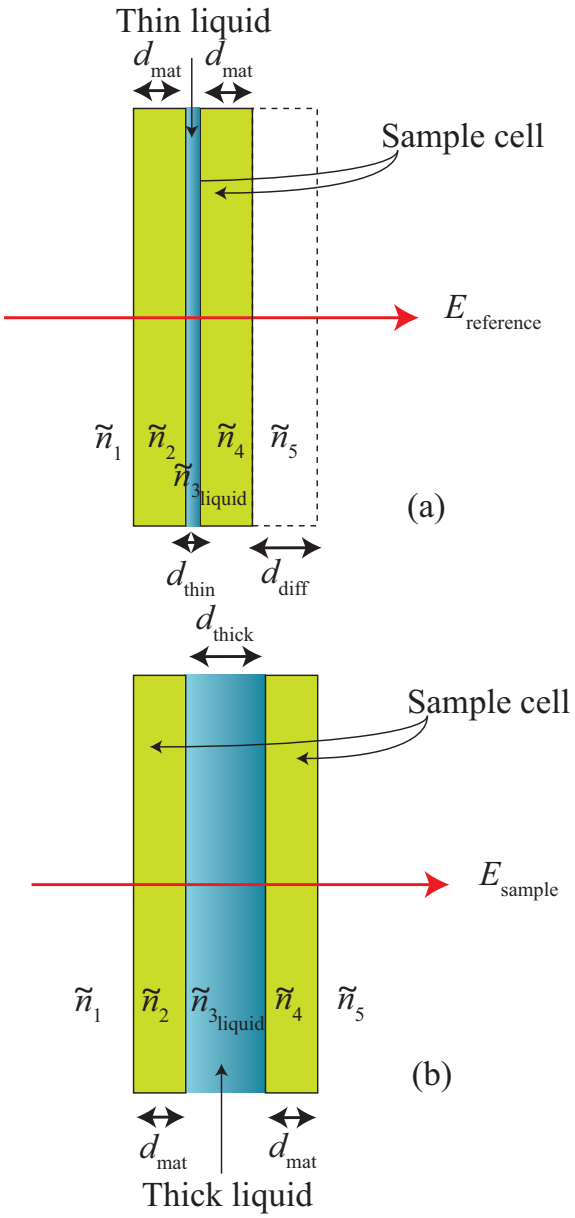

Figure 6.7. T-ray transmission notation for dual-thickness window cell geometry. This figure illustrates the notation for modelling T-ray propagation through liquid sample of two different thicknesses. The reference signal, $E_{reference}$ and the sample signal, E_{sample} travels through the same interfaces to ensure the reflections at the dielectric interfaces are identical. The only difference between reference and sample will be the thickness of the liquid being measured. Dual-thickness window cell geometry is used for experiments in Ch. 8.

Therefore, based on ratio formula, the complex transmission coefficient for dual-thickness window cell geometry is expressed as

$$\widetilde{T}(\omega) = \frac{P_{3_{\text{thick}}}(\omega, d_{\text{thick}})}{P_{3_{\text{thin}}}(\omega, d_{\text{thin}}) \cdot P_{\text{diff}}(\omega, d_{\text{diff}})} , \tag{6.23}$$

which can also be written as follows:

$$\widetilde{T}(\omega) = \frac{\exp(\frac{-j\tilde{n}_3\omega d_{\text{thick}}}{c})}{\exp(\frac{-j\tilde{n}_3\omega d_{\text{thin}}}{c}) \cdot \exp(\frac{-j\tilde{n}_5\omega d_{\text{diff}}}{c})} . \tag{6.24}$$

Here, $\tilde{n}_5$ is the complex refractive index of air. The $\tilde{n}_{3_{\text{liquid}}}$ represents the complex refractive index of the liquid. Also, d_{thin} is the thickness of the thin liquid sample for a reference signal and d_{thick} is the thickness of the thick liquid sample for a sample signal (see Fig. 6.7).

Equation (6.24) simplifies to

$$\widetilde{T}(\omega) = \exp(\frac{-j\omega d_{\text{diff}}}{c}(\tilde{n}_{3_{\text{liquid}}} - 1)) . \tag{6.25}$$

with $\tilde{n}_5 = 1$ and $d_{\text{diff}} = d_{\text{thick}} - d_{\text{thin}}$. Also, by substituting $\tilde{n}_{3_{\text{liquid}}} = n_{3_{\text{liquid}}} - j\kappa_{3_{\text{liquid}}}$, one may obtain the the frequency dependent phase, $\phi(\omega)$, and extinction coefficient, $\rho(\omega)$, as follows:

$$\phi(\omega) = \frac{\omega d}{c}(n_{3_{\text{liquid}}}(\omega) - 1) , \tag{6.26}$$

$$\rho(\omega) = \exp(-\frac{\omega d_{\text{diff}}}{c}\kappa_{3_{\text{liquid}}}) . \tag{6.27}$$

Rearranging the above equations produces the THz material parameters,

$$n_{3_{\text{liquid}}}(\omega) = \frac{\phi(\omega)c_0}{\omega d} + 1 , \tag{6.28}$$

$$\kappa_{3_{\text{liquid}}}(\omega) = -\frac{c}{\omega d_{\text{diff}}} \ln[\rho(\omega)] . \tag{6.29}$$

The absorption coefficient α is commonly introduced as

$$\alpha(\omega) = 2\frac{\kappa_{3_{\text{liquid}}}(\omega)\omega}{c} , \tag{6.30}$$

which simplifies to

$$\alpha(\omega) = -\frac{2}{d_{\text{diff}}} \ln[\rho(\omega)] \, . \tag{6.31}$$

There are several ways to implement the dual-thickness window cell geometry. Mickan (2003) and Kindt and Schmuttenmaer (1996) demonstrated dual-thickness liquid measurements through high density polyethylene (HDPE) bag as shown in Fig. 6.8. The dual-thickness geometry was introduced by adjusting the thickness of the liquid inserted in the HDPE bag through the single axis stage. Also, dual-thickness geometry can be implemented by using the thickness adjustable window cells presented in Fig. 6.2 and 6.4. Spacers with different thicknesses are required to form dual-thickness geometry. Alternatively, a spinning wheel technique described in Ch. 8 can be used for implementing dual-thickness measurements.

NOTE:
This figure is included on page 86
of the print copy of the thesis held in
the University of Adelaide Library.

Figure 6.8. Dual-thickness liquid sample cell. This figures depicts a variable-length liquid sample cell using HDPE bag. The HDPE bag is placed in between the thick Telfon windows. The dual-thickness is achieved by moving one of the Teflon window forward and backward using a single axis stage. After Mickan (2003).

6.2.4 Reflection window cell geometry

A reflection geometry is useful when dealing with highly-absorbing samples where a transmission geometry may not be appropriate, i.e., polar liquids. In this section Total Internal Reflection (TIR) presented by Rønne *et al.* (1997) has been considered to elaborate reflection window cell geometry. In Fig. 6.9, as the liquid sample is placed at a normal incidence with respect to the THz beam, the reference signal is obtained from the first reflection between air and silicon window interface and the sample signal is detected through the following reflection that occured between the silicon and liquid interface. Therefore, one may write the spectral reflection ratio of sample and reference signals as follows:

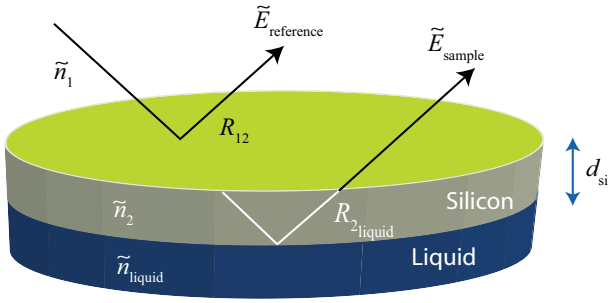

Figure 6.9. T-ray reflection notation for window cell geometry at normal incidence. This schematic illustrates the notation for modelling T-ray propagation through liquid sample placed at a normal incidence with respect to the THz beam. The reference signal is detected from the air-silicon window interface and the sample signal is detected from the silicon-liquid interface.

$$\widetilde{T}(\omega) = \frac{\widetilde{E}_{\text{sample}}(\omega)}{\widetilde{E}_{\text{reference}}(\omega)} = \rho e^{-j\phi} , \tag{6.32}$$

$$\widetilde{T}(\omega) = \frac{T_{12} R_{2_{\text{liquid}}} T_{21}}{R_{12}} \exp\left(\frac{-j2n_2 d_{\text{si}}\omega}{c}\right) . \tag{6.33}$$

According to Rønne *et al.* (1997), placing the liquid sample at a normal incidence to the THz beam allows one to calculate the material parameters analytically. If $n_1 \gg \kappa_1$ and $n_2 \gg \kappa_2$, the frequency dependent THz sample properties can be estimated by (Rønne *et al.* 1997, Mickan 2003),

$$n_{\text{liquid}}(\omega) = \frac{n_2(1-\rho^2)}{1+\rho^2+2\rho\cos\phi} , \tag{6.34}$$

$$\kappa_{\text{liquid}}(\omega) = \frac{2n_2\rho\sin\phi}{1+\rho^2+2\rho\cos\phi}\,. \tag{6.35}$$

In the above equations, Fabry-Pérot reflection term is ignored due to the sufficiently thick sample. However, in cases where thin samples are used, FP factors must be taken into account by calculating material parameters iteratively.

Fig. 6.10 shows a TIR set up for THz liquid measurements using a silicon window. With an assumption that the THz beam is normal incidence to the sample, the THz material parameters can be extracted using Eqs. 6.32 - 6.35.

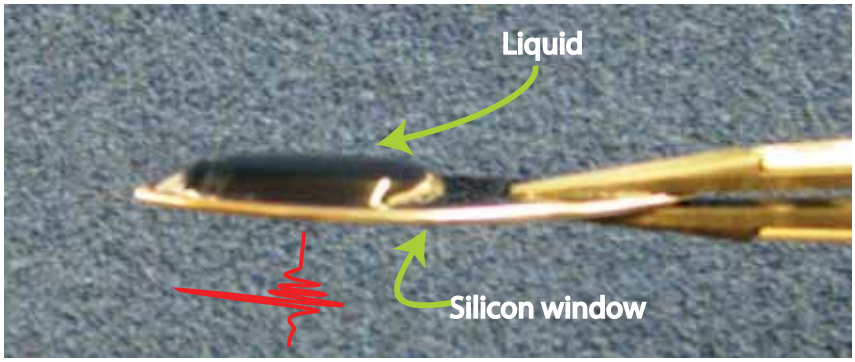

Figure 6.10. Reflection geometry liquid cell setup. This photo shows liquid sample on silicon window at normal incidence to the THz beam.

6.3 Chapter summary

The work presented in this chapter presents various types of window cell geometries used by the THz community for liquid spectroscopy. In this chapter, we have also shown our custom-built sample holders based on COC 5013L10 window material. Here, the window cell geometries are accompanied by the data analysis techniques. This chapter forms a basic understanding of window cell geometries that is essential for the development of the fixed dual-thickness window spinning wheel technique for liquid spectroscopy described in Ch. 8.

In the recent years, double-modulated terahertz differential time-domain spectroscopy (double-modulated THz-DTDS) scheme has been a topic of interest among the THz community. In the following chapter we develop a novel spinning wheel technique for material parameter measurement and demonstrate preliminary experimental results

showing that the fluctuations in the T-ray pulses affected by the $1/f$ noise characteristic of the modelocked laser can be improved by increasing the modulation frequency of the spinning wheel. The spinning wheel measurement technique in the following chapter is of significance particularly for THz spectroscopy of liquids where the presence of noise is particularly problematic.

THz material parameter extraction using a spinning wheel

DOUBLE-modulated terahertz differential time-domain spectroscopy (double-modulated THz-DTDS), is a technique that is based on dithering the sample under test. In this chapter, we report a measurement technique based on mounting the sample on a spinning wheel, in order to overcome fundamental limitations imposed by linear dithering. We demonstrate a proof-of-principle showing that noise decreases as a function of the spinning wheel modulation frequency. This technique does not suffer the mechanical noise limitation of traditional linear dithering and thus opens up future scope for further noise reduction via hardware advances in the modulation frequency of the wheel. The spinning wheel technique enables a rapid succession of measurements between the reference and sample signals with a single mechanical delay scan. As a result, an improvement in measurement time by at least a factor of two, as compared to the conventional THz-TDS measurement technique is observed. The spinning wheel technique is experimentally verified by measuring the dielectric properties of a thick polymer material.

7.1 Introduction

The rapidly evolving area of terahertz (T-ray) technology has drawn considerable attention for a variety of applications. Terahertz is currently of great interest in applications such as medical diagnostics (Png *et al.* 2008, Knobloch *et al.* 2002), chemical and biological identification (Fischer *et al.* 2007, Globus *et al.* 2006), and quality control (Ho *et al.* 2007). Due to the advent of THz technology, the measurement techniques used in conventional THz-TDS are still far less established as compared to other well-developed electromagnetic technologies such as MRI and X-rays. In a typical conventional THz-TDS setup, a complete scan consists of a reference (air) scan and a sample (material) scan. In order to obtain a high SNR, each scan requires a separate delay stage scan with a measurement time of several minutes depending on the time constant set by the lock-in amplifier. A number of significant studies have motivated the need for a fast and reliable THz measurement technique, including: fast scanning of terahertz signal using oscillating and rotary optical delay lines (Jin *et al.* 2007, Kim *et al.* 2008), real-time terahertz scanner for moving objects, and rapid-phase modulation for high speed terahertz imaging and spectroscopy (Sinyukov *et al.* 2008), and simultaneous reference and differential waveform acquisition (Iwaszczuk *et al.* 2009).

7.1.1 Objectives and framework

We demonstrate simulation and experimental results of a novel spinning wheel technique implemented using a double-modulated terahertz differential time-domain spectroscopy (double-modulated THz-DTDS) scheme (Mickan *et al.* 2004). The spinning wheel technique enables a rapid succession of measurements between the reference and sample signals with a single delay stage scan. This technique allows an improvement in the reference and sample measurement times by at least a factor of two as compared to the conventional THz-TDS measurement technique. The spinning wheel technique is experimentally verified using a polyvinyl chloride (PVC) polymer sample under test. A standardized sample thickness of 3 mm is used herein and this is a trade-off between maximising bandwidth and maximising THz interaction depth in the samples. This chapter is structured as follows: THz differential time-domain

spectroscopy (THz-DTDS) and double-modulated THz differential time-domain spectroscopy (double-modulated THz-DTDS) schemes are introduced in Section 7.2. Section 7.3 presents the spinning wheel mechanism implemented using the double modulated THz-DTDS. Simulation of the spinning wheel technique is described in Section 7.4. The experimental configuration and analytical formula used for signal extraction from the spinning wheel are explained in Sections 7.5 and 7.6. Discussion and validation of the results obtained via measurement of a PVC polymer sample under test are given in the following sections.

7.2 THz-DTDS and Double-modulated THz-DTDS

THz-DTDS scheme (Jiang *et al.* 2000) based on a differential signal measurement. The THz-DTDS was first used to measure the dielectric and optical properties of nanometer scaled dielectric films in the THz frequency band. The dielectric film is mounted on a hammer-like sample holder that is designed to be half coated and half uncoated with a thin sample film on a substrate (Fig. 7.1). The sample holder is mounted on

Figure 7.1. The hammer-like sample holder for a differential measurement technique. The sample holder is half coated and half uncoated with a thin film on a substrate, serving as sample and reference. After Jiang *et al.* (2000).

a galvanometer operating at f_{shaker} set at 16 Hz. Therefore, as the THz (T-ray) beam transmits through the dithered sample, a differential signal can be generated. Dithering the sample holder by covering the half coated thin film by a metal plate generates a differential reference signal. Thus, by taking the ratio of the differential signal over the differential reference signal, dielectric and optical properties of the sample film

can be determined. Recently, Mickan *et al.* (2002b) and Lee *et al.* (2003), investigated a double-modulated THz-DTDS technique whereby a double modulation scheme is used to extract the differential signal and the differential reference signal of a thin film. According to Mickan *et al.* (2002b), the double modulation technique is analogous to encoding information on a carrier wave in a radio system. Here, the modulated THz signal at lower frequency, f_{shaker}, is further modulated at a higher frequency, f_{chopper}. The double-modulated THz signal is then demodulated using two separate lock-in amplifiers. The first lock-in amplifier is demodulated at f_{chopper} to remove the carrier frequency component. Here, the lock-in amplifier is set to a low time constant to minimise the filtering effect. The output of the lock-in amplifier is then fed into the second lock-in amplifier. The second lock-in amplifier demodulates at f_{shaker} to produce the differential signal. The process is repeated for a differential reference measurement with the sample thin film covered by a metal plate thereby blocking the THz beam. In this case, an improvement in the shaking frequency of up to 66 Hz is achieved. In 2002, Mickan *et al.* (2002c) reported the use of double-modulated THz-DTDS for bioaffinity sensing. In their work, a surface recognition process of a highly specific label-free biotin-avidin complex was investigated. Furthermore, double-modulated THz-DTDS can be used for measuring thin liquid layers (Mickan *et al.* 2004). In that work, simultaneous dual-waveform acquisition, resulting in mean and amplitude signals, are introduced for the first time. Dual-waveform acquisition is implemented using an audio speaker to dither the sample.

Although working measurement techniques implemented with THz-DTDS or double-modulated THz-DTDS have been demonstrated, the limitation caused by the mechanical instability of the dithering mechanism introduces noise into the system. Furthermore, prior measurement techniques by Jiang *et al.* (2000), Mickan *et al.* (2002b), Lee *et al.* (2003), and Mickan *et al.* (2002c) can be time consuming especially in terms of sample preparation and measurement scan time—laser drift can be an issue, especially during the sample preparation period, since two separate scans are required to determine the dielectric properties of a material. Recently, several preliminary studies have been conducted by Balakrishnan *et al.* (2006), Withayachumnankul *et al.* (2007), Balakrishnan *et al.* (2008), and Balakrishnan *et al.* (2009a) on double-modulated THz-DTDS using a spinning wheel technique with simultaneous dual-waveform acquisition for measuring the dielectric properties of a material, however no detailed studies have been described so far.

Thus, in this chapter, we describe a detailed study of the spinning wheel technique with simultaneous dual-waveform acquisition for potentially improving the noise performance. Both simulation and experimental results of the spinning wheel technique are presented.

7.3 Spinning wheel

The spinning wheel (Fig. 7.2) is a mechanism we now introduce to address the mechanical instability in the prior linear dithering technique. The spinning wheel is designed

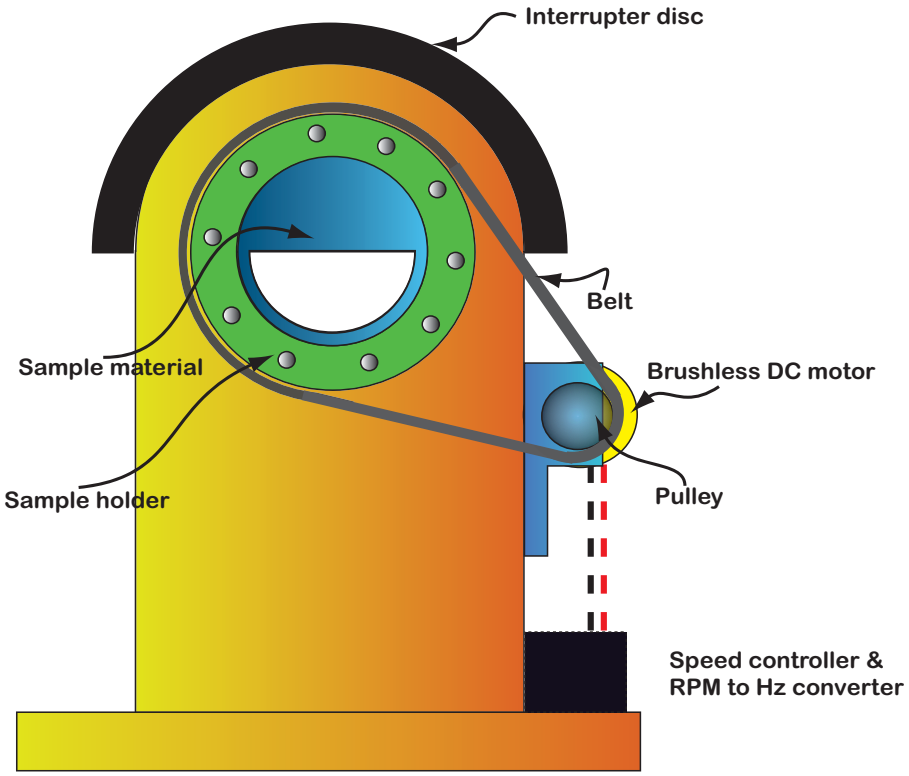

Figure 7.2. Spinning wheel for double-modulated THz-DTDS polymer measurements. The spinning wheel is located in the focal plane with a frequency setting of up to 310 Hz. As THz transmits through the rotating sample, a rapid succesion of measurements can be achieved.

to measure the reference and sample signals in quick succession with a single mechanical delay scan. The spinning wheel consists of five main parts: sample holder, sample material, photointerrupter and interrupter disc, rpm to Hz converter circuit and brushless DC motor set which consists of pulley, timing belt, high speed three-phase DC

motor, and speed controller. The sample holder is built using a robust stainless steel wheel supported by low friction ball bearings. The wheel is driven by a high speed brushless DC motor with a built-in governor mode. The governor mode is enabled to allow the motor to operate at a fixed speed. A custom-built pulley, a timing belt and a speed controller are attached to the motor. The sample is designed with half reference (air) and half sample (polymer) as shown in Fig. 7.3.

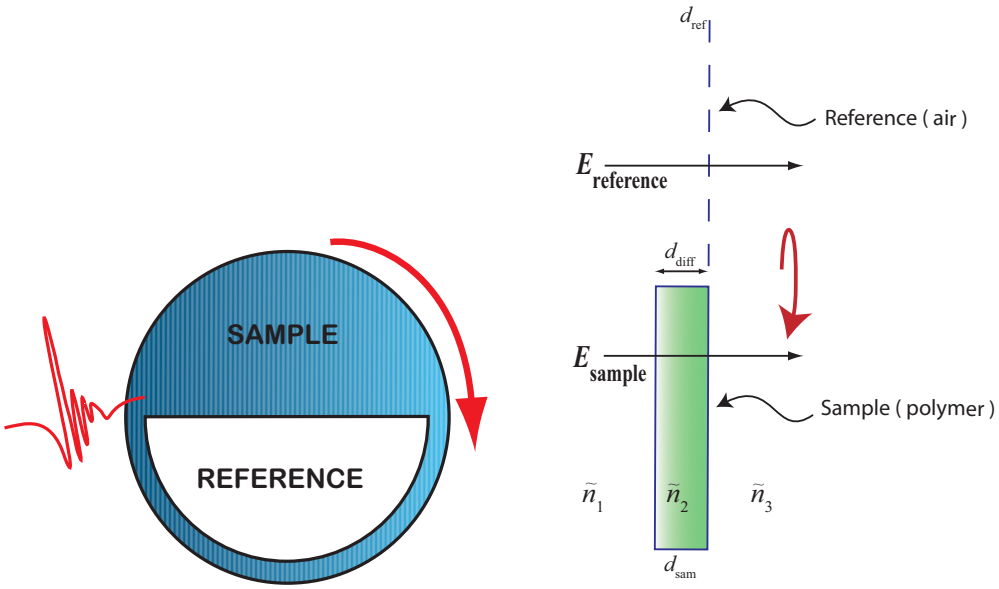

(a) Front view of sample material (b) Cross-section of sample material

Figure 7.3. Polymer sample design for a double-modulated THz-DTDS measurement. This figure depicts the sample under test in the double-modulated DTDS measurement. In Fig. 7.3a, the test sample is designed to be half reference (air) and half sample (polymer) and it is mounted onto the spinning wheel as shown in Fig. 7.2. In Fig. 7.3b, $\tilde{n}_1$ and $\tilde{n}_3$ are the refractive index of air, and $\tilde{n}_2$ is the refractive index of the sample material. Here, $d_{\text{diff}} = d_{\text{sam}}$ - d_{ref} is the thickness of the sample material. The electric field components for reference and sample signals are denoted as $E_{\text{reference}}$ and E_{sample} respectively.

This design allows a rapid succession of measurements between reference and sample as the wheel spins. A photointerrupter electronic circuit and a photointerrupter disc, which are used to convert the wheel's spinning speed (rpm) into frequency (Hz) are attached to the spinning wheel. Hence, the wheel is placed in the double-modulated THz-DTDS experimental setup described in Fig. 7.7 for a measurement. Transmitting THz beam through the rapidly rotated sample produces a rapid succession of measurements. The time between measuring the reference and sample is thereby dramatically reduced and is determined by the speed of the wheel.

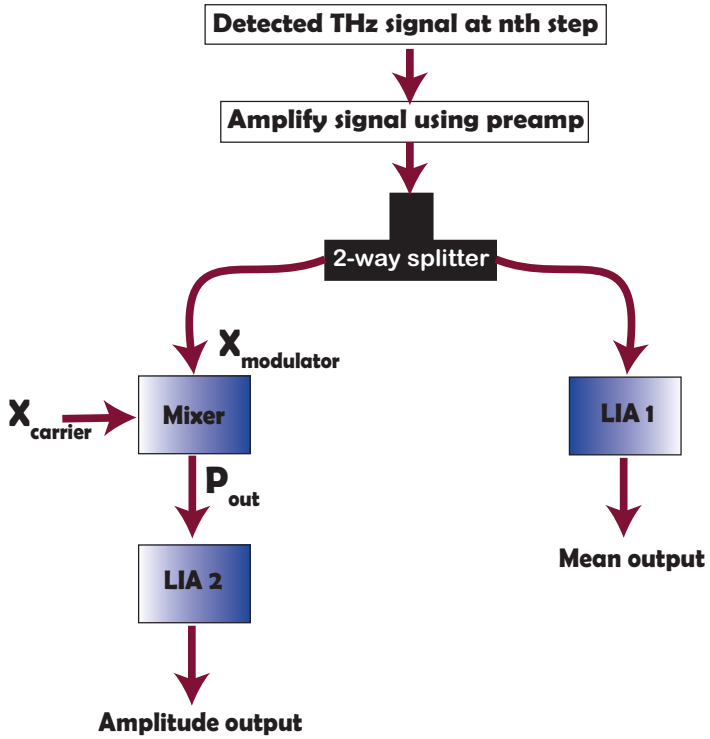

Figure 7.4. Flowchart of the simulation process for mean and amplitude signal extraction. The detailed explanation of the flowchart is given in the text.

7.4 Simulation

The rapid succession measurement using the spinning wheel technique is simulated using Matlab based on the flow chart presented in Fig. 7.4. The detected double-modulated THz signal at nth step is denoted as $E_{\mathrm{dm}}(\tau_{\mathrm{n}})$,

$$\begin{aligned} E_{\mathrm{dm}}(\tau_{\mathrm{n}}) = A_{\tau_{\mathrm{n}}}((1+\frac{4}{\pi}\sum_{k=1}^{\infty}\frac{\sin((2k-1)\omega_{\mathrm{chopper}}t+\phi_{\mathrm{chopper}})}{(2k-1)}) \\ \times(\frac{x-d}{x}(1+\frac{4}{\pi}\sum_{k=1}^{\infty}\frac{\sin((2k-1)\omega_{\mathrm{wheel}}t+\phi_{\mathrm{wheel}})}{(2k-1)})+d))\,, \end{aligned} \tag{7.1}$$

where $A_{\tau_{\mathrm{n}}}$ is the averaged amplitude with varying time delay, τ_{n} and n is the step number determined by the delay stage. Here, x is the thickness of the reference sample. The sample material thickness is defined as d. Here, the $\omega_{\mathrm{chopper}} = 2\pi f_{\mathrm{chopper}}$ and $\omega_{\mathrm{wheel}} = 2\pi f_{\mathrm{wheel}}$ represent the chopper frequency and the spinning wheel frequency respectively. Also, ϕ_{chopper} refers to the chopper phase while ϕ_{wheel} refers to wheel phase. The detected double-modulated signal is further amplified using a low-noise pre-amplifier before entering the 2-way power splitter. The time delay dependant amplified signal, $E_{\mathrm{p}}(\tau_{\mathrm{n}})$ can be written as follows:

$$E_{\mathrm{p}}(\tau_{\mathrm{n}}) = A_g E_{\mathrm{dm}}(\tau_{\mathrm{n}}), \tag{7.2}$$

where A_g denotes the gain applied to the detected signal. The amplified signal is then split using a 2-way power splitter to produce the split signals, $E_{\mathrm{s}_1}(\tau_{\mathrm{n}})$ and $E_{\mathrm{s}_2}(\tau_{\mathrm{n}})$. These signals enter the input channel of the lock-in amplifier one (LIA1) and the input channel, $X_{\mathrm{modulator}}$ of the mixer respectively. The $E_{\mathrm{s}_1}(\tau_{\mathrm{n}})$ and $E_{\mathrm{s}_2}(\tau_{\mathrm{n}})$ are described as follows:

$$E_{\mathrm{s}_1}(\tau_{\mathrm{n}}) = E_{\mathrm{s}_2}(\tau_{\mathrm{n}}) = \frac{1}{2} E_{\mathrm{p}}(\tau_{\mathrm{n}}). \tag{7.3}$$

As the input channel of LIA1 receives the $E_{\mathrm{s}_1}(\tau_{\mathrm{n}})$ from the splitter, the external chopper reference signal, $E_{\mathrm{c}}(t)$ with phase ϕ_c is fed into the reference input channel of LIA1 simultaneously for signal demodulation. The external chopper signal, $E_{\mathrm{c}}(t)$ is given by,

$$E_{\mathrm{c}}(t) = 1 + \left(\sum_{k=1}^{\infty} \frac{\sin((2k-1)\omega_{\mathrm{c}} t + \phi_{\mathrm{c}})}{(2k-1)}\right), \tag{7.4}$$

where $\omega_c = 2\pi f_{\mathrm{c}}$ is the reference frequency with phase, ϕ_{c}. Assuming that the chopper phase, ϕ_{chopper}, is synchronised to ϕ_{c} and the chopper frequency, $\omega_{\mathrm{chopper}}$ is synchronised to ω_{c}, the double-modulated signal is frequency-shifted after the demodulation stage. The demodulated output is then low-pass filtered to remove the unwanted frequency components. Thus, the output signal detected at LIA1 is denoted as the time delay dependant mean signal, $E_{\mathrm{mean}}(\tau_{\mathrm{n}})$.

The mixer illustrated in Fig. 7.4 is used as a multiplier. It consists of two input channels, $X_{\mathrm{modulator}}$ and X_{carrier}, and an output channel P_{out}. Here, P_{out} is the product of $X_{\mathrm{modulator}}$ and X_{carrier} input channels. Therefore, as the double-modulated signal from the splitter, $E_{\mathrm{s}_2}(\tau_{\mathrm{n}})$ enters $X_{\mathrm{modulator}}$ and the external chopper reference signal, $E_{\mathrm{c}}(t)$ is fed into X_{carrier} input channel simultaneously, a frequency shifting effect can be observed at the output channel of the mixer. Figure 7.5 shows the simulation-based frequency shifting effect at the mixer output channel.

Here, the mixer is designed without any filters. Therefore, the output of the mixer consists of frequency shifted components and noise. The mixer output, $P_{\mathrm{out}}(\tau_{\mathrm{n}})$ is

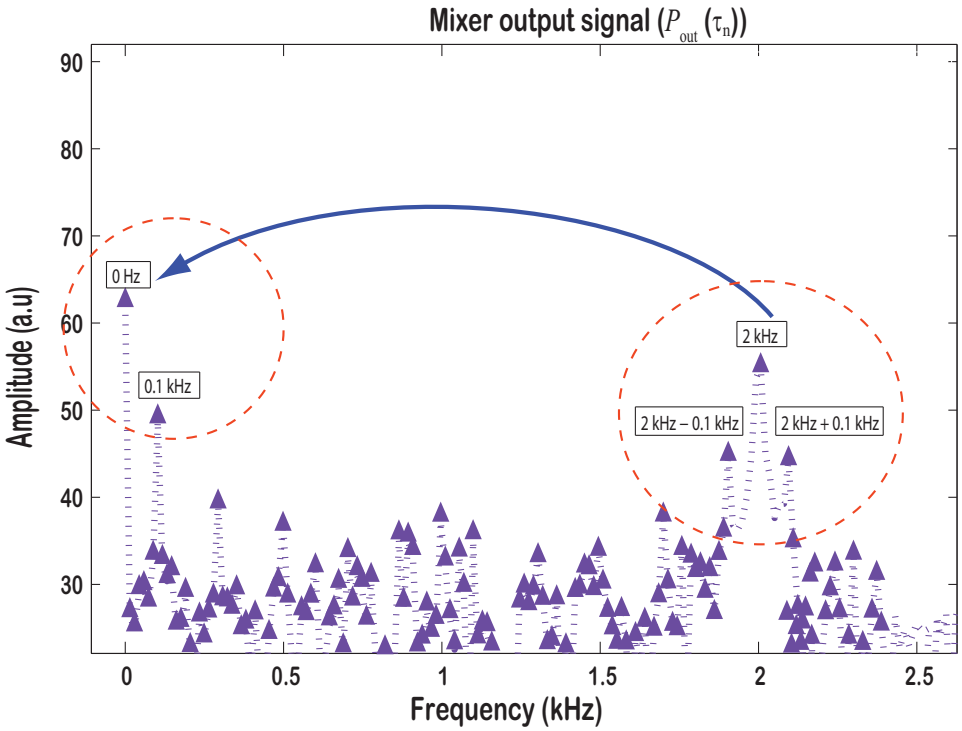

Figure 7.5. Simulated mixer output at nth step of the delay stage in frequency domain. This figure illustrates the product of $X_{\text{modulator}}$ and X_{carrier} channels of the mixer at the nth step of the delay stage in frequency domain. The $X_{\text{modulator}}$ input channel is fed with the simulated double-modulated signal, $E_{s_2}(\tau_n)$ with f_{chopper} of 2 kHz and f_{wheel} of 0.1 kHz and the X_{carrier} input channel is fed with the simulated chopper reference signal, $E_c(t)$ with f_c of 2 kHz. Thus, the simulated $E_{s_2}(\tau_n)$ consists of a sum component (2 kHz + 0.1 kHz) and a difference component (2 kHz - 0.1 kHz) is frequency shifted as illustrated in the figure above. With the assumption that the phase and frequency components of $E_{s_2}(\tau_n)$ synchronises to the phase and frequency components of $E_c(t)$, one can deduce the output of the mixer, $P_{\text{out}}(\tau_n)$ as shown in the figure. Therefore, the simulated double-modulated signal will be shifted towards the DC at the output of the mixer. The shifted components will then enter the input channel of LIA2 for further demodulation process to produce the amplitude signal.

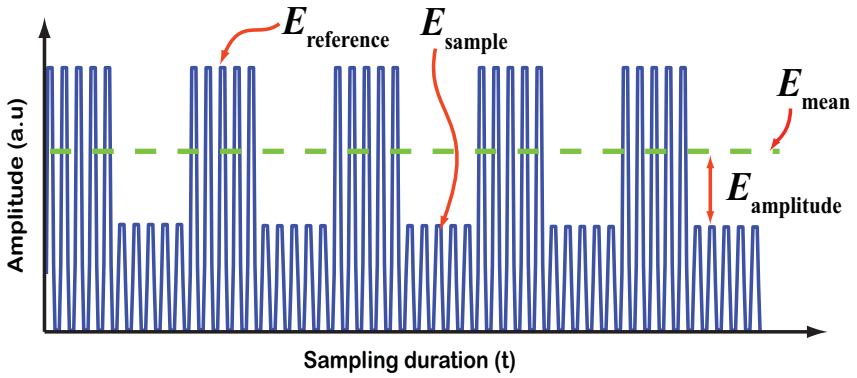

Figure 7.6. Time-domain simulated output signal of a mixer at nth step of the delay stage. This figure depicts a simulated output of the mixer at nth step of the delay stage. A rapid succesion of measurements produce a square wave pattern at the output of the mixer. This square wave consists of reference signal, $E_{\text{reference}}(\tau_{\text{n}})$, sample signal, $E_{\text{sample}}(\tau_{\text{n}})$, mean signal, $E_{\text{mean}}(\tau_{\text{n}})$, and amplitude signal, $E_{\text{amplitude}}(\tau_{\text{n}})$.

then fed into the second lock-in amplifier (LIA2). Here, LIA2 further demodulates the output signal from the mixer with wheel reference signal, $E_{\text{w}}(t)$. The $E_{\text{w}}(t)$ can be deduced as follows:

$$E_{\text{w}}(t) = 1 + \left(\sum_{k=1}^{\infty} \frac{\sin((2k-1)\omega_{\text{w}}t + \phi_{\text{w}})}{(2k-1)}\right), \tag{7.5}$$

where $\omega_{\text{w}} = 2\pi f_{\text{w}}$ is the reference frequency with phase, ϕ_{w}. With an assumption that the phase, ϕ_{wheel} is synchronised to the phase of the wheel reference signal, ϕ_{w} and the wheel frequency, ω_{wheel} is synchronised to ω_{w}, the demodulated mixer output is further frequency shifted after the demodulation process. Thus, the demodulated signal is low-pass filtered to produce the time delay dependant amplitude signal, $E_{\text{amplitude}}(\tau_{\text{n}})$ at the output of LIA2. Therefore, with the extracted mean and amplitude signals, the reference and sample signals can be obtained. A further explanation of the reference signal and sample signal extraction is described in the analysis section. Figure 7.6 shows the simulated time-domain output signal of the mixer at nth step of the delay stage. In this figure, the relationships between the mean, amplitude, reference, and sample signals are depicted. Further information on the simulation technique can be obtained from Appendix A.

7.5 Experimental Method

The double-modulated DTDS setup for a polymer material measurement is shown in Fig. 7.7. A MiraSeed Ti-sapphire femtosecond modelocked laser is used as a source of optical pulses. It is pumped by Verdi V6 laser with a wavelength of 532 nm. The femtosecond laser produces an output pulse duration of 20 fs at a repetition rate of 76 MHz. This laser has an output power of 1 W with a centered wavelength at 800 nm. The laser is split into a pump beam and a probe beam using a beamsplitter. The pump beam is modulated by an optical chopper at a frequency of 2.2 kHz. The modulated beam is then focused on an emitting photoconductive antenna using a plano-convex optical lens. The emitting antenna is biased at 90 Vdc using a standard low current power supply.

The modulated beam is incident on the emitter for generating the THz pulse. The THz pulse is collimated and focused onto the rotating polymer material using the first pair of off-axis parabolic mirrors. Here, the spinning wheel speed is set to a frequency range of 66 Hz to 310 Hz. The THz pulse transmits through the rotating sample and is recollimated and focused onto the photoconductive detector antenna using the second pair of off-axis parabolic mirrors. The probe beam gates the transmitted THz pulse by focusing the laser beam onto the photoconductive antenna at the detector. Two SR830 lock-in amplifiers, a low-noise SR560 pre-amplifier and a custom-built electronic mixer based on an MC1495P multiplier chip are used for signal extraction in this setup. The details of the signal extraction are given in Sec. 7.5.1.

7.5.1 Lock-in amplifier configuration

The lock-in amplifier configuration for mean and amplitude signal extraction is shown in Fig. 7.8. First, the detected double-modulated THz signal is fed into the preamplifier for signal amplification. The amplified signal is then fed into a low noise 2-way power splitter. Thus, one end of the splitter output is connected to the input channel of the first lock-in amplifier (LIA1) and the other end of splitter output is fed into the $X_{\text{modulator}}$ input channel of the mixer. Here, the LIA1 input signal is demodulated using the external chopper reference signal. Autophasing the LIA1 input signal to the external chopper reference signal synchronises the phase of the input signal to the phase of the external chopper reference signal. Thus, synchronised signals are low-pass filtered to produce a mean signal at the output channel of LIA1. The mixer input signal

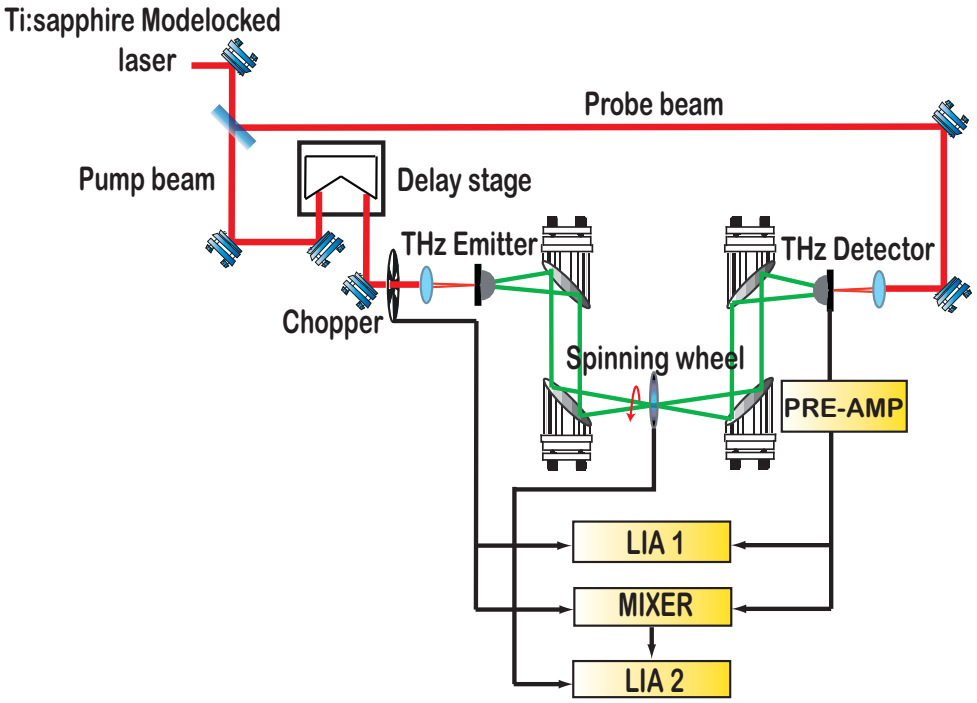

Figure 7.7. Double-modulated DTDS spectrometer schematic for polymer materials measurement. This schematic diagram illustrates a double-modulated DTDS spectrometer configured for characterizing dielectric properties of polymer materials. The sample material placed at the focal plane is modulated at f_{wheel} of 66 Hz to 310 Hz. A Ti-sapphire femtosecond laser is split into pump beam and probe beam. The pump beam is modulated at 2.2 kHz using a mechanical chopper and focused on an emitting photoconductive antenna to generate THz pulse. The THz pulse is collimated and focused onto the rotating sample. The transmitted THz pulse is recollimated and focused onto the photoconductive detector antenna. The probe beam gates the incoming THz pulse at the detector. The detected THz pulse is pre-amplified and fed into lock-in amplifiers and mixer for mean and amplitude signals extraction.

is demodulated with the external chopper reference signal, however, no filtering is applied to the output signal of the mixer. As a result, the output of the mixer consists of frequency shifted components and noise as described in Fig. 6.5. Here, a scaling factor of $2E_{\text{amplitude}}$ is applied to the mixer output before feeding into the input channel of the second lock-in amplifier (LIA2). The mixer, based on the MC1495P multiplier, has the facility for applying this scaling factor via an external variable resistor. The scaled output of the mixer is fed into the input channel of LIA2. The input signal is then demodulated using the external wheel reference signal. Autophasing the input signal to the wheel reference signal, synchronises the phase of the wheel reference signal with

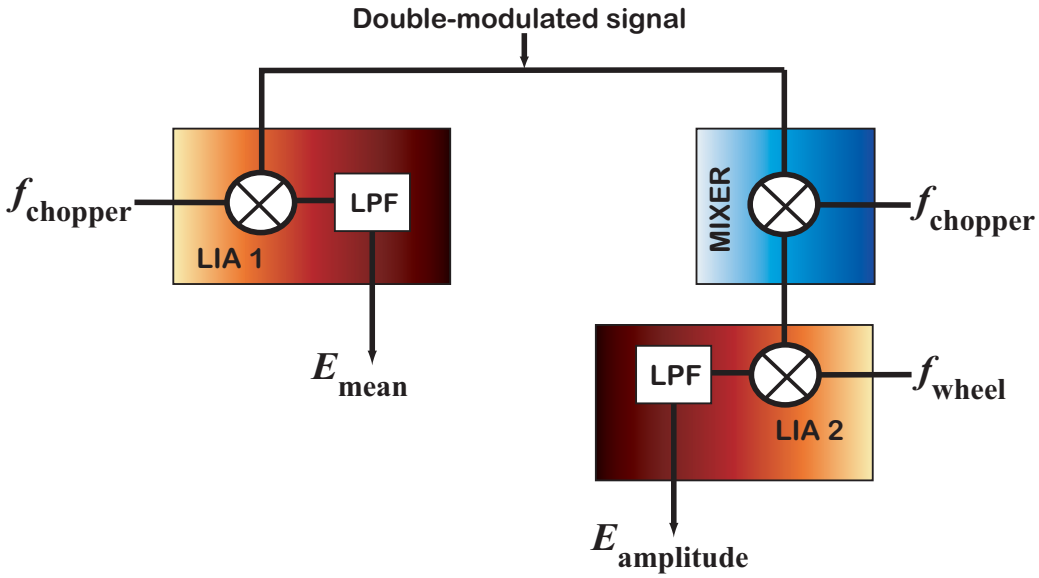

Figure 7.8. Lock-in amplifier configuration for mean and amplitude signals extraction. This figure shows a simulataneous dual-waveform acquisition (mean and amplitude) using two lock-in amplifiers and a mixer. The detailed explanation of the lock-in amplifier configuration is given in the text.

the input signal. The synchronised signals are then low pass filtered to produce an amplitude signal at the output channel of LIA2. Therefore, with the extracted mean and amplitude information, the reference and sample signals can be calculated according to Eqs. (7.6) and (7.7).

7.6 Analysis

Given that terahertz radiation is incident on the rotating sample, the mean and amplitude signals are then extracted according to the lock-in amplifier configuration described in Fig. 7.8. Therefore, based on the extracted mean and amplitude signals, the reference and sample signals can be calculated as follows (Mickan *et al.* 2004):

$$\widetilde{E}_{\text{reference}}(\omega) = \widetilde{E}_{\text{mean}}(\omega) + \widetilde{E}_{\text{amplitude}}(\omega)\,, \tag{7.6}$$

$$\tilde{E}_{\text{sample}}(\omega) = \widetilde{E}_{\text{mean}}(\omega) - \widetilde{E}_{\text{amplitude}}(\omega)\,. \tag{7.7}$$

A spectral component of the reference and sample signals can be modelled based on the polymer material design presented in Fig. 7.3. Thus, the reference and sample signal can also be written as follows (refer to Sec. 3.3.1):

$$\widetilde{E}_{\text{sample}}(\omega) = T_{12}(\omega).\, P_2(\omega, d_{\text{sam}}).\, T_{23}(\omega).A(\omega).\text{FP}(\omega)\ , \tag{7.8}$$

$$\widetilde{E}_{\text{reference}}(\omega) = T_{13}(\omega).\, P_{\text{air}}(\omega, d_{\text{ref}}).\, A(\omega)\ . \tag{7.9}$$

Hence, the complex transmission coefficient $T(\omega)$, is determined by taking the ratio of E_{sample} and $E_{\text{reference}}$,

$$\widetilde{T}(\omega) = \frac{\widetilde{E}_{\text{sample}}(\omega)}{\widetilde{E}_{\text{reference}}(\omega)} = \rho e^{-j\phi}\ . \tag{7.10}$$

With the assumption that the complex refractive index of air, $\tilde{n}_1$ and $\tilde{n}_3 = 1$, the complex transmission coefficient can be simplified as follows:

$$\widetilde{T}(\omega) = \frac{4\widetilde{n}_2(\omega)}{(1+\widetilde{n}_2(\omega))^2} \exp\left(\frac{-i\omega d_{\text{diff}}}{c}(\widetilde{n}_2(\omega) - 1)\right) \text{FP}(\omega)\ , \tag{7.11}$$

where the frequency-dependant complex refractive index $\widetilde{n}_2(\omega) = n_2(\omega)$ - $j\kappa_2(\omega)$. Here, $n_2(\omega)$ and $\kappa_2(\omega)$ refer to the refractive index and extinction coefficient of the sample respectively. The $d_{\text{diff}} = d_{\text{sam}}$ - d_{ref} where d_{sam} is the thickness of the sample material and d_{ref} is the thickness of the reference (Fig. 7.3b). The angular frequency is denoted as ω and the speed of light is denoted as c. The Fabry-Pérot reflection in the sample is labelled as $\text{FP}(\omega)$. According to Mickan *et al.* (2002b), the complex refractive index of a sample can be estimated by an iterative approximation or analytically. In our study, since the sample measured is sufficiently thick (Balakrishnan *et al.* 2009b, Fischer 2005), the Fabry-Pérot reflections can be easily isolated. Thus, the analytic expression for n and κ can be made through approximation given in (Duvillaret *et al.* 1999). Here, we define the noise percentage, μ_{x} of the THz system as the standard deviation of the reference temporal electric field, $\Delta E_{\text{reference}}$ over the mean reference temporal electric field, E_{mref} (Mickan *et al.* 2004, Jiang *et al.* 2000). The measurement is repeated five times for a noise percentage calculation. In this experiment, the lock-in amplifier time constant is set at 100 ms for both LIA1 and LIA2. The noise percentage, μ_{x} can be expressed as follows:

$$\mu_{\text{x}} = \frac{\Delta E_{\text{reference}}}{E_{\text{mref}}} \times 100\%\ . \tag{7.12}$$

7.7 Results and discussion

As a proof-of-concept, the spinning wheel technique is experimentally verified using the following polymer material: polyvinyl chloride (PVC). The results obtained are compared with the results from a conventional THz-TDS measurement technique. From here on we have labelled the results obtained from the double-modulated spinning wheel as *double-modulated* and the results obtained from the conventional THz-TDS as *conventional*.

7.7.1 Polyvinyl chloride: PVC

PVC is optically opaque and its dielectric properties are well explored in terehertz range (Balakrishnan *et al.* 2009b, Withayachumnankul *et al.* 2008, Piesiewicz *et al.* 2007a, Nagai and Fukasawa 2004) as well as in the optical regime (Al-Ramadin 2000). In this section, the dielectric properties of PVC in the terahertz band are measured using the double-modulated spinning wheel technique. The results obtained are then compared with the dielectric properties of PVC obtained from the conventional THz-TDS technique. These results agree well with the literature data (Balakrishnan *et al.* 2009b, Withayachumnankul *et al.* 2008, Piesiewicz *et al.* 2007a). At every nth step of the delay stage, reference and sample signals are measured in a rapid succession. This produces mean and amplitude waveforms simultaneously at the output channel of LIA1 and LIA2 (Fig. 7.9a). Therefore, with the mean and amplitude signals, the reference and sample temporal electric field can be obtained by using the formulas given in Eqs. (7.6) and (7.7). In Fig. 7.9b, the double-modulated reference and sample waveforms are compared with the conventional reference and sample waveforms. A close match is observed between the double-modulated signals and the conventional signals. However, since the double-modulated and the conventional TDS measurements were not conducted simultaneously, a slight deviation is seen on the conventional TDS measurement. The deviation is mainly caused by the $1/f$ noise fluctuation originated from the modelocked laser (Yasui and Araki 2005, Son *et al.* 1992, Poppe *et al.* 1998).

Figure 7.10 compares the absorption coefficient, α, and refractive index, n, of PVC obtained through the double-modulated spinning wheel technique and conventional THz-TDS. A close match is observed. In this measurement, the thickness of the sample under test is set at 3 mm to show proof-of-concept, however, measurement on a very thin sample can be carried out with an appropriate sample preparation technique.

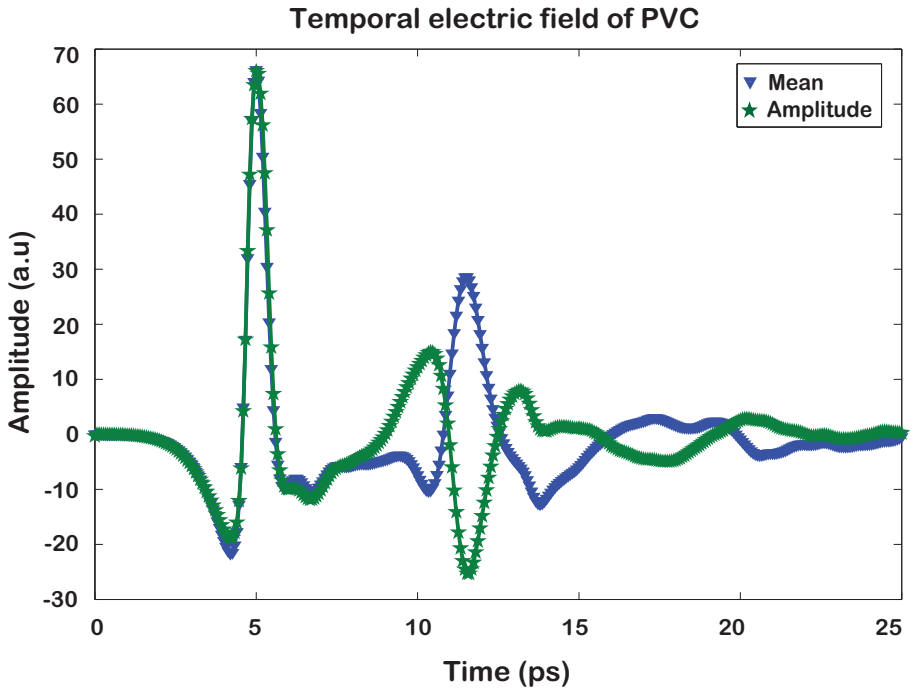

(a)

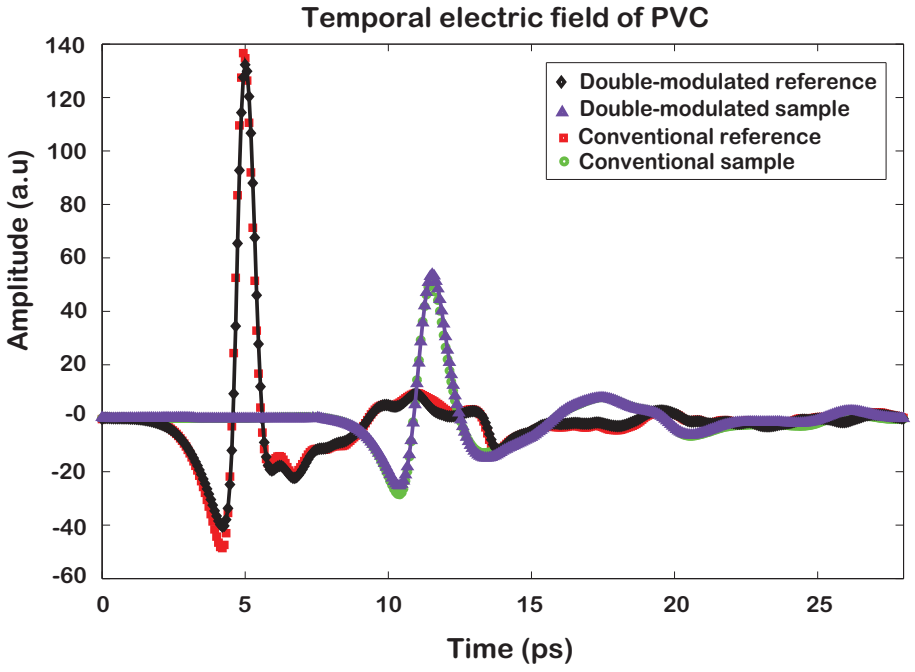

(b)

Figure 7.9. Mean and amplitude waveforms of PVC. Figure 7.9a shows the mean and amplitude waveforms of PVC obtained through the double-modulated DTDS technique and Fig. 7.9b shows the double-modulated and conventional reference and sample waveforms of PVC.

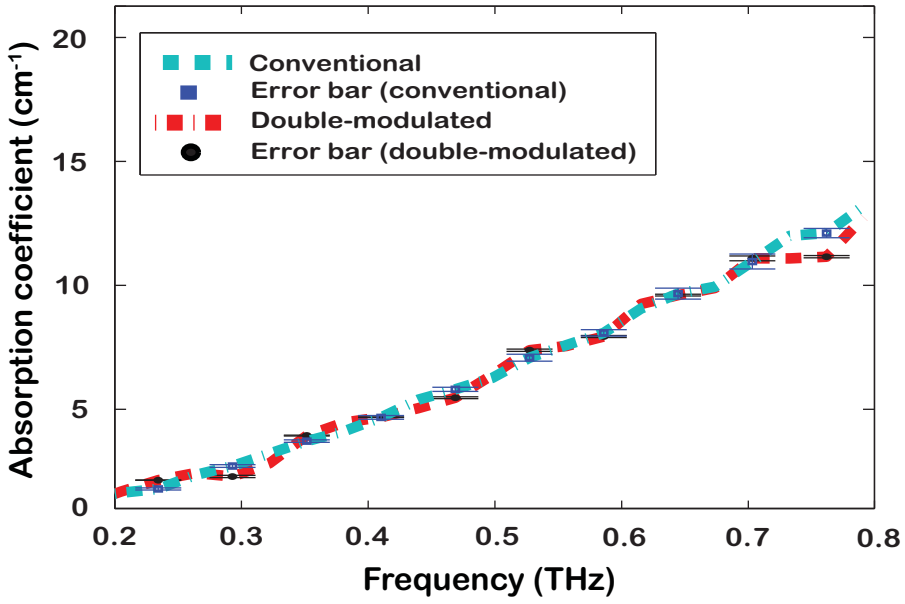

(a)

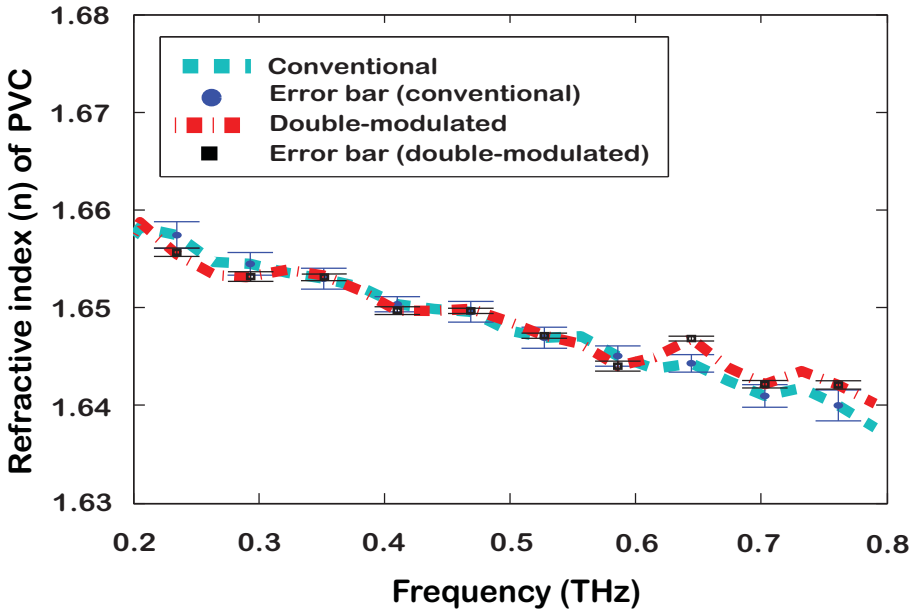

(b)

Figure 7.10. Absorption coefficient and refractive index of PVC. This figure depicts the double-modulated and conventional absorption coefficient and refractive index of PVC, indicating a close match. The error bars indicate uncertainties in the conventional technique and double-modulated spinning wheel technique. According to the FFT of the temporal profile, it was observed that the linear region for the sample signal is limited to 0.8 THz and the signal is noisy thereafter.

In order to compare the noise performance of the double-modulated spinning wheel technique with conventional THz-TDS, five averages of reference scans are obtained and analysed according to the formula described in Eq. (7.12). Here, in order to calculate the noise percentage appropriately, we have only considered the fluctuations in the T-ray pulses, caused by the laser fluctuations. Thus, it is found that noise percentage, μ_x, of conventional THz-TDS is 1.84% as compared to 1.22% for the double-modulated spinning wheel technique. Here, the noise percentage of 1.22% is obtained when the spinning wheel is modulated at 310 Hz. Therefore, an improvement of 30% as compared to the conventional THz-TDS has been demonstrated. Thus, we confirm that the noise percentage present in the THz system can be reduced by using the spinning wheel technique. Figure 7.11 shows the noise percentage of the THz system detected using the spinning technique as a function of modulation frequency. In this work, a preliminary result showing that the fluctuations in the T-ray pulses affected by the $1/f$ noise characteristic of the modelocked laser can be improved by increasing the modulation frequency of the spinning wheel. Thus, the results presented in this work agree with the theoretical and experimental work presented by Mickan *et al.* (2004).

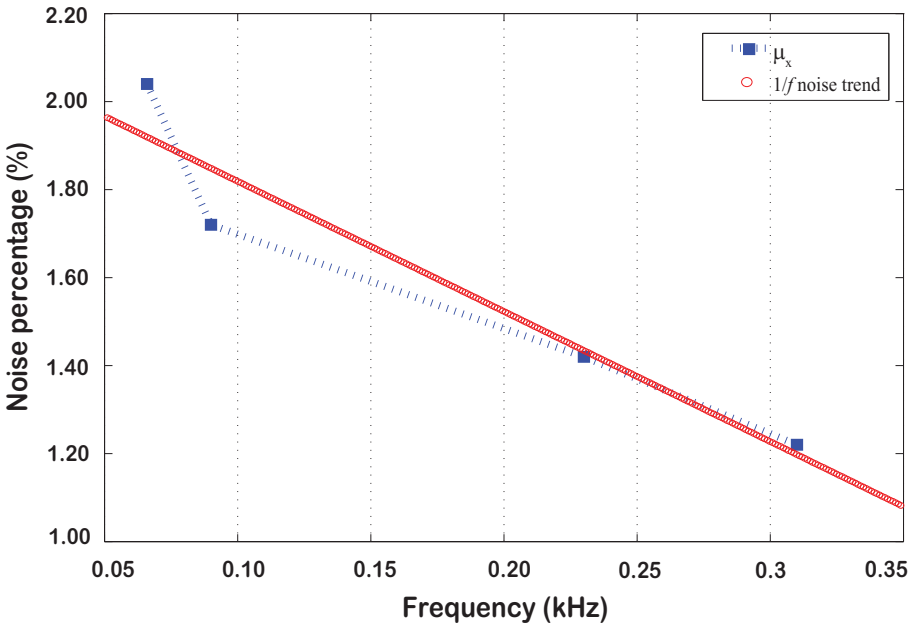

Figure 7.11. Noise percentage, μ_x of the THz system detected using a spinning wheel technique as a function of modulation frequency. This figure illustrates that as the modulating frequency of the wheel increases, the noise present in the THz system reduces.

7.8 Chapter summary and recommendation

We have developed a novel THz spinning wheel technique for material parameter measurement and demonstrate preliminary experimental results showing that the fluctuations in the T-ray pulses affected by the $1/f$ noise characteristic of the modelocked laser can be improved by increasing the modulation frequency of the spinning wheel. This technique is successfully implemented using a double-modulated terahertz differential time-domain spectroscopy (double-modulated THz-DTDS) experimental setup. We demonstrate measurements in rapid succession, requiring one mechanical delay scan for the sample and reference signals. This results in a reduction in the measurement time of the reference and sample signals by at least a factor of two. We validate the technique using thick polymer test sample. A good agreement in the resulting dielectric parameters is produced when compared with the conventional THz-TDS technique. Thus, this demonstrates the accuracy of the double-modulated THz-DTDS spinning wheel technique. The noise level that is present in our double-modulated technique is lower than that in conventional TDS, especially as the modulating frequency of the wheel increases. An improvement of 30% as compared to the conventional THz-TDS has been demonstrated. The results herein represent proof-of-principle, and the noise level that is present in double-modulated THz-DTDS is not fundamental but can be reduced, in principle, by development of hardware that effectively increases the modulation frequency introduced by the spinning wheel. Preliminary experiments indicate the potential of this technique for achieving a better noise performance, which is of significance particularly for THz spectroscopy of polar liquids where the signal-to-noise ratios are typically low due to high absorption coefficient.

The initial demonstration of the spinning wheel technique leads to THz spectroscopy of homogeneous polar liquids in the following chapter. In the next chapter, the spinning wheel mechanism is now coupled with a fixed dual-thickness window geometry to address the limitation imposed on linear dithering technique. We demonstrate for the first time a reduction to less than 5 μm in sample thickness error with the implementation of the fixed dual-thickness geometry as compared to 100 μm sample thickness error introduced by the linear dithering technique.

Chapter 8

Fixed dual-thickness terahertz liquid spectroscopy

CONVENTIONAL double-modulated terahertz differential time-domain spectroscopy (double-modulated THz-DTDS) of liquids requires linear dithering of the sample to rapidly vary the sample thickness, in order to produce the required sample and reference signals. Linear dithering, however, imposes a fundamental limitation as it introduces mechanical noise into the system, thereby contributing to measurement uncertainty. In this chapter, we address this limitation for the THz spectroscopy of liquids, by using a fixed dual-thickness sample mounted on a spinning wheel. The concept of spinning the sample allows rapid switching between two fixed sample thicknesses, in order to produce sample and reference signals without the introduction of added mechanical noise. We validate this new technique by measuring the dielectric properties of a number of liquids, and confirm the results against the Debye relaxation model.

8.1 Introduction

Spectroscopic studies on liquid in the terahertz (T-ray) regime have been a topic of interest in recent years. Terahertz liquid spectroscopy allows an analysis of chemical composition and provides a better understanding of the solvation dynamics of various types of liquids. A number of significant studies have motivated the need for THz spectroscopy of liquids, including: spectroscopy of biomolecules in aqueous solutions (Globus *et al.* 2006), spectroscopy of inflammables in beverage plastic bottles (Ikeda *et al.* 2005), spectroscopy of polar and non-polar liquids (Jepsen *et al.* 2007, Kindt and Schmuttenmaer 1996, Pedersen and Keiding 1992, Thrane *et al.* 1995). Although it has been shown that liquid spectroscopy using T-rays is feasible, the absorption coefficient for liquid water shows a very high THz absorption, 200 - 230 cm^{-1} at 1 THz (Kindt and Schmuttenmaer 1996, Thrane *et al.* 1995). Recently, many measurement techniques have been introduced to improve the sensitivity of THz liquid measurements. Hirori *et al.* (2004) implemented attenuated total reflection spectroscopy (TD-ATR) for highly absorbing materials such as polar liquids and biomolecules in aqueous solution. Interaction between the sample and the evanescent wave propagating along a prism can be detected via the TD-ATR measurement technique. Moreover, Cheng *et al.* (2008) demonstrated liquid measurements using the evanescent field of a silicon waveguide. In their work, the optical properties of a liquid are obtained based on the interaction between the evanescent wave of a cylindrical silicon waveguide and the liquid sample. Moreover, implementation of simultaneous measurement of the reference and sample signals using two separate pyroelectric sensors is introduced. In another study conducted by Mickan *et al.* (2004), a linear liquid dithering technique using a double-modulated differential time-domain spectroscopy (double-modulated DTDS) has been explored. The linear dithering technique used here allows a dual-thickness measurement where the reference and sample signals are detected through a thick and a thin version of the same liquid. Furthermore, a simultaneous dual-waveform acquisition, resulting in mean and amplitude signals, is achieved by this technique. Although dithering has been demonstrated, inaccuracies in the dual-thickness measurement introduced by the mechanical instability of the dithering mechanism is significantly large. Also, the presence of Fabry-Pérot reflections, due to the very thin sample cell, limits the dithering performance. Furthermore, the presence of macroscopic and microscopic bubbles in a liquid can hinder the accuracy of the measurements.

8.1.1 Objectives and framework

In this chapter, we demonstrate a fixed dual-thickness THz liquid measurement using a spinning wheel technique to address the limitation imposed by conventional linear dithering. By mounting a fixed dual-thickness sample on a spinning wheel, we remove the uncertainty introduced by linear dithering. As will be shown in Sec. 8.2, this technique has added advantage of allowing a quick succesion of measurements between sample and reference. Furthermore, by spinning a liquid sample the bubbles migrate towards the spin axis thereby managing the problem of bubble-induced inhomogeneity in the liquid. The experimental setup for implementing this technique is disccussed in Sec. 8.3. The lock-in amplifier setting for signal extraction and the sample preparation techniques are also discussed in this section. In Sec. 8.4, the mathematical formulas used for signal analysis are presented. In the following section, the results and discussion obtained for a number of liquids are shown.

8.2 Spinning wheel

Figure 8.1 shows the spinning wheel prototype for a fixed dual-thickness terahertz liquid measurement. A spinning wheel is a robust and reliable mechanical device implemented to address the limitation of the linear dithering of the sample. Here, the optical characteristics of liquids are determined using a dual-thickness geometry presented by Mickan *et al.* (2004). However, in that paper, a polyethylene bag, which is susceptible to Fabry-Pérot reflections is used as a window material to hold the liquid sample. The dual-thickness measurement was achieved using an audio speaker to dither the liquid sample, leading to an estimated sample thickness error of approximately 100 μm. In this work, the dual-thickness geometry is achieved by using a fixed thick layer and a fixed thin layer of the same liquid. As the spinning wheel is designed for a transmission experimental setup, the fixed dual-thickness geometry is implemented using a window material known as (TOPAS) cyclic-olefin copolymer (COC) 5013L10. This is because COC 5013L10 is optically transparent, high in transmission and has a low hygroscopicity (more in Ch. 4 and 5), which makes it ideal for a terahertz liquid spectroscopy (more details in Ch. 4 and 5). With careful design consideration and molding procedures, the error present in the fixed dual-thickness geometry (Fig. 8.2)

is reduced to approximately 5 μm. Furthermore, this technique has an additional advantage of allowing bubble-free measurements. The bubbles present in the liquid are pushed to the center of the window cell as the wheel spins.

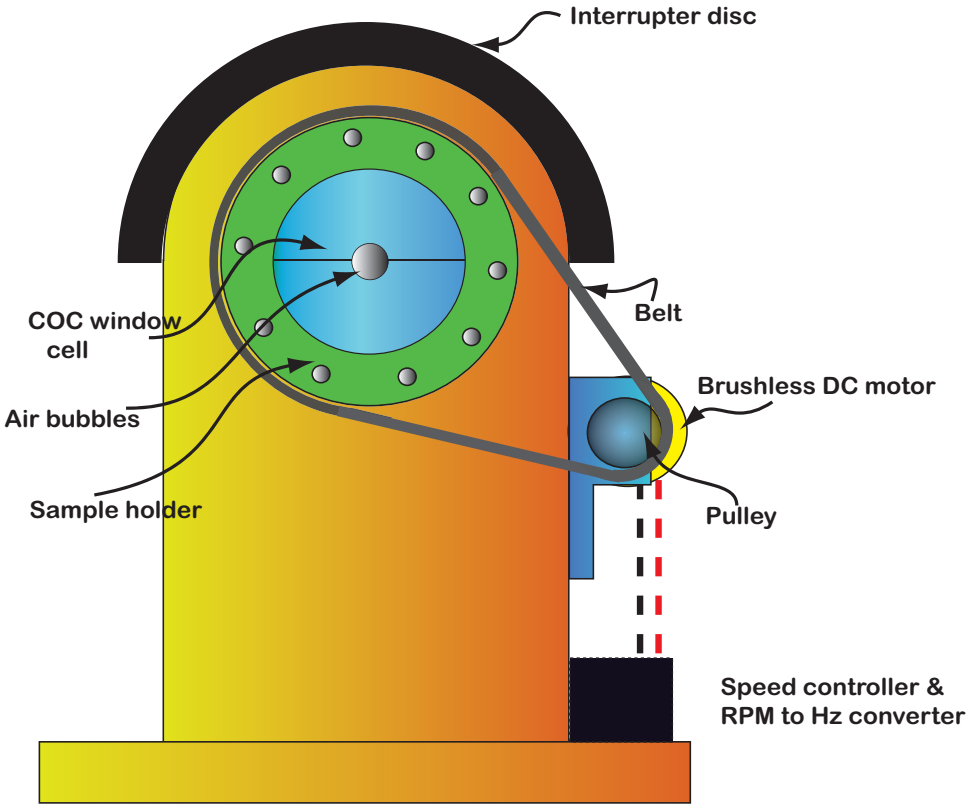

Figure 8.1. Spinning wheel for double-modulated DTDS dual-thickness liquid measurement. This figure shows a prototype of the spinning wheel sample holder for a dual-thickness liquid measurement. The wheel is located in the focal plane with a speed setting of 70 Hz. Here, a rapid succession measurement can be achieved as the THz beam transmits through the rotating sample. Due to the buoyancy effect, any excess air bubbles present in the liquid sample are desirably pushed to the center of the window cell as the wheel spins.

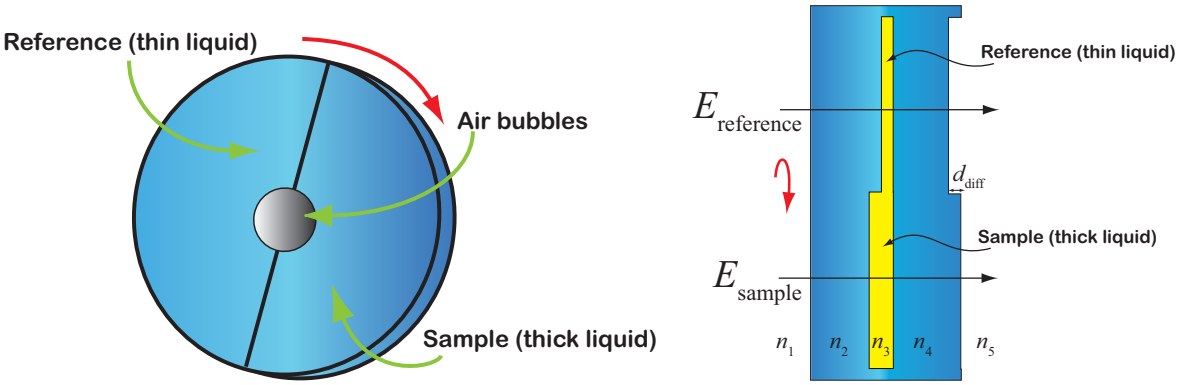

(a) Front view of window cell (b) Cross-section of window cell

Figure 8.2. Fixed dual-thickness geometry of COC 5013L10 window cell. This figure illustrates a fixed dual-thickness sample cell made from COC 5013L10 for a double-modulated DTDS liquid measurement. In Fig. 8.2a, the front view of sample holder is shown. The sample holder is designed to be half reference and half sample and mounted onto the spinning wheel as shown in Fig. 8.1. Figure 8.2b depicts the cross-sectional view. The window cell has a cavity with two different thicknesses. The reference (thin liquid) is set at 20 μm and the sample (thick liquid) is set at 170 μm. Here, n_1 and n_5 are the refractive index of air, n_2 and n_4 are the refractive index of the COC 5013L10 window cell, and n_1 is the refractive index of the liquid sample under test. Also, d_{diff} is the thickness difference between thin and thick liquid samples.

8.3 Experimental configuration

The experimental setup for a fixed dual-thickness THz liquid measurement using a spinning wheel is shown schematically in Fig. 7.3. A MiraSeed Ti-sapphire femtosecond modelocked laser is used to drive the THz system. The femtosecond laser produces an output pulse duration of 20 fs at a repetition rate of 76 MHz. This laser generates an output power of 1 W with a center wavelength of 800 nm. The pump beam is modulated at optical chopper frequency, f_{chopper} of 2 kHz. The THz pulse is generated due to the modulated pump beam incident on an emitting photoconductive antenna. The THz pulse is then collimated and focused onto the rotating dual-thickness liquid sample using the first pair of off-axis parabolic mirrors. The sample under test is located in the focal plane and modulated at frequency, f_{wheel} of 70 Hz. The transmitted THz pulse is recollimated and refocused onto the detector using the second pair of off-axis parabolic mirrors. The probe beam gates the incoming transmitted THz pulse by focusing the probe laser beam onto the photoconductive antenna at the detector.

The detected double-modulated THz signal is extracted based on a lock-in amplifier configuration described in the following section.

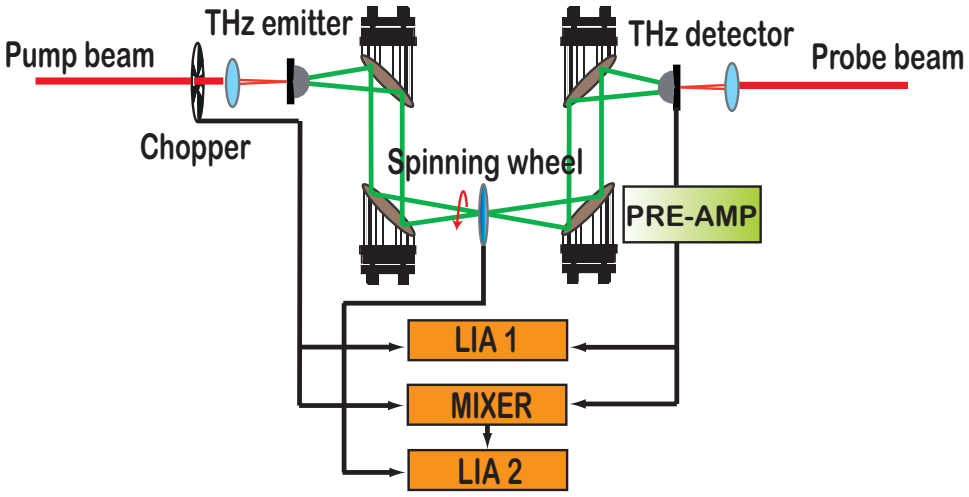

Figure 8.3. A double-modulated DTDS spectrometer schematic for dual-thickness liquid measurement. This schematic diagram shows a double-modulated DTDS spectrometer configured for characterising dielectric properties of liquid samples using a spinning wheel technique. The sample under test is located in the focal plane and modulated at frequency, f_{wheel} of 70 Hz.

8.3.1 Lock-in amplifier setting

A double-modulated signal detected at the output of the THz system is pre-amplified using a SR560 preamplifier. The amplified signal is then split by a ZFRSC-2050+ two-way power splitter. One end of the splitter output is connected to the input channel of lock-in amplifier one (LIA1) and the other end of the splitter output is connected to the mixer signal input channel. LIA1 demodulates the incoming THz signal with chopper reference signal, f_{chopper}, which is then low-pass filtered to produce a mean output signal. The mixer multiplies the incoming signal with the chopper reference signal, f_{chopper}, to produce sum and difference components, however, no filtering is applied in the mixer. The multiplied output of the mixer is then fed into the input channel of the second lock-in amplifier (LIA2). Here, LIA2 demodulates the signal detected at the input channel with the spinning wheel reference frequency, f_{wheel}. The demodulated signal is low-pass filtered to produce an amplitude output signal. The lock-in amplifier settings for mean and amplitude signal extraction are illustrated in Fig. 8.4.

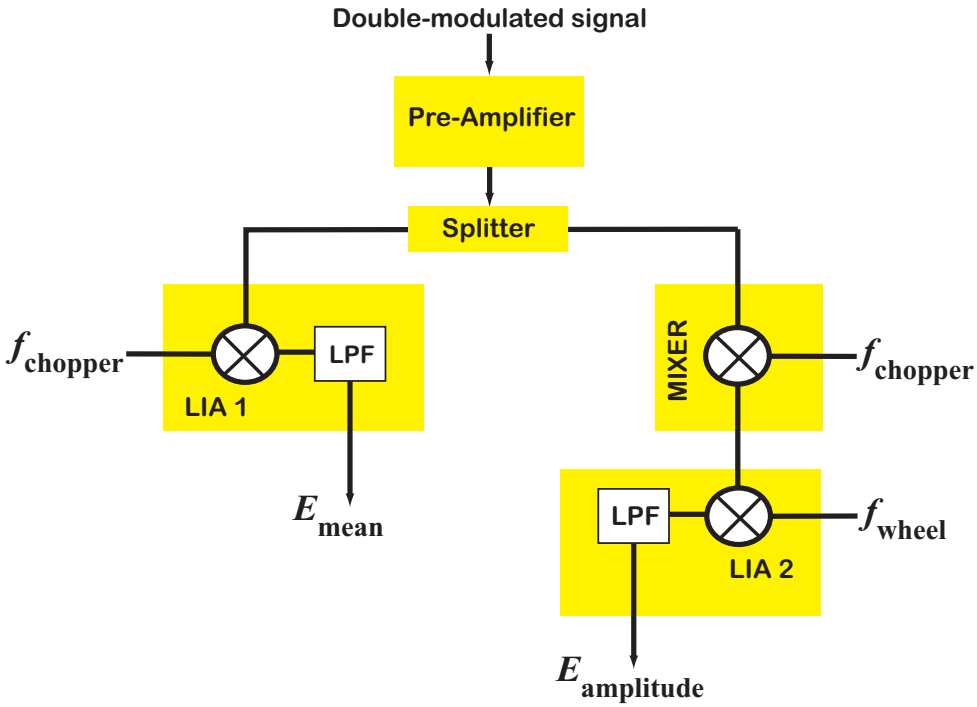

Figure 8.4. Lock-in amplifier settings for mean and amplitude signal extraction. In this figure, simultaneous dual-waveform acquisition (mean and amplitude) using two SR830 lock-in amplifiers and a MC1495P mixer is illustrated.

8.3.2 Sample preparation

The spinning wheel with a dual-thickness window cell is prepared according to Fig. 8.1. The thickness of the thin and thick cavities in the window cell is set to 20 μm and 170 μm respectively (Fig. 8.2). Here, the window cell thickness is set to 3 mm, which is sufficiently thick to avoid the Fabry-Pérot reflections. Liquid is injected into the cavities through the centre hole of the window cell using a syringe. In order to increase the signal-to-noise ratio of the measurements, five averaged scans at a lock-in amplifier time constant setting of 100 ms are used. Morever, the ambient water vapor spectral lines are reduced by conducting the measurements in a nitrogen purged environment. The excess liquid present on the surface of the window cell is removed before the measurement. All measurements are conducted at room temperature.

8.4 Mathematical formula

The output detected at LIA1 (Mean) and LIA2 (Amplitude) is used to extract the frequency dependent reference and sample signals based on the Eqs. 7.6 and 7.7 given in

Ch. 7. Thus, based on these equations, the complex transmission coefficient $\widetilde{T}(\omega)$, can be expanded as follows (refer to Sec. 6.2.3),

$$\widetilde{T}(\omega) = \frac{\exp(\frac{-j\tilde{n}_3\omega d_{\text{thick}}}{c})}{\exp(\frac{-j\tilde{n}_3\omega d_{\text{thin}}}{c}) \cdot \exp(\frac{-j\tilde{n}_5\omega d_{\text{diff}}}{c})} . \tag{8.1}$$

Here, $\tilde{n}_3 = n - j\kappa$, $\tilde{n}_5 = 1$ and $d_{\text{diff}} = d_{\text{thick}} - d_{\text{thin}}$. Liquid thicknesses, d_{thick} and d_{thin} are set to 170 μm and 20 μm respectively. By substituting these parameters into Eq. 8.1, the magnitude ρ and the phase ϕ can be obtained as follows:

$$\rho(\omega) = \exp(\frac{-\omega\kappa d_{\text{diff}}}{c}) , \tag{8.2}$$

$$\phi(\omega) = \frac{\omega d_{\text{diff}}(n(\omega) - 1)}{c} . \tag{8.3}$$

Hence, based on the magnitude and phase information from Eqs 8.2 and 8.3, the frequency dependent refractive index n, extinction coeffcient κ, and absorption coefficient α can be deduced as follows:

$$n(\omega) = \frac{\phi(\omega)c_0}{\omega d_{\text{diff}}} + 1 , \tag{8.4}$$

$$\kappa(\omega) = -\frac{c_0}{\omega d_{\text{diff}}} \ln|\rho(\omega)| , \tag{8.5}$$

$$\alpha(\omega) = 2\frac{\kappa(\omega)\omega}{c_0} . \tag{8.6}$$

8.4.1 Spinning wheel accuracy verification

The functionality of the spinning wheel technique for a dual-thickness liquid measurement is experimentally verified using water, ethanol, and methanol. The accuracy of the dielectric properties of the measured water is compared with the double Debye relaxation model, in which the frequency-dependent complex dielectric constant is given by (Debye 1942),

$$\hat{\epsilon}(\omega) = \epsilon_\infty + \frac{\Delta\epsilon_1}{1 + i\omega\tau_1} + \frac{\Delta\epsilon_2}{1 + i\omega\tau_2} . \tag{8.7}$$

The measurement accuracy of the dielectric properties of the measured ethanol and methanol is compared with the triple Debye relaxation model as follows (Debye 1942):

$$\hat{\epsilon}(\omega) = \epsilon_\infty + \frac{\Delta\epsilon_1}{1 + i\omega\tau_1} + \frac{\Delta\epsilon_2}{1 + i\omega\tau_2} + \frac{\Delta\epsilon_3}{1 + i\omega\tau_3} \,. \tag{8.8}$$

According to Eqs. 8.7 and 8.8, ϵ_∞ is the high-frequency dielectric constant and $\Delta\epsilon_1$, $\Delta\epsilon_2$, and $\Delta\epsilon_3$ refer to relaxation amplitudes. Here, τ_1 is the slow relaxation time constant, and τ_2 and τ_3 are the fast relaxation time constants of liquid. The parameters for the Eqs. 8.7 and 8.8 are obtained from Kindt and Schmuttenmaer (1996). Since the complex index of refraction is related to the dielectic properties of a material as given in the following equation,

$$\hat{\epsilon}(\omega) = \epsilon'(\omega) - j\epsilon''(\omega) = (n - jk)^2 \,, \tag{8.9}$$

one can rewrite the above equation in terms of n and α as follows:

$$n(\omega) = \left(\frac{\sqrt{\epsilon'(\omega)^2 + \epsilon''(\omega)^2} + \epsilon'(\omega)}{2}\right)^{\frac{1}{2}} \,, \tag{8.10}$$

$$\alpha(\omega) = \frac{2\omega}{c}\left(\frac{\sqrt{\epsilon'(\omega)^2 + \epsilon''(\omega)^2} - \epsilon'(\omega)}{2}\right)^{\frac{1}{2}} \,. \tag{8.11}$$

Here, $\omega = 2\pi f$, and c is the speed of light.

8.5 Results and discussion

In this section, we validate the dual-thickness liquid measurement technique using the following homogeneous liquids: water, methanol, and ethanol. In this work, we have limited our measurements to only homogeneous liquids since the technique presented may not be suitable for heterogeneous liquids (i.e., milk and blood) as it separates due to the centrifugal force introduced by the spinning wheel. Figure 8.5 shows typical time profiles for a double-modulated DTDS dual-thickness liquid measurement. In Fig. 8.5a, the mean signal detected at the output channel of LIA1 and the amplitude signal detected at the output channel of LIA2 are depicted. Figure 8.5b illustrates the reference and sample signals obtained based on the extracted mean and amplitude signals. The formulas given in Eqs. 7.6 and 7.7 are used to calculate the reference and sample signals. Figures 8.6 - 8.8 display the terahertz dielectric properties of water, methanol, and ethanol. The accuracy of the measurement results is compared with the Debye relaxation model.

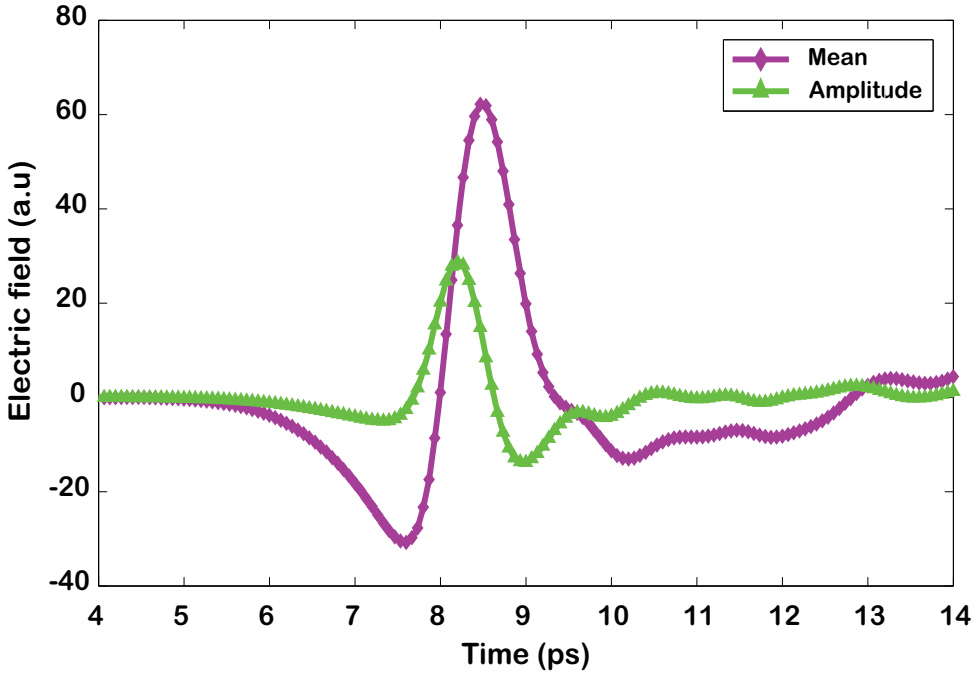

(a)

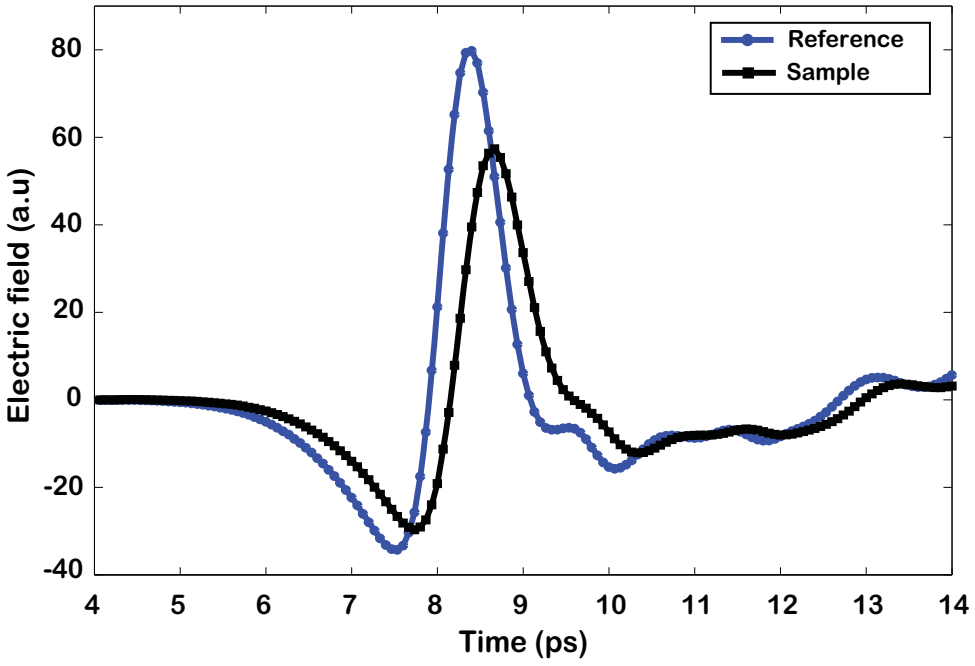

(b)

Figure 8.5. Time traces of a double-modulated dual-thickness liquid spectroscopy. This figure illustrates typical time profiles of double-modulated dual-thickness liquid measurements. (a) presents the mean and amplitude signals detected at the output channels of LIA1 and LIA2. The mean and amplitude information is then used to plot the reference and sample signals shown in (b) according to Eqs. 7.6 and 7.7.

8.5.1 Water

Water is known to have high absorption coefficient in the THz frequency band, typically 200 - 230 cm^{-1} at 1 THz (Kindt and Schmuttenmaer 1996). For the past decades, many studies have been conducted to analyse the dielectric response of liquid water in the terahertz frequency range. The dielectric response provides valuable information on solvation dynamics of liquid. In this work, an alternative measurement using a double-modulated dual-thickness spinning wheel technique to measure the dielectric properties of liquid water is shown. Figure 8.6 illustrates the refractive index and the absorption coefficient of liquid water. According to Fig. 8.6a, a close match can be seen between the measured refractive index and the refractive index from the double-Debye relaxation model. In Fig. 8.6b, we compare the absorption coefficient in this work with that from the double-Debye relaxation model obtained at a room temperature. We found a close match to the double-Debye model, however, a slight variation in the higher frequency range is seen. Since the Debye model is obtained at room temperature, heat generated by the spinning wheel results in slight discrepancies in the absorption coefficient.

8.5.2 Methanol

Methanol is a flammable polar liquid and its dielectric properties are well explored in the terahertz regime (Kindt and Schmuttenmaer 1996, Venables and Schmuttenmaer 2000a, Asaki *et al.* 2002, Sato and Buchner 2005). Here, the dielectric properties of methanol are measured using the double-modulated dual-thickness spinning wheel technique. Figure 8.7 shows the terahertz dielectric properties of methanol. Figure 8.7a compares the measured refractive index with refractive index obtained from the triple-Debye relaxation model. The results are in good agreement with the triple-Debye relaxation model. In Fig. 8.7b, an excellent match between the measured absorption coefficient and the absorption coefficient obtained from triple-Debye model is demonstrated.

8.5.3 Ethanol

Ethanol is another flammable polar liquid, which has drawn attention among terahertz researchers. The dielectric properties of ethanol are well explored in the terahertz

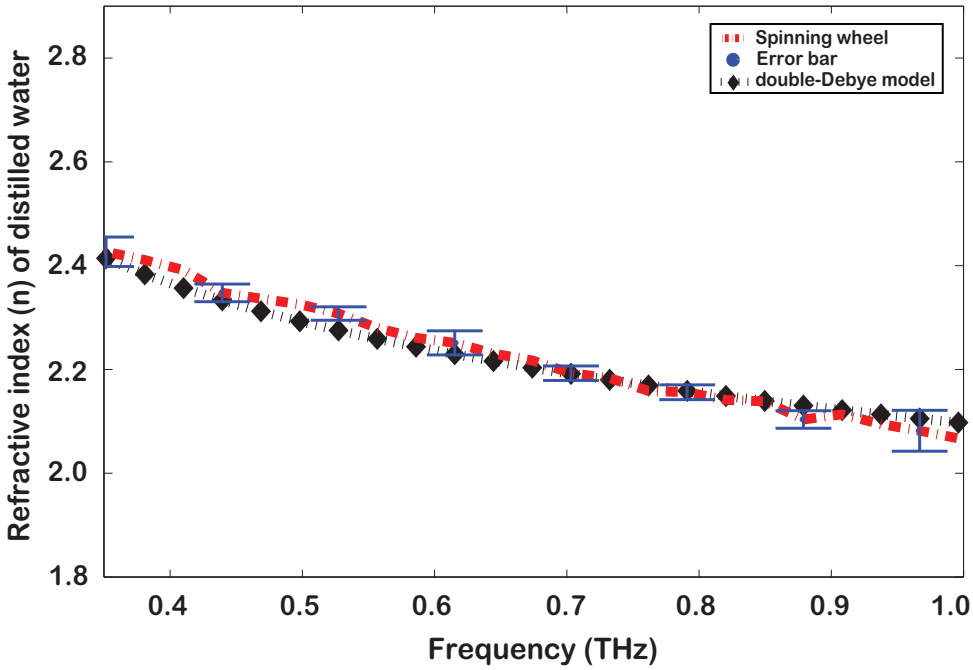

(a)

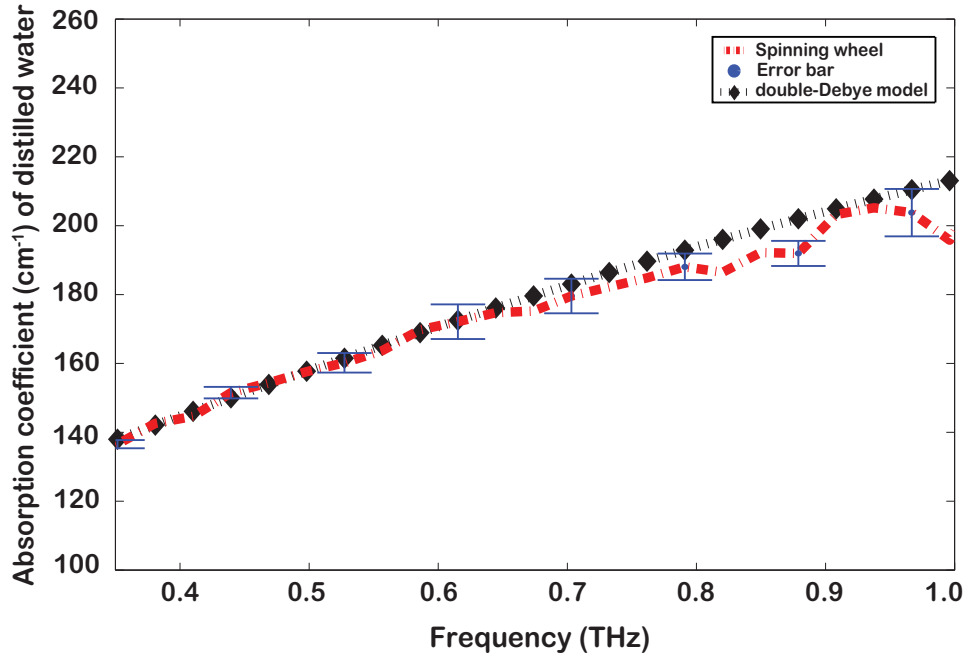

(b)

Figure 8.6. Refractive index and absorption coefficient of distilled water. This figure compares the experimental results with the double-Debye relaxation model. A good agreement between the measured data and relaxation model is seen. The double Debye relaxation model is plotted based on the parameters given in Kindt and Schmuttenmaer (1996). The error bars indicate an estimated uncertainty in the calculated values.

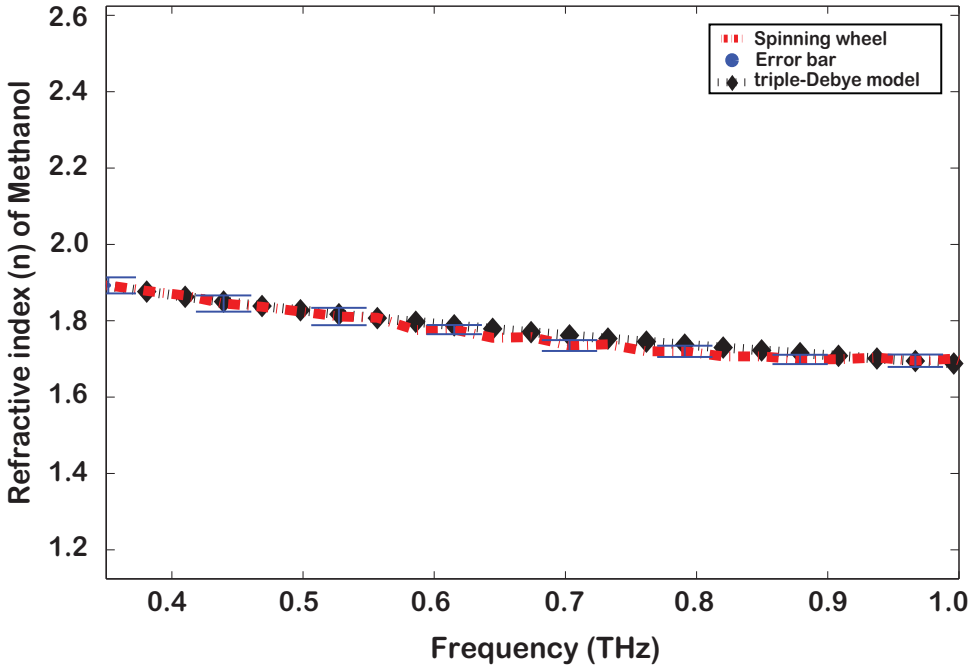

(a)

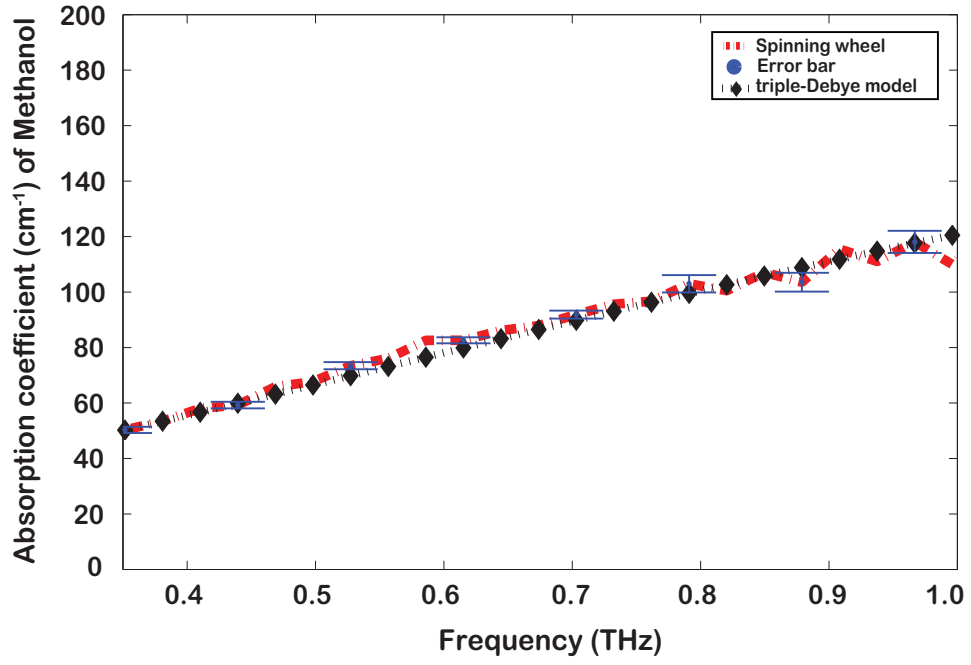

(b)

Figure 8.7. Refractive index and absorption coefficient of methanol. This figure compares the measured terahertz dielectric properties of methanol with the triple Debye relaxation model described in the Appendix. The fitting parameters for triple Debye relaxation model are obtained from Kindt and Schmuttenmaer (1996). The measured results are in an excellent agreement with the triple Debye relaxation model reported by Kindt and Schmuttenmaer (1996). Error bars indicate the uncertainty present in the calculated values.

regime (Kindt and Schmuttenmaer 1996, Jepsen *et al.* 2007) as well as in the gigahertz regime (Petong *et al.* 2000, Sato and Buchner 2005). In this section, we demonstrate the experimental results of the double-modulated dual-thickness technique, which is then compared with the triple-Debye relaxation model. The fitting parameters for the triple-Debye model are obtained from (Kindt and Schmuttenmaer 1996). According to our observation in Figure 8.8a, the measured refractive index of ethanol matches well with refractive index derived from the triple-Debye model. In Figure 8.8b, the absorption coefficient of ethanol is compared with absorption coefficient calculated from triple-Debye model. Here, a close match is demonstrated. Figure 8.9, shows the sample thickness error present in the thin and thick liquid layers of the fixed dual-thickness liquid sample holder. Based on the graph, one can say that δd_{thin} and δd_{thick} are less than 5 μm, as compared to 100 μm in the previously presented dithering technique (Mickan *et al.* 2004).

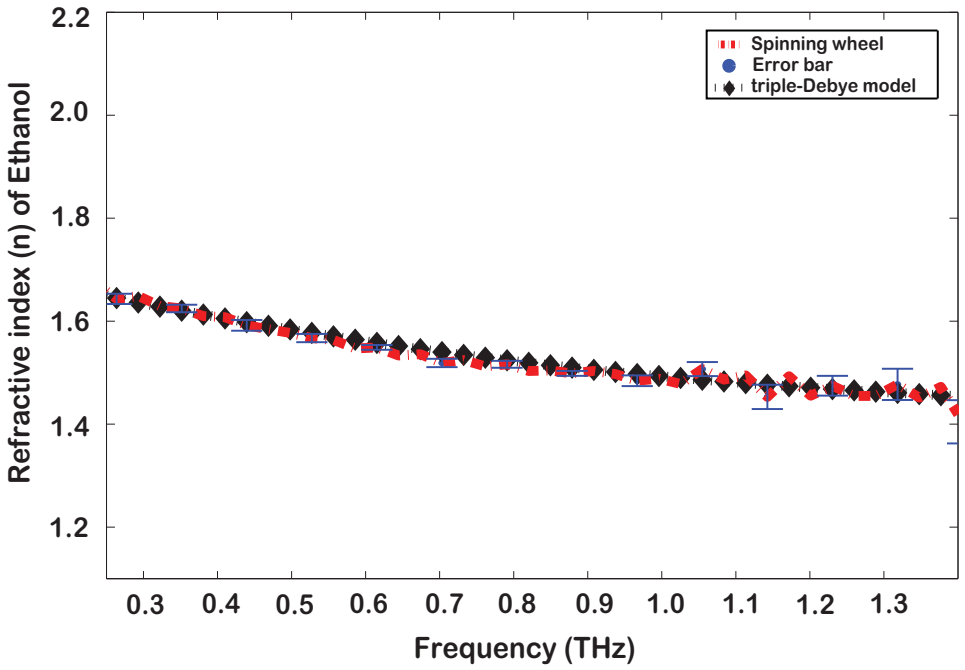

(a)

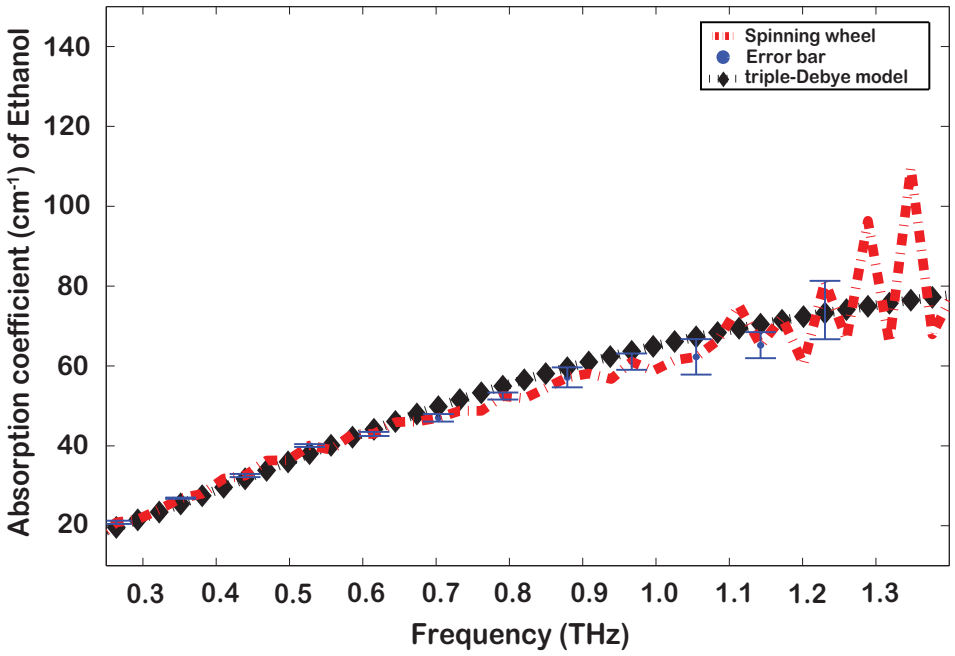

(b)

Figure 8.8. The absorption coefficient and refractive index of ethanol. This figure illustrates the measured terahertz dielectric properties of ethanol. The measured data is compared with the triple Debye relaxation model. A close match is demonstrated. The estimated uncertainty in the calculated values is indicated by the error bars.

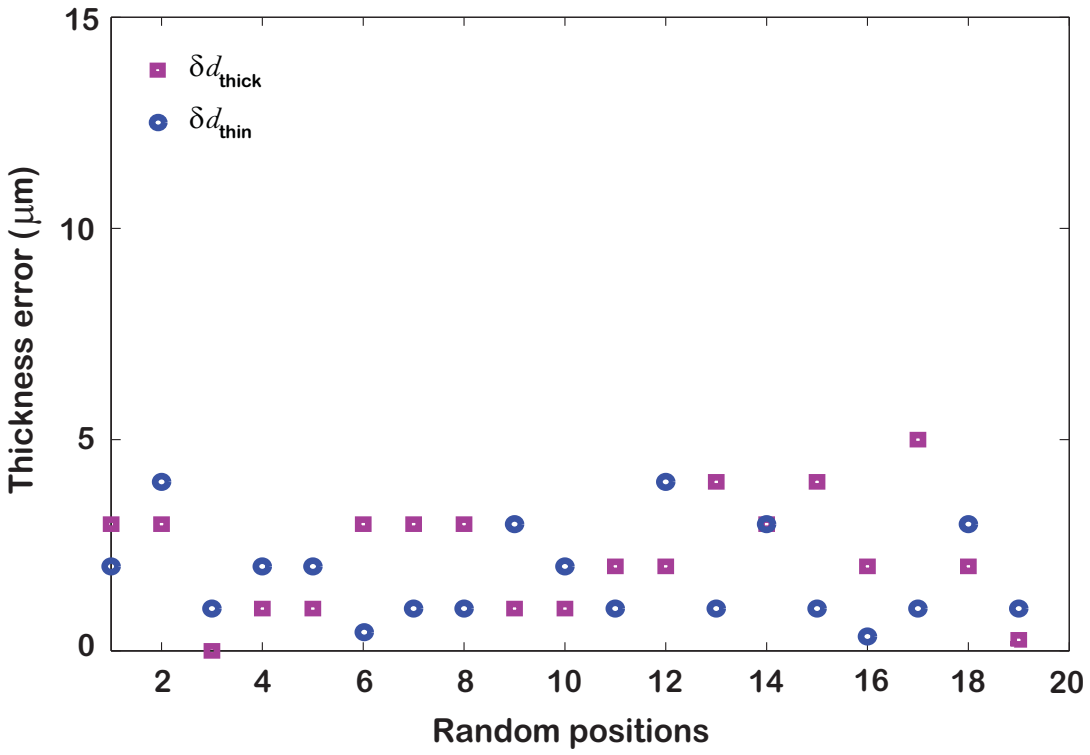

Figure 8.9. Sample thickness error present at random positions in the thin and thick liquid layer of the fixed dual-thickness liquid sample holder. This plot shows that the δd for thin and thick liquid layers are less than 5 μm.

8.6 Chapter summary

An approach for obtaining terahertz dielectric properties of thin-layered liquids using a spinning wheel technique is demonstrated. We have shown an improvement in the dual-thickness geometry by introducing a fixed dual-thickness window cell using a cyclic-olefin copolymer (COC) 5013L10 polymer material. The 100 μm sample thickness error introduced by linear dithering is reduced to less than 5 μm with our implementation of a fixed dual-thickness geometry. This work also highlights that bubble-free liquid measurement is achievable with a spinning wheel technique. Moreover, a rapid succession measurement between reference and sample signals is demonstrated. The measurement technique is validated by measuring three different homogeneous liquids (i.e., water, methanol, and ethanol). The measurement results show a good agreement with the Debye relaxation model. Therefore, this demonstrates the accuracy of the dual-thickness spinning wheel technique.

In the following chapter, we conclude the work described in this Thesis and recommend future directions of the work presented in this Thesis.

Thesis conclusion and recommendation

THIS chapter draws together the conclusions from the work described in this Thesis, and proposes directions for further research. A summary of the original contribution is given in this chapter.

9.1 Introduction

Section 9.2 summarises the research conducted in this Thesis and describes the major conclusions and novel contributions of this work. Section 9.3 highlights a number of remaining open questions identified in the course of this research and details research areas which form the logical next steps to build upon the contributions of this Thesis.

9.2 Thesis conclusions

The conclusions drawn from the experiments in this Thesis fall into several categories: (i) identifying optimal THz window material, (ii) spinning wheel technique for material parameter extraction double-modulated THz-DTDS scheme, and (iii) fixed dual thickness window cell for liquid spectroscopy.

9.2.1 Review of Electromagnetic spectrum

Chapter 2 introduces the electromagnetic spectrum through the diverse collection of electromagnetic waves that can be classified interms of a continous range of wavelength, frequency, or energy. In this chapter, a brief historical development of the electromagnetic spectrum is discussed. Chapter 3 focussed on the least explored region of the spectrum known as T-ray or THz. A fundamental principle of THz-TDS using photoconductive emission and detection is described in detail.

9.2.2 Review of THz dielectric properties of polymer materials

Chapter 4 reviewed THz dielectric properties of several polymer materials. The motivation of this chapter is to characterise a range of polymers with a view to identifying the best THz window material for the spinnning wheel device described in Ch. 8. In order to ensure that the reviewed polymer materials are low in water absorption, a hygroscopicity test was conducted using a linear absorption model in Ch. 5.

9.2.3 Review of THz-TDS sample cells for liquid spectroscopy

A review on various window cell geometries for liquid measurements is given in Ch. 6. In this chapter, we discussed four types of geometries used for liquid spectroscopy. A

detailed analysis technique is discussed here. We have also presented two custom-built sample holders for liquid spectroscopy in this chapter.

9.2.4 Review of THz material parameter extraction using a spinning wheel

Chapter 7 describes a novel spinning wheel technique for material parameter extraction based on double-modulated THz-DTDS scheme. In this chapter we have shown a measurement technique based on mounting the sample on a spinning wheel, in order to overcome fundamental limitations imposed by the dithering work presented in the previous work. In this work, we have also shown that the spinning wheel technique enables a rapid succesion of measurements between reference and sample signals with a single mechanical delay scan. Through this technique, we have demonstrated a proof-of principle showing that noise decrease as a function of the spinning wheel modulation frequency.

9.2.5 Review of Fixed dual-thickness terahertz liquid spectroscopy

With the proof-of-principle demonstrated in Ch. 7, we then demonstrated a fixed dual-thickness terahertz liquid spectroscopy using spinning wheel mechnanism for the first time in Ch. 8. Here, the reference signal is measured through the thin version of the liquid and the sample signal is measured via the thick version of the liquid. With the fixed dual-thickness geometry, we have reduced the 100 μm thickness error introduced by the linear dithering technique in the previous work to less than 5 μm. A bubble-free liquid measurement has been highlighted in this chapter.

9.3 Recommendation and future directions

With any rapidly developing technology there are a vast number of open questions and promising future research problems. The double-modulated THz-DTDS scheme is no different. This section surveys the scope of the future work in this area and particularly highlights promising extensions of the work presented in this Thesis.

The main focus of this Thesis is on the development of the spinning wheel device. Throughout this research work, we have demonstrated an improvement of 30% in noise performance as compared to the conventional THz-TDS measurement scheme. This improvement is obtained at a spinning speed of approximately 0.3 kHz. The question is, can we achieve a further improvement in noise performance? According to our conclusion given in Ch. 7, it appears that further improvement in noise performance can be achieved by development of hardware that effectively increases the modulation frequency introduced by the spinning wheel.

Initial hardware development would be to use air bearings instead of contact-roller bearings (ball bearings) to increase the speed limit and to reduce the friction effect on the spinning wheel. In order to accomodate the air bearings, a high power motor will be required. Additionally, slight modification in the hardware structure is required in order to support the high speed rotation.

9.4 Summary of original contributions

The original contributions in this Thesis were described in Sec. 1.3 of the introductory chapter. In summary, the key contributions are as follows:

- **Sensing the hygroscopicity of polymer and copolymer materials.** Experimental studies are carried out for the first time to measure the hygroscopicity of polymer materials in the low terahertz frequency band using a linear absorption model. Through this measurement, we have identified the optimal window material required for the fixed dual-thickness liquid measurement introduced in Ch. 8 (Balakrishnan *et al.* 2009b).

- **THz material parameter extraction using a spinning wheel.** A spinning wheel technique for THz material parameter extraction is demonstrated for the first time. This technique is implemented using the double-modulated THz-DTDS scheme (Balakrishnan *et al.* 2010).

- **Fixed dual-thickness terahertz liquid spectroscopy.** A novel fixed dual-thickness window cell is developed for liquid spectroscopy measurement. We have also demonstrated a reduction in the window cell thickness error to less than 5 μm (Balakrishnan *et al.* 2009a).

9.5 In closing

This chapter gives an overview of the major conclusions of this Thesis, and presents a number of recommendations for future work in the field. As summarised in this chapter, the Thesis has made a number of contributions to T-ray science and technology. The work herein is unique, original, and provides a direction for further contributions to T-ray science.